MASTER'S THESIS

Allocation of bone fluid throughout the hierarchical structure of bone: multi-technique analysis on bovine femur

submitted in satisfaction of the requirements for the degree of
Diplom-Ingenieur
of the TU Wien, Faculty of Civil Engineering

DIPLOMARBEIT

Verteilung von Körperflüssigkeit auf die hierarchisch organisierten Porenräume in Knochen: chemo-physikalische und mikroskopische Analysen am Rinderoberschenkel

ausgeführt zum Zwecke der Erlangung des akademischen Grades eines
Diplom-Ingenieurs
eingereicht an der Technischen Universität Wien, Fakultät für Bauingenieurwesen

von

Luis Zelaya-Lainez, MSc.
Matr.Nr.: 1328369
Brünner Straße 55/3/309
A-1210 Wien

unter der Anleitung von

Univ.Prof. Dipl.-Ing. Dr.Techn. **Christian Hellmich**

Dipl.-Ing. **Hawraa Kariem**

Institut für Mechanik der Werkstoffe und Strukturen
Technische Universität Wien
Karlsplatz 13/E202, A-1040 Wien

Wien, November 2016

_____

ABSTRACT

In a landmark series of physico-chemical experiments published over some 25 years (1979-2003), Lees and co-workers determined the mineral, organic, and water content of cortical bone samples from all over the vertebrate kingdom, across species ranging from fish to large mammals, from rips to ear bones, and from young to old individuals; thereby elucidating the large compositional variations throughout all these different bone tissues. In similarly pioneering neutron diffraction and transmission electrone microscopic studies, they also provided satisfying answers on as to how the elementary structural components of bone, namely collagen (making up 90% of the organic matter) and hydroxyapatite mineral, are organized in the extracellular spaces of bone, whereas the question on how the water (with 10% non-collagenous organics within it) is partitioned between the hierarchically organized pore spaces in bone, has remained, up to the knowledge of the authors, largely open. Namely, more recent imaging techniques revealing these fascinating pore morphologies have been never combined with physico-chemical testing of the same samples. This knowledge gap is tackled in the present contribution, by re-viving and refining the original protocols of Lees et al, and combining them with light and scanning electron microscopy. It turns out that handling cortical bone samples on air does not reduce the their water content, so that Lees' protocols indeed give access to the entire water in the vascular, lacunar, and ultrastructural pore spaces. In bovine bone, their partition is 13:8:79.

The thesis is structured as follows: After a general introduction into the hierarchical structure of bone and the methodology used, Chapter 2 contains a scientific paper summarizing in a concise fashion, the revival and refinement of the Lees protocols in combination with microscopic techniques, providing quantitatively the allocation of bone fluid throughout the different pore spaces found within the hierarchical organization of bone. Thereafter, additional technical and methodological aspects are summarized in Chapter 3. Subsequent appendices contain light microscopic images of the surfaces of all tested samples, sketches of the newly developed sample holder, and a conference poster contribution on the topic.

KURZFASSUNG

Als Meilenstein in der chemo-physikalischen Charakterisierung von Knochengeweben untersuchten Sidney Lees und Kollegen über 25 Jahre (1979-2003) lang die organischen, anorganischen und Wasser-Gehalte von Proben aus dem gesamten Wirbeltierreich, von Fischen bis großen Säugetieren, von Rippen bis Ohrenknochen, und über alle Altersstufen hinweg. Dabei zeigte sich eine große Variation in der Zusammensetzung solcher Gewebe. In ebenso wegweisenden Studien mittels Transmissionselektronenmikroskopie und Neutronenstreuung gaben Lees und Kollegen auch zufriedenstellende Antworten auf die Frage nach der Organisation der „strukturellen“ Komponenten von Knochengeweben, nämlich Hydroxyapatit-Mineral und Kollagen (welches 90% der organischen Strukturen ausmacht), innerhalb Wasser, innerhalb der extrazellulären Knochenräume. Vergleichsweise blieb die Frage nach der Verteilung des Wassers auf die in Knochengeweben auftretenden, hierarchisch organisierten Porenräume weitgehend unbeantwortet - während nämlich jüngste Bildgebungsverfahren faszinierende Porenmorphologien zutage gefördert haben, sind solche Studien in der Regel nie mit physiko-chemischen Versuchen kombiniert werden. Diese Wissenslücke soll mit dem aktuellen Beitrag geschlossen werden. Hier werden die Protokolle von Lees und Kollegen wiederbelebt und verfeinert, sowie mit Licht- und Rasterelektronenmikroskopie kombiniert. Es zeigt sich, dass die Behandlung der Proben in atmosphärischen Bedingungen ihren Wassergehalt nicht vermindert, sodass die Protokolle von Lees und Kollegen tatsächlich Zugang zum gesamten in den vaskulären, lakunären und ultrastrukturellen Porenräumen vorhandenen Wasser geben. In Rinderknochen ist diese Aufteilung durch das Verhältnis 13:8:79 gekennzeichnet.

Die vorliegende Arbeit ist folgendermassen aufgebaut: Nach einer allgemeinen Einleitung betre ffend hierarchische Organisation von Knochen und die verwendeten Methoden gibt Kapitel 2 in Form eines wissenschaftlichen Artikels eine konzise Darstellung der Wiederbelebung und Verfeinerung der Protokolle von Lees und Kollegen, sowie der gleichzeitig verwendeten mikroskopischen Techniken. Weitere technische und methodische Details werden in Kapitel 3 beleuchtet. Anschließende Appendizes zeigen lichtmikroskopische Aufnahmen der Oberflächen aller getesteter Proben, Pläne eines neu entwickelten Probenhalters, sowie eine Posterpräsentation zum Thema.

Abbreviations and Nomenclature

μCT micro-Computed Tomography

μm micrometer

ρ^{fluid} density of immersion fluid

ρ^{HA} density of hydroxyapatite

ρ^{HBSS} density of Hank's Balanced Salt Solution

ρ^{xylene} density of xylene

AFM Atomic Force Microscope

$CAMI$ Coated Abrasive Manufacturers Institute

$EDTA$ 0.5 M Ethylenediaminetetraacetic acid Solution pH 7.5

$f_{H_2O,PL}$ volume fraction of water in lacunar pores, per volume of wet macroscopic bone sample

$f_{H_2O,Pultra}$ volume fraction of water in ultra-structural pores, per volume of wet macroscopic bone sample

$f_{H_2O,PV}$ volume fraction of water in vascular pores, per volume of wet macroscopic bone sample

f_{H_2O} volume fraction of water, per volume of wet macroscopic bone sample

$f_{H_2O}^{ultra}$ the volume fractions of water, per volume of extra-cellular matrix

f_{HA} volume fraction of mineral (hydroxyapatite), per volume of wet macroscopic bone sample

f_{HA}^{ultra} the volume fractions of mineral (hydroxyapatite), per volume of extracellular bone matrix

f_{org} volume fraction of organic matter, per volume of wet macroscopic bone sample

f_{org}^{ultra} the volume fractions of organic matter, per volume of extra-cellular bone matrix

FEG Field Emission Gun

$FESEM$ Field Emission Scanning Electron Microscope

$HBSS$ Hank's Balance Salt Solution

$ICP-OES$ Inductively Coupled Plasma Optical Emission Spectrometer

LM Light Microscope

M_{dry} mass of dehydrated mineralized bone sample

M_{H_2O} mass of water contained in wet macroscopic bone sample

M_{HA} mass of mineral (hydroxyapatite) in wet macroscopic bone sample

M_{org} mass of organic matter contained in wet macroscopic bone sample

M_{wet} mass of wet macroscopic bone sample

mm millimeter

nm nanometer

$NPCs$ Non-collagenous Proteins

PL Lacunar Porosity

PLM Polarized Light Microscope

$Pultra$ Ultra-structure Porosity

PV Vascular Porosity

rpm revolutions per minute

SEM Scanning Electron Microscope

$SR-\mu CT$ Synchrotron Radiation micro-Computed Tomography

TEM Transmission Electron Microscope

V^{H_2O} volume of water contained within the wet macroscopic bone sample

V^{HA} volume of mineral matter contained within the wet macroscopic bone sample

V^{org} volume of organic matter contained within the wet macroscopic bone sample

V^{wet} volume of hydrated mineralized bone sample

$W_{immersed}$ weight of macroscopic bone samples submerged in fluid (xylene or HBSS)

$WF_{H_2O,PL}$ weight fraction of water component within lacunae pores

$WF_{H_2O,Pultra}$ weight fraction of water component within ultra-structure pore

$WF_{H_2O,PV}$ weight fraction of water component within vascular pores

WF_{H_2O} weight fraction of water component within mineralized bone sample

WF_{HA} weight fraction of mineral component within mineralized bone sample

WF_{org} weight fraction of organic component within mineralized bone sample

ACKNOWLEDGMENTS

Caminante, son tus huellas
el camino y nada más;
Caminante, no hay camino,
se hace camino al andar.
Al andar se hace el camino,
y al volver la vista atrás
se ve la senda que nunca
se ha de volver a pisar.
Caminante no hay camino
sino estelas en la mar.

—Antonio Machado

This work could have been never accomplished without the help and contribution from many people who I meet along my stay at the Institute for Mechanics of Materials and Structures.

First, I would like to express my sincere gratitude to my adviser and supervisor, Prof. Christian Hellmich for his guidance, trust, and continuous support through the course of this work. The great vision, knowledge, and creativity of Prof. Hellmich have been a source of inspiration not only for this work, but for my professional life.

I would like to acknowledge Dr. Orestis Andriotis for introducing me into the interesting field of tissue biomechanics.

I would like to acknowledge DI Winfried Nischkauer for the help provided during the experiment phase. His cooperation gave this work an extra level of precision.

I would like to thank my laboratory colleague DI Hawraa Kariem for her significant addition in the experiments. It was a pleasure to discuss many ideas with her.

I would also like to thank my colleagues at the Institute for Mechanics of Materials and Structures: Dr. Georg Kandler, Dr. Markus Lukacevic, DI Herwig Hengl, Dr. Giuseppe Balduzzi, DI Michael Schweigler, Dr. Leopold Wagner, DI Maximilian Autengruber, DI Thomas Kiefer, Mingjing Li, MSc., DI Thomas Schlappal, DI Wolfgang Lederer, DI Maria Pastrama, Dr. Markus Königsberger, DI Patricia Hasslinger, and Dr. Josef Füssl for all the help given, the discussions, and the best working environment I could ever wish for.

In addition, I would like to thank my parents and sisters for giving me so much emotional support and encouragement. Also, I am really grateful with my Austrian family and friends for helping with my adaptation and support.

Finally, I would like to specially praise all the help given to me by my wife, Dr. Michaela Fraubaum. There is no words to describe all the devotion, patience, confidence, and love that she provided me since we met.

To Michaela

—Luis Z.

Contents

Chapter 1

CHAPTER 1

Introduction

1.1 Bone and major components

Bone is a biological tissue found in any vertebrate. It is a specialized tissue that performs several structural and physiological functions, e.g. the protection of organs, locomotion, calcium homeostasis, storage of phosphorous [Parfitt, 1983], [Weiner and Wagner, 1998]. It is well accepted that bone is a hierarchical composite material [Katz et al., 1984], [Hellmich and Ulm, 2002], and that it has three major components i.e. organic, mineral, and bone fluid components. Initially, the mechanical properties of bone were just analyzed in terms of the organic and mineral components. Currey [Currey, 1964], [Currey, 1969] observed that the mineral component has a high Young's modulus of elasticity, while the organic component has better tensile properties than the mineral phase and a low Young's modulus of elasticity. This proved to be not a competent way to describe the mechanical properties of cortical bone [Katz et al., 1984]. The combination of the structural and the volumetric information of bone along its hierarchical organization [Katz et al., 1984] is a more adequate description [Weiner and Wagner, 1998], [Hellmich and Ulm, 2002]. In addition, the mechanical role of the third major component, bone fluid, is less known and cannot be underestimated [Weiner and Wagner, 1998].

Experiments on cortical bone like the ones performed by [Robinson and Elliot, 1957], [Lees et al., 1979b], prompted quantitative results to the inquire of the volume fraction of the major component found within bone. [Robinson and Elliot, 1957] remarked that the proportions of organic, mineral, and bone fluid components can vary widely between the different types of bone.

1.2 Hierarchical Structure of bone

Several contributions [Katz et al., 1984], [Weiner and Wagner, 1998], [Hellmich and Ulm, 2002] referred to the ways the hierarchical organization influences the mechanical behavior of bone, and with this on mind, we distinguished five levels of hierarchical organization:

1. *Constituents level.* At the tens of nanometers scale, this level consists of the constituents of the major components or the so-called elementary components of mineralized tissue. These elementary components can be classified into organic or inorganic constituents.

   The organic constituents are further divided into collagen type I proteins which account for 90% of the organic component [Buckwalter et al., 1996], and over two hundred non-collagenous proteins (NPCs) account for the remaining 10% of the total protein content [Weiner and Wagner, 1998]. The NPCs include also proteoglycans, phospholipids, glycoproteins, and phosphoproteins [Urist et al., 1983]. Proteoglycans have a regulatory effect, and phospholipids have a significant role in calcification. The degree of calcification is influenced by the NPCs [Butler, 1984].

   The collagen type I fibrils with diameters of 50-500 nm [Hellmich and Ulm, 2002] are assembled by tropocollagen macro-molecules [Pestruska and Hodge, 1964], at the same time, each tropocollagen is composed of three equivalent helical polypeptide chains [Bryan, 1951], [Orgel et al., 2006]. Due

to a certain variety of amino acid sequences, the tropocollagen may have some heterogeneity [Mahalanobis, 1936].

According to the two-dimensional model proposed by [Pestruska and Hodge, 1964], the collagen type I is assembled by macro-molecules consisting of two α_1 chains and one α_2 chain [Mahalanobis, 1936]. Each of the two α_1 chains consists of a repeating five identical sub-units σ_1 sequence, meanwhile the α_2 chain consists of a repeating seven identical sub-units σ_2 sequence. The shifting of the tropocollagen macro-molecules create regions of gaps. The tropocollagen macro-molecules are stabilized by enzymatic and non-enzymatic cross-links [Andriotis et al., 2015]. These cross-links are essential for the tensile strength of the collagen type I fibrils and the stiffening of the tissue [Hassenkam et al., 2005], [Bailey, 2001].

Recent findings by [Orgel et al., 2006] showed that the theoretical two-dimensional model is slightly simplistic to describe the thought that the gap regions is where the inorganic constituents are located [Bonucci, 2000], [Georgiadis et al., 2016]. [Orgel et al., 2006] introduced a model that uses an electron density map to describe a more realistic three-dimensional structure as seen in Fig. [2.1].H.

The inorganic constituents found within mineralized bone tissue are an impure form of hydroxyapatite ($Ca_{10}[PO4]_6[OH]_2$) [Gong et al., 1964], [Weiner and Wagner, 1998], [Lees, 1987], [Hellmich et al., 2004] and water [Robinson and Elliot, 1957].

2. *Suprafibrillar-structural level.* At this level, we considered the domains referred to as collagen type I fibrils or intrafibrillar space, and the extrafibrillar space. According to [Hellmich and Ulm, 2003], most of the hydroxyapatite crystallites are be located at the extrafibrillar spaces. Bone fluid can be located in the intrafibrillar or in the extrafibrillar spaces [Weiner and Wagner, 1998], [Fritsch and Hellmich, 2007].

3. *Ultra-structural level.* At this scale several collagen type I fibrils form a "bundle". [Gao et al., 2003] claimed that most of the mineral is located within the collagen fibrils or intrafibrillar spaces, while [Hellmich and Ulm, 2003] claimed the majority of the mineral content is located outside the fibrils or extrafibrillar spaces. Studies using TEM, as seen in Fig.2.2.G, showed the clear division of organic and mineral components. This brought the thought of an impure hydroxyapatite material coating the collagen "bundle" [Prostak and Lees, 1996]. This can be seen with more detail in Fig.2.2.G [Hassenkam et al., 2005]. This way of calcification may be due to the extra-cellular matrix vesicles [Anderson et al., 2005], although this can be only one of the ways that mineral component are formed.

   The spaces found within the suprafibrillar- and ultra-structure level, where bone fluid can be located, are part of the ultra-structure porosity *Pultra*. The amount of bone fluid contained within *Pultra* varies depending on the degree of mineralization in the bone [Lees, 1986], [Lees and Escoubes, 1987], [Lees, 1987], [Weiner and Wagner, 1998]. The *Pultra* is therefore considered the lowest characteristic lineal dimension porosity [Cowin, 1999].

4. *Micro-structural level.* At the scale around 100 μm, the organic and inorganic constituents form even more complex structures e.g. osteons. These osteons are constructed by substructures called lamellae. [Marotti et al., 1994] classified these lamellae substructures as collagen rich (dense) and collagen poor (loose) lamellae, and can be observed in Fig.[2.1].E.

   The center of an osteon is composed by a vascular canal. These canals, i.e. haversian and Volksmann canals, that conform the vascular porosity *PV*, enclose the vasculature, the nerves, and the bone fluid ([Zhang et al., 1998]). The lacunae porosity *PL* shelters the osteocytes, and is connected by a series of microscopic channels called canaliculi [Hesse et al., 2014]. Due to diameters of around 100 nm [Atkinson and Hallsworth, 1983], the canaliculi are also treated as part of *Pultra*.

   [Newman and Newman, 1958] called the fluid contained in the vascular canals i.e. Haversian canals and Volksmann canals, "serum" and the fluid contained in the "smaller" pores i.e. lacunae pores and ultra-structure porosity, "extra-cellular fluid". Both bone fluids have an equivalent composition,

but are contained in different pressures. The pressure of the fluid within the "smaller" pores is high, meanwhile the pressure in the vascular canals is considered to be low [Morris et al., 1982], [Zhang et al., 1998]. It is acknowledged that bone fluid is crucial for the transport of nutrients to the bone-forming cells (osteoblasts), and waste from the bone-resorbing cells (osteoclasts) [Cowin, 1999], [Pivonka et al., 2013].

5. *Macro-structural level.* Is the structural level where size and shape of whole bones are considered.

Besides the hierarchical organization illustrated in Fig.[2.1], the quantitative aspects of bone fluid within this partition levels remains largely unknown. The present work elucidates the lack of association between past experiments concerning the quantification of the major component, and studies related to the calculation of bone porosity by refining the landmark protocol of [Lees et al., 1979b], and performing simultaneous investigations with the LM.

1.3 Overview of methodology

1.3.1 Light Microscopy (LM)

It is an instrument that uses visible light and magnifying lenses to examine objects that are not visible to the naked human eye [Bradbury and Bracegirdle, 1998]. The LM is used in this work to calculate the PV and PL.

1.3.2 FESEM and SEM

The main difference between a SEM and FESEM is the emitter type of each. SEM uses a thermionic emitter, which uses electrical current to heat up a filament. Tungsten is the most common material used for filaments. The filament must heat enough to overcome the work function of the material, and this way the electron can be emitted. A thermionic source has a relative low picture brightness, a high evaporation of cathode material, and a big thermal drift during the operation of the instrument. In the other hand, FESEM uses a FEG to avoid these drawbacks. The FEG does not heats up the filament, and is a great electrical potential gradient which facilitates the emission. The FEG uses also Tungsten as a filament material, which in this case is a wire assembled in a end of the head. The FESEM was used to identify some of the PV and PL of bone specimens.

1.3.3 Demineralization using EDTA

A 0.5M ethylenediaminetetraacetic acid (EDTA) solution with pH 7.5 was used to demineralized the bone samples. EDTA is a demineralizing agent [Suvarna et al., 1996], which is used to create a chelate employing metallic ions. In contact with bone, an EDTA solution demineralizes the mineralized bone matrix by capturing the calcium, phosphorous, and magnesium ions from the surface of the hydroxyapatite crystals, and therefore reducing its size. The process of demineralization using EDTA is a slow procedure [Skinner et al., 1997], which can take several weeks (see Chapter 2). Due to the lethargic action rate of EDTA, the method is gentle with the sample, causing little damage to the organic structure.

1.4 Motivation

The three major components of bone i.e. organic content, mineral content, and bone fluid, have completely different mechanical properties. It is acknowledge that the mechanical properties of bone depend on the organic content [Katsamenis et al., 2015] and the degree of mineralization of bone [Hellmich and Ulm, 2002]. Meanwhile, the mechanical role of the third major component, bone fluid, is less known and cannot be underestimated [Weiner and Wagner, 1998], [Hellmich and Ulm, 2003]. The main motivation of this work is to quantify the amount of fluid within the bone, as well as to establish until certain degree the location of it. The author used the experiments performed by [Robinson and Elliot, 1957] and [Lees et al., 1979b]

as a "building base" or reference to obtain the quantification of the three major components, and added new methodologies to determine with more detail the location of fluid within bone.

1.5 Contribution by the author

The core of this master's thesis is a scientific paper that will be submitted for publication. The title of the scientific paper is **"Allocation of bone fluid throughout the hierarchical structure of bone: multi-technique analysis on bovine femur"**, and it can be found in Chapter 2.

The author contributed with the state-of-art of this work, a technical report found in Chapter 3, the sample preparation and measurements at the laboratory, and a new method to quantify the amount of the components found in a bovine femur specimen.

CHAPTER 2

CHAPTER 2

Allocation of bone fluid throughout the hierarchical structure of bone: multi-technique analysis on bovine femur

Authored by: Luis Zelaya-Lainez[1], Hawraa Kariem[1], Winfried Nischkauer[2], Andreas Limbeck[2], and Christian Hellmich[1]

scientific article to be submitted in an international refereed journal

Abstract

In a landmark series of physico-chemical experiments published over some 25 years (1979-2003), Lees and co-workers determined the mineral, organic, and water content of cortical bone samples from all over the vertebrate kingdom, across species ranging from fish to large mammals, from rips to ear bones, and from young to old individuals; thereby elucidating the large compositional variations throughout all these different bone tissues. In a similarly pioneering neutron diffraction and transmission electrone microscopic studies, they also provided satisfying answers on as to how the elementary structural components of bone, collagen (making up 90% of the organic matter) and hyroxyapatite mineral are organized in the extracellular spaces of bone, the question on how the water (with 10% non-collagenous organics within it) is partitioned between the hierarchically organized pore spaces in bone, has remained, up to the knowledge of the authors, largely open; as more recent imaging techniques revealing these fascinating pore morphologies have been never combined with physico-chemical testing of the same samples. This knowledge gap is tackled in the present contribution, by re-viving and refining the original protocols of Lees et al, and combining them with light and scanning electron microscopy. It turns out that handling cortical bone samples on air does not reduce the their water content, so that Lees' protocols indeed give access to the entire water in the vascular, lacunar, and ultrastructural pore spaces. In bovine bone, their partition is 13:8:79.

[1]Institute for Mechanics of Materials and Structures, Vienna University of Technology (TU Wien), Karlsplatz 13/E202, 1040 Vienna, Austria.

[2]Institute of Chemical Technologies and Analytics, Division of Instrumental Analytical Chemistry, Vienna University of Technology (TU Wien), Getreidemarkt 9/164, 1060 Vienna, Austria.

2.1 Introduction

Bone is a composite material consisting of mineral, organic, and fluid components [Parfitt, 1983], [Weiner and Wagner, 1998], [Hellmich and Ulm, 2002]. What complicates the matter, is that bone is also hierarchically organized [Katz et al., 1984], [Lakes, 1993], i.e. the mineral and organic phases, making up the "solid" part of the material, are intertwined at different length scales, and in particular the fluid is partitioned between various pore spaces, again visible at different length scales; see Figure 2.1.

These complicated features have of course attracted many researchers over far more than hundred years, with a typically quite focused interest: On the one hand, experimental campaigns have aimed at quantification of the mineral, organic, and fluid content of different bone samples [Hammett, 1925], [Burns, 1929], [Biltz and Pellegrino, 1969], culminating in the unparalleled work of Lees and coworkers [Lees et al., 1979a], [Lees et al., 1979b], [Lees and Heeley, 1981], [Lees et al., 1983], [Lees et al., 1984a], [Lees et al., 1984b], [Lees, 1986], [Lees and Escoubes, 1987], [Lees, 1987], [Lees and Page, 1992], [Lees et al., 1994a], [Lees et al., 1994b], [Lees et al., 1995], [Prostak and Lees, 1996], [Lees, 2003]. Thereby, the key focus was on the bone ultrastructure, i.e. on the organization of the about 100 nm wide collagen fibrils and the mineral crystals within and around them. Starting with early hypotheses on the distribution of hydroxyapatite crystallites throughout the ultrastructure of bone [Lees, 1979], these ultrastructural features were then more and more clearly seen in transmission electron micrographs (TEM) [Lees and Prostak, 1986], [Lees et al., 1994b], [Prostak and Lees, 1996], [Benezra Rosen et al., 2002], [Rubin et al., 2003], [Rubin and Jasiuk, 2005], [Alexander et al., 2012], [McNally et al., 2012], [McNally et al., 2013], [Schwarcza et al., 2014], or atomic force microscopy (AFM) [Sasaki et al., 2002], [Hassenkam et al., 2004], [Bozeca et al., 2005], [Hassenkam et al., 2005], [Wallace, 2012].

At this level, ten nanometer-sized inter-crystalline pores appear between the mineral crystals, while even smaller, one-nanometer sized intermolecular pores appear within the fibrils, as evidenced from electron density maps [Orgel et al., 2000], [Orgel et al., 2001], [Orgel et al., 2006], see Figure 2.1.[h]. Such ultrastructural investigations typically do not explicitly report on the pore spaces appearing at larger length scales, i.e. in the ten to hundred micrometer range.

On the other hand, the aforementioned larger pore spaces, i.e. the ten micrometer-sized lacunar pores hosting single osteocytes and the 50 to 500 micrometer-sized vascular pores hosting a variety of cells (including 10 micrometer-sized osteoblasts and up to 100 micrometer-sized osteoblasts [Buckwalter et al., 1996]) as well as blood vessels, see Figure 2.1.[a-c], have been the key focus in microscopic [Frost, 1960], [Schaffler and Burr, 1988], [Sietsema, 1995], [Fritsch and Hellmich, 2007], and computer-tomographic activities [Hannah et al., 2010], [Dong et al., 2013], [Mader et al., 2013], [Carriero et al., 2014], together with the lamellar structures seen around these pores in the light microscope; which at higher magnification under the Scanning Electron Microscope (SEM) appear as dense and loose packings of collagen fibrils [Marotti, 1993], [Marotti et al., 1994].

The present contribution wishes to close the knowledge gap between these two groups of bone microstructure investigations. Therefore, we have re-established and refined the landmark protocol of Lees at al., and accompanied all the chemical steps involved by comprehensive microscopic investigations. As result, we arrive not only at the mineral, organic, and fluid content within a piece of bone, but we can, probably for the first time, exactly assign the bone fluid to vascular, lacunar, and ultrastructural subcompartments. The corresponding details are covered in the remainder of this paper, which is structured as follows:

A Materials and Methods section reports on the harvesting of twenty-four millimeter-sized specimens of cortical bone from a bovine femur; on dehydration, re-hydration, and demineralization tests performed on these samples, always with accompanying mass and volume measurements; on light microscopic imaging of the surfaces of these samples; and on mathematical relations allowing for derivation, from these tests, the volume fractions of the elementary components and of the different pore spaces hosting the bone fluid. Corresponding results are compiled in a Results section; which is followed by a conclusive Discussion Section.

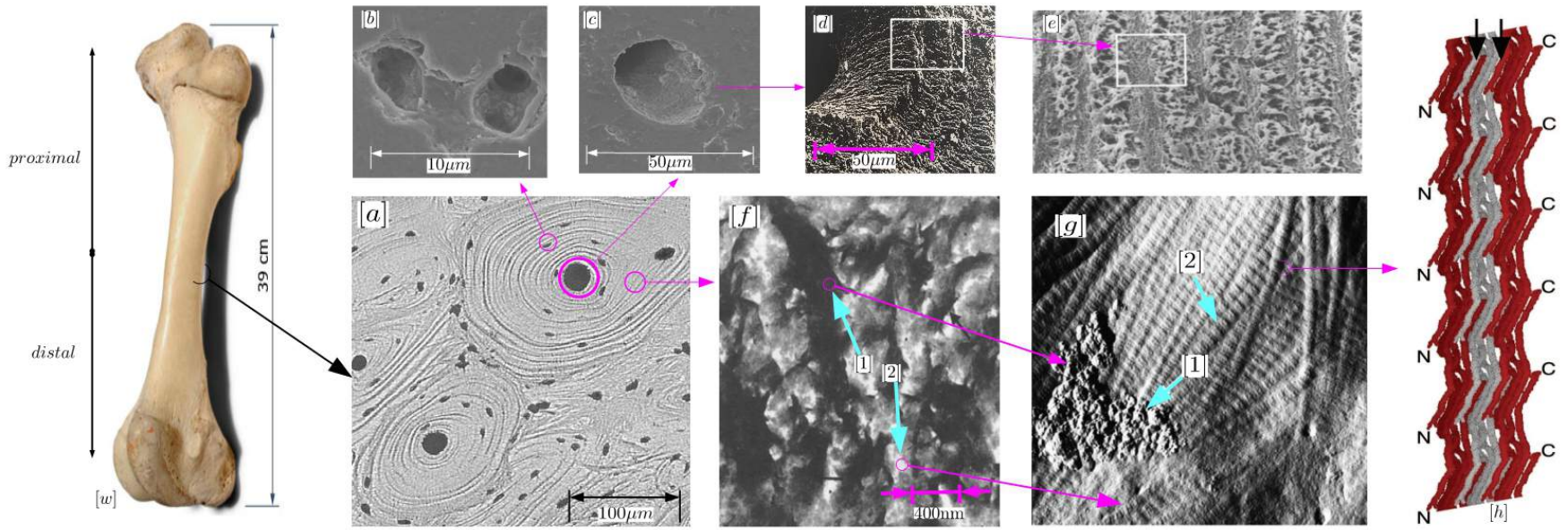

Figure 2.1: [*a*] micro-structural level of the axial face observed under the LM using a magnification of 100x. [*b*] lacunae pores observed with the FESEM using a magnification of 12000x and a voltage of 5kV at High Vacuum. [*c*] Haversian canal observed with the FESEM using a magnification of 1600x and a voltage of 5kV at High Vacuum. [*d*] With SEM and a voltage of 10 kV, [Raspanti et al., 1995] observed the lamellae structure near a haversian canal [*e*] With SEM (magnified 1965x), [Marotti, 1993] observed and identified the alternating types of lamellae i.e. dense and loose lamellae.[*f*] TEM of cross section from a fully mineralized human bone. Arrow [1] points the mineral full extrafibrillar space and arrow [2] points the protein content or intrafibrillar space [Prostak and Lees, 1996]. [*g*] A 2x2 μm^2 tapping mode AFM, arrow [1] points impure hydroxyapatite material and arrow [2] points collagen fibrils forming a "bundle" [Hassenkam et al., 2005]. [*h*] Model of a collagen fibril by [Orgel et al., 2006]. Three tropocollagen are shown side by side with a remark at the possible binding site. A N-terminal of a sub unit from a tropocollagen is bound to two other, while a C-terminal cross-links with only one. The banding seen in collagen fibrils is due to the 3D organization of these tropocollagens.[*w*] Bovine femur (public image from the University of New South Wales, Australia)

2.2 Materials and Methods

2.2.1 Sample Preparation

A bovine femur was purchased from a local butcher. First, a 16 mm high cylindrical segment with plane cross sections orthogonal to the long bone axis (see Figure 2.2.[a,b]) was cut out of the femoral shaft by means of a handsaw. This segment was then rinsed under a 5% ethanol solution, in order to facilitate the scalpel-based removal of the periosteum, the endosteum, and the bone marrow. Thereafter, the segment was cleaned with distilled water in an ultrasonic bath for five minutes, and then stored in a frozen state, i.e. at -20 centigrades, for four days. Then, the segment was further sectioned by means of a diamond blade saw (EXAKT Systeme, Germany); first in the transverse direction, resulting in two cylindrical samples of 8 mm height; and then these two smaller segments were cut into halves, along the longitudinal direction (see Figure 2.2.[c,d]). These four halves were then cut longitudinally into six pieces each, the latter measuring approximately $3 \times 2 \times 8$ mm, by means of an Isomet low speed saw (Buehler, USA), with cubic Boron Nitride (cBN) blades of 1270 mm diameter and 0.4 mm thickness rotating at 150 rpm, under distilled water as a cooling medium. Thereafter, the same cutting specifications were employed for removing the remaining trabecular portions from the 24 samples. After cleaning again the samples with distilled water in an ultrasonic bath for five minutes, they were stored in a frozen state at -20 centigrades for four days. The samples were subsequently attached, one by one, to a custom-made steel holder, and the surfaces of one of the sections oriented perpendicular to the long bone axis were polished in a two-step process using a PM5 Polishing system (Logitech Ltd., UK). The first step consisted of grinding the aforementioned planar surfaces of the samples by means of a 1000 CAMI grit Silicon Carbide (SiC) 305.00 mm diameter polishing paper rotating at 15 rpm for ten minutes, with Ethylene glycol as lubricant medium. After the first step, the samples were cleaned with distilled water in an ultrasonic bath for fifteen minutes, and subsequently under a light microscope (Carl Zeiss, Germany) at hundred-fold magnification, in order to check the realization of uniformly grinded surfaces. For the second step, an 1.00 micron poly-crystalline diamond suspension was used to final-polish each samples for two hours, using a 304.80 mm diameter micro-cloth at 30 rpm as a polishing surface. The polishing method reduced the sample height by about 1.2 mm, resulting in final sample sizes of $3 \times 2 \times 7$ mm. After cleaning the individual samples with distilled water in an ultrasonic bath for fifteen minutes, the samples were examined under the aforementioned light microscope (Carl Zeiss, Germany), in order to check whether a satisfactory polishing finish would have been attained. In addition, selected areas of the polished sections were imaged by a Field Emission Scanning Electron microscope (FESEM Quanta 200; FEI Company, USA). Thereafter, the samples were stored in a 0.15 N saline solution at room temperature, until the physical and chemical tests described next, were initiated.

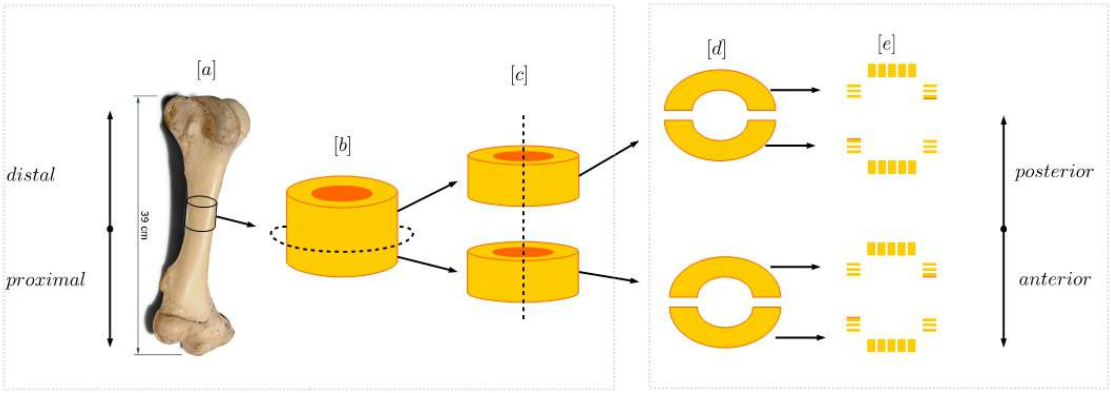

Figure 2.2: Schematic drawing of the sample preparation steps, from the sawing with the hand saw until the twenty-four sample cuts with the low speed saw. [*a*] A longitudinal 16mm section from a bovine femur was cut with a hand saw (public image from the University of New South Wales, Australia) [*b*] The 16 mm section was cut into two 8 mm londitudinal subsections with the diamond band saw. [*c*] The two 8 mm subsections were cut longitudinally with the diamond band saw into four smaller subsections.[*d*] The four halves seen from the axial plane.[*e*] The four halves were cut with the low speed saw into the twenty four samples.

2.2.2 Dehydration, re-hydration, and demineralization tests, accompanied by weighing

Following the storage of the bone samples in a 0.15 N saline solution, each sample was dehydrated under vacuum alongside with an orange silica gel desiccant, at room temperature. The mass from each of the samples was monitored in a precision balance Mettler Toledo model PGH403-S (Mettler-Toledo International Inc., Switzerland), four, five, and six days after starting the dehydration process. From the seventh day onward, no change of mass could be recorded any more, so that the samples were then regarded as being fully dehydrated, with mass M_{dry}.

Thereafter, the 24 samples were re-hydrated again, eighteen of them by immersion of eighteen samples into a Hank's Balanced Salt Solution (HBSS) with 7.4 pH, and six samples were immersed in xylene. During the re-hydration process, the mass of each sample was monitored every two hours, over a 24 hour period; and thereafter once a day, for a six day period. Directly before each mass monitoring step, the samples underwent an immersion fluid-specific treatment, in order to arrive at the real sample mass, without accounting for any additional surface-bound fluid: The HBSS- immersed samples were wiped free of surface water with Rotizell Tissues (Carl Roth GmbH, Germany) before measuring their mass, while the samples immersed in xylene were hold with tweezers in the air until no more fluid trickled from them. After the seven days of re-hydration, the samples were again constant in mass, i.e. they were fully re-hydrated, exhibiting the sample-specific masses M_{wet}. It allows for the definition of a hydration degree $m(t)$ increasing over the seven day re-hydration period, reading as

$$m(t) = \frac{M(t)}{M_{wet}} \tag{2.1}$$

The differences between the masses of the wet samples and the masses of the corresponding dry samples provide the masses of water in each and every specimen, according to

$$M_{H_2O} = M_{wet} - M_{dry} \tag{2.2}$$

After re-hydration, the volume of each sample was determined from Archimedes' principle: The weight $W_{immersed}$ of the samples of the samples under immersion (in HBSS or Xylene, respectively) was measured by means of the precision balance Mettler Toledo model PGH403-S with the density pack assembled (Mettler-Toledo International Inc., Switzerland). This weight, together with the mass density ρ^{fluid} of the immersion fluid (HBSS= $1g/cm^3$, and xylene= $0.88g/cm^3$), gives access to the volume of the wet macroscopic bone sample, according to

$$V^{wet} = \frac{M_{wet} - W_{immersed}/g}{\rho^{fluid}} \tag{2.3}$$

with g as the acceleration of gravity.

The volume of water contained in each of the tested macroscopic bone samples reads as

$$V^{H_2O} = \frac{M_{H_2O}}{\rho^{H_2O}} \tag{2.4}$$

Subsequently, the samples immersed in the HBSS were cleaned with distilled water in an ultrasonic bath for fifteen minutes, and the samples immersed in Xylene were first cleaned with a 30% ethanol solution and later cleaned with a 0.15 N saline solution in an ultrasonic bath for fifteen minutes.

Finally, the samples underwent demineralization treatment, in a 0.5 M Ethylenediaminetetraacetic acid (EDTA) solution with a pH 7.5. To accomplish the demineralization of the samples, each sample was immersed individually in a 0.5M EDTA solution three times for a seven-day period. After each of the immersions, the samples were cleaned with a 30% ethanol solution in an ultrasonic bath for fifteen minutes and subsequently, they were cleaned with distilled water in an ultrasonic bath for fifteen minutes. Later, the 0.5 M EDTA solutions of the three immersions from each sample were examined in an Inductively Coupled Plasma Optical Emission Spectrometer (ICP-OES), in order to detect the presence of Calcium, Magnesium, or Phosphorous. After not detecting any of the before-mentioned minerals in the last 0.5 M EDTA solutions, they are considered to be demineralized at this point. Following the last immersion in EDTA, the samples were treated with mass M_{org}. The mass of the organic content found within the bone samples M_{org} is the result of removing M_{H_2O} through the dehydration process and the mass of the mineral content found within the bone samples M_{HA} through the demineralization process from M_{wet}, as expressed by Eq [2.5]. Following the last immersion in EDTA, the samples were treated with increasing 30%, 50%, 70%, 90%, 98%, and 99% ethanol solutions. Thereafter, each of the samples was dehydrated under vacuum alongside with an orange silica gel desiccant until no change of mass was noticed. Since these demineralization and dehydration steps deprived the samples of any inorganic or water mass, they finally exhibited only the mass of organic matter, M_{org}. From the latter and previously determined mass of water, M_{H_2O}, the mass of mineral per sample can be computed according to

$$M_{HA} = M_{wet} - M_{H_2O} - M_{org} \tag{2.5}$$

This mineral readily gives access to the volume filled by minerals in the wet sample, through

$$V^{HA} = \frac{M_{HA}}{\rho^{HA}} \tag{2.6}$$

which, in turn, yields the organic volume as

$$V^{org} = V^{wet} - V^{H_2O} - V^{HA} \tag{2.7}$$

2.2.3 Porosity measurements by means of light microscopy

The amount of water located in the PV and PL can be calculated from the images obtained under the LM. The total area of the axial-polished face in the bone samples was divided into several smaller subareas. Therefore, the reconstructed subareas represent the complete image of the axial-polished face. The images,

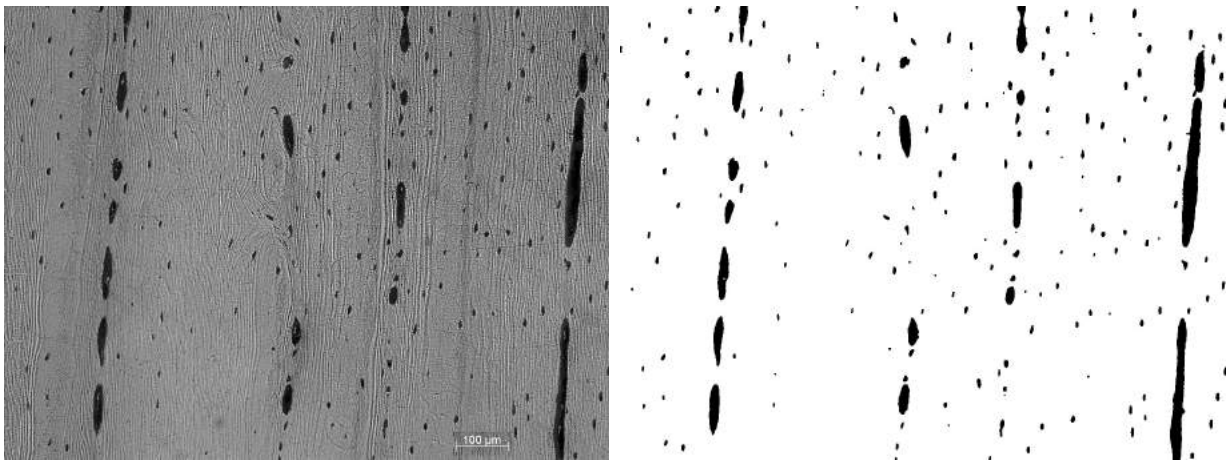

(a) Porosity of the axial-polished face image

(b) Analyzed porosity of Binary converted axial-polished face image

Figure 2.3: Determination of porosity from LM image 06/12 in sample F03

observed in [Figure 2.3a], were later processed in the Java-based ImageJ program (National Institutes of Health, USA). Each image was converted into an 8-bit image and filtered manually. The image segmentation was performed by a two-level threshold method. The first threshold employed user-defined observable features to remove micro-cracks, and non-lacunae or non-vascular pores artifacts. The *PV* and *PL* were portrayed as black areas. Subsequently, as demonstrated in [Figure 2.3b], a particle analyzer was applied to attain the number of pixels that represent each identified pore. Finally, the pores were divided into Vascular pores and Lacunae pores by setting an user-defined second threshold condition.

2.2.4 Evaluation of experimental data

The density of the hydrated bone samples ρ^{wet} was determined by relating V^{wet} and M_{wet}, as seen in Eq.[2.8].

$$\rho^{wet} = \frac{M_{wet}}{V^{wet}} \tag{2.8}$$

The results of the samples immersed in HBSS are expressed in Tables[2.1] and [2.3]. Considering the HBSS saturated samples, V^{wet} in Eq.[2.3] was calculated by inserting ρ^{fluid} for 1g/cc (ρ^{HBSS}). Meanwhile, the results of the samples immersed in Xylene are illustrated in Tables[2.2] and [2.4]. Here, ρ^{fluid} was substituted for 0.88 g/cc (ρ^{xylene}).

The mass of the bone contents are normally given in terms of the content weight fraction, and yields according to

$$WF_i = \frac{M_i}{M_{wet}}, \tag{2.9}$$

with $i = H_2O$ for the water content, $i = org$ for the organic content, and $i = HA$ for the mineral content within the bone samples. For the samples immersed in HBSS, M_{H_2O} in Eq.[2.9] is the mass of HBSS within M_{wet}. As for the samples immersed in Xylene, M_{H_2O} is the mass of Xylene within M_{wet}.

The relation presented in Eq.[2.10] is derived from Eq.[2.9].

$$WF_{H_2O} + WF_{org} + WF_{HA} = 1 \tag{2.10}$$

Equation [2.11] displays the ratio of V^{H_2O} and V^{wet}, calculating the volume fraction of the water content f_{H_2O}.

$$f_{H_2O} = \frac{V^{H_2O}}{V^{wet}} \tag{2.11}$$

The volume fraction of the mineral content f^{HA} is obtained by the ratio of V^{HA} and V^{wet}, as indicated by Eq.[2.12]. The mass density of the mineral content in Eq.[2.6] is ρ^{HA}= 3g/cc ([Robinson and Elliot, 1957]; [Gong et al., 1964]; [Lees and Escoubes, 1987]; [Hellmich et al., 2004]).

$$f_{HA} = \frac{V^{HA}}{V^{wet}} \tag{2.12}$$

According to Eq.[2.13], the volume fraction of the organic content f_{org} is obtained by the ratio of V^{org} and V^{wet}.

$$f_{org} = \frac{V^{org}}{V^{wet}} \tag{2.13}$$

f_{H_2O}, f_{HA}, and f_{org} constitute together the relation followed by Eq.[2.14].

$$f_{H_2O} + f_{HA} + f_{org} = 1 \tag{2.14}$$

The PV and PL calculated from the bone samples under the LM are computed to the volume fraction of the water content located within the Vascular pores $f_{H_2O,V}$ and to the volume fraction of the fluid content located within the Lacunae pores $f_{H_2O,PL}$ respectively.
The mass of the bone fluid content within the PV of the bone samples is typically given in terms of the weight fraction of fluid within the Vascular pores $WF_{H_2O,PV}$, as developed in Eq.[2.15].

$$WF_{H_2O,PV} = \frac{f_{H_2O,PV} \times V^{wet} \times \rho^{fluid}}{M_{wet}} \tag{2.15}$$

The outcome of Eq.[2.16] is the water within the PL weight fraction $WF_{H_2O,PL}$.

$$WF_{H_2O,PL} = \frac{f_{H_2O,PL} \times V^{wet} \times \rho^{fluid}}{M_{wet}} \tag{2.16}$$

2.2.5 Fluid contained within the ultra-porosity

PV and PL is organized with reference to the micro-structural level. The features at micro-meter scale μm i.e. Haversian canals and Lacunae, were reckon using LM. The volume of fluid that can not be acquired with the LM technique is treated as the volume of water within *Pultra*. Equation[2.17] denotes that $f_{H_2O,Pultra}$ is the remaining volume fraction after considering the micro-structural level.

$$f_{H_2O,Pultra} = f_{H_2O} - f_{H_2O,PV} - f_{H_2O,PL} \tag{2.17}$$

Equation[2.18] expresses the fluid within *Pultra* weight fraction of the sample.

$$WF_{H_2O,Pultra} = WF_{H_2O} - WF_{H_2O,PV} - WF_{H_2O,PL} \tag{2.18}$$

Table[2.5] describes the porosity and weight fractions of the ultra-structure level for the samples immersed in HBSS. Meanwhile, Table[2.6] demonstrate the calculated porosity and weight fractions of the ultra-structural level for samples immersed in Xylene. This data quantifies the amount of water at the smallest dimensional porosity.

The volume fractions of water content within the extracellular bone matrix $f^{ultra}_{H_2O}$ can be calculated from Equation [2.19], and the results can be seen in Tables [2.5] and [2.6].

$$f^{ultra}_{H_2O} = \frac{f_{H_2O,Pultra}}{1 - f_{H_2O,PV} - f_{H_2O,PL}} \tag{2.19}$$

Figure 2.4: Average hydration curve of bone samples

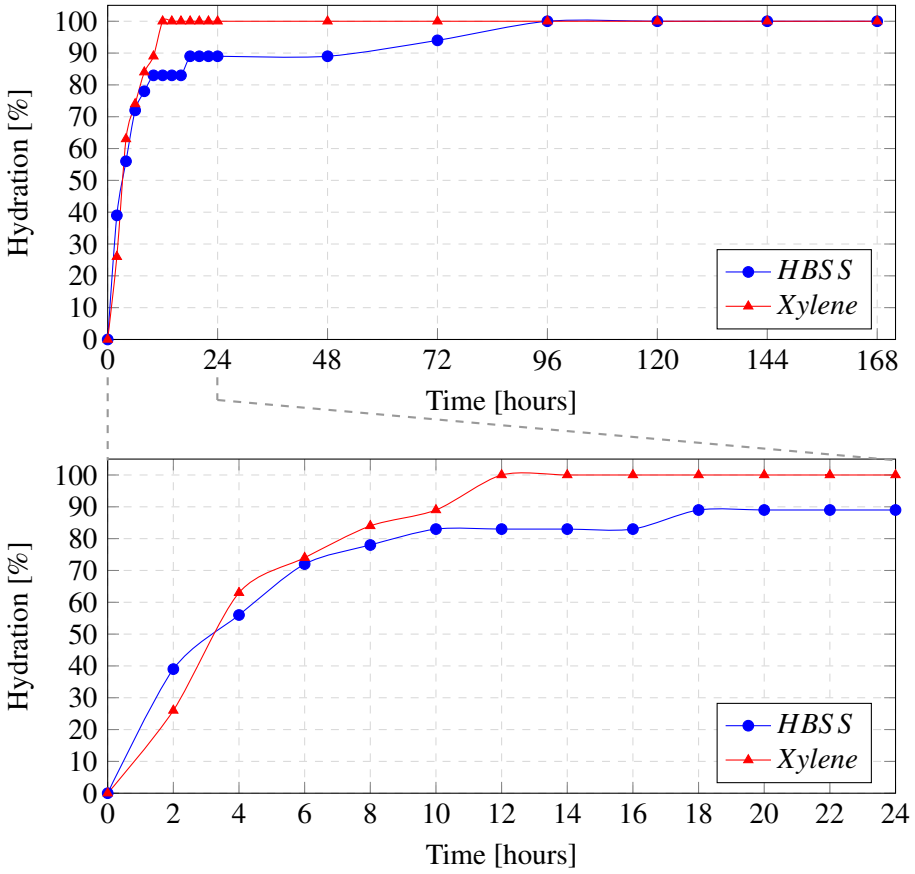

Equation [2.20] describes the volume fractions of mineral content within the extracellular bone matrix f_{HA}^{ultra} and the results can be seen in Tables [2.5] and [2.6].

$$f_{HA}^{ultra} = \frac{f_{HA}}{1 - f_{H_2O,PV} - f_{H_2O,PL}} \tag{2.20}$$

Finally, the volume fractions of organic content within the extracellular bone matrix f_{org}^{ultra} can be computed from Equation [2.21], and the results can be seen in Tables [2.5] and [2.6].

$$f_{org}^{ultra} = \frac{f_{org}}{1 - f_{H_2O,PV} - f_{H_2O,PL}} \tag{2.21}$$

2.3 Results and Discussion

Table 2.1: Density and Weight Fractions of samples immersed in HBSS

Sample	WF_{H_2O} Eq.[2.9]	$WF_{H_2O,PV}$ Eq.[2.15]	$WF_{H_2O,PL}$ Eq.[2.16]	WF_{org} Eq.[2.9]	WF_{HA} Eq.[2.9]	ρ^{wet} (g/cc) Eq.[2.8]
F01	0.0961	0.0141	0.0132	0.2227	0.6812	1.90
F02	0.1078	0.0225	0.0094	0.1796	0.7126	2.06
F03	0.2517	0.0144	0.0111	0.1958	0.5524	1.81
F04	0.0848	0.0153	0.0096	0.2232	0.6920	2.22
F05	0.1007	0.0153	0.0123	0.2282	0.6711	2.04
F06	0.0960	0.0129	0.0088	0.2400	0.6640	1.95
F07	0.0966	0.0142	0.0095	0.1862	0.7172	1.79
F08	0.0964	0.0164	0.0106	0.2169	0.6867	2.13
F09	0.1420	0.0160	0.0096	0.2160	0.6420	1.93
F10	0.1364	0.0168	0.0081	0.2143	0.6494	2.08
F11	0.0968	0.0136	0.0103	0.1935	0.7097	2.04
F12	0.0926	0.0143	0.0083	0.2037	0.7037	2.00
F13	0.0995	0.0177	0.0086	0.2189	0.6816	2.01
F14	0.1090	0.0181	0.0085	0.1538	0.7372	1.93
F15	0.1040	0.0181	0.0089	0.2197	0.6763	1.97
F16	0.0977	0.0134	0.0093	0.2047	0.6977	1.94
F17	0.1161	0.0193	0.0097	0.2000	0.6839	1.96
F18	0.1087	0.0193	0.0109	0.1957	0.6957	1.97
mean	0.1129	0.0161	0.0098	0.2063	0.6808	1.99

Table 2.2: Density and Weight Fraction of samples immersed in Xylene

Sample	WF_{H_2O} Eq.[2.9]	$WF_{H_2O,PV}$ Eq.[2.15]	$WF_{H_2O,PL}$ Eq.[2.16]	WF_{org} Eq.[2.9]	WF_{HA} Eq.[2.9]	ρ^{wet} (g/cc) Eq.[2.8]
FX01	0.1735	0.0127	0.0071	0.2041	0.6224	1.92
FX02	0.1500	0.0158	0.0073	0.1833	0.6670	1.99
FX03	0.1333	0.0163	0.0088	0.2095	0.6571	1.93
FX04	0.1089	0.0163	0.0089	0.1980	0.6931	1.81
FX05	0.1250	0.0151	0.0075	0.1985	0.6765	1.84
FX06	0.1389	0.0111	0.0076	0.1759	0.6852	1.83
mean	0.1383	0.0145	0.0079	0.1949	0.6680	1.90

Table 2.3: Volume Fractions of samples immersed in HBSS

Sample	f_{H_2O} Eq.[2.11]	$f_{H_2O,PV}$ [LM]	$f_{H_2O,PL}$ [LM]	f_{org} Eq.[2.13]	f_{HA} Eq.[2.12]
F01	0.1849	0.0271	0.0254	0.3782	0.4370
F02	0.2222	0.0464	0.0193	0.2881	0.4897
F03	0.4557	0.0260	0.0202	0.2110	0.3333
F04	0.1881	0.0340	0.0214	0.3003	0.5116
F05	0.2055	0.0312	0.0252	0.3379	0.4566
F06	0.1875	0.0253	0.0171	0.3802	0.4323
F07	0.1728	0.0254	0.0170	0.3992	0.4280
F08	0.2051	0.0348	0.0225	0.3077	0.4872
F09	0.2738	0.0309	0.0185	0.3135	0.4127
F10	0.2838	0.0349	0.0168	0.2658	0.4505
F11	0.1974	0.0277	0.0211	0.3202	0.4825
F12	0.1852	0.0287	0.0165	0.3457	0.4691
F13	0.2000	0.0355	0.0174	0.3433	0.4567
F14	0.2099	0.0349	0.0164	0.3169	0.4733
F15	0.2045	0.0355	0.0175	0.3523	0.4432
F16	0.1892	0.0259	0.0180	0.3604	0.4505
F17	0.2278	0.0378	0.0191	0.3249	0.4473
F18	0.2143	0.0345	0.0214	0.3286	0.4571
mean	0.2227	0.0320	0.0195	0.3263	0.4510

Table 2.4: Volume Fractions of samples immersed in Xylene

Sample	f_{H_2O} Eq.[2.11]	$f_{H_2O,PV}$ [LM]	$f_{H_2O,PL}$ [LM]	f_{org} Eq.[2.13]	f_{HA} Eq.[2.12]
FX01	0.3778	0.0277	0.0156	0.2246	0.3976
FX02	0.3396	0.0358	0.0165	0.2176	0.4428
FX03	0.2917	0.0356	0.0193	0.2867	0.4217
FX04	0.2245	0.0335	0.0183	0.3565	0.4190
FX05	0.2615	0.0316	0.0158	0.3233	0.4152
FX06	0.2885	0.0231	0.0158	0.2941	0.4174
mean	0.2893	0.0312	0.0169	0.2883	0.4224

Table 2.5: Ultra-structure level porosity and weight fractions of samples immersed in HBSS

Sample	$f_{H_2O,Pultra}$ Eq.[2.17]	$f_{H_2O}^{ultra}$ Eq.[2.19]	f_{org}^{ultra} Eq.[2.21]	f_{HA}^{ultra} Eq.[2.20]	$WF_{H_2O,Pultra}$ Eq.[2.18]
F01	0.1324	0.1397	0.3991	0.4612	0.0688
F02	0.1565	0.1675	0.3083	0.5242	0.0759
F03	0.4096	0.4294	0.2212	0.3495	0.2263
F04	0.1327	0.1405	0.3179	0.5415	0.0598
F05	0.1491	0.1580	0.3581	0.4839	0.0730
F06	0.1451	0.1515	0.3970	0.4514	0.0743
F07	0.1305	0.1362	0.4168	0.4469	0.0729
F08	0.1478	0.1567	0.3264	0.5168	0.0694
F09	0.2243	0.2360	0.3298	0.4341	0.1163
F10	0.2321	0.2448	0.2802	0.4750	0.1115
F11	0.1486	0.1562	0.3366	0.5072	0.0728
F12	0.1400	0.1466	0.3620	0.4913	0.0700
F13	0.1471	0.1553	0.3625	0.4822	0.0732
F14	0.1585	0.1671	0.3340	0.4989	0.0823
F15	0.1515	0.1600	0.3720	0.4680	0.0771
F16	0.1453	0.1519	0.3769	0.4711	0.0750
F17	0.1710	0.1813	0.3445	0.4742	0.0871
F18	0.1584	0.1678	0.3480	0.4842	0.0804
mean	0.1711	0.1804	0.3439	0.4757	0.0870

Table 2.6: Ultra-structure level porosity and Weight fractions of samples immersed in Xylene

Sample	$f_{H_2O,Pultra}$ Eq.[2.17]	$f_{H_2O}^{ultra}$ Eq.[2.19]	f_{org}^{ultra} Eq.[2.21]	f_{HA}^{ultra} Eq.[2.20]	$WF_{H_2O,Pultra}$ Eq.[2.18]
FX01	0.3345	0.3497	0.2347	0.4156	0.1536
FX02	0.2871	0.3032	0.2296	0.4671	0.1269
FX03	0.2367	0.2505	0.3033	0.4461	0.1082
FX04	0.1727	0.1821	0.3759	0.4419	0.0838
FX05	0.2142	0.2249	0.3393	0.4358	0.1024
FX06	0.2495	0.2596	0.3060	0.4343	0.1201
mean	0.2491	0.2617	0.2982	0.4402	0.0942

The motivation of this paper is to contribute to an explanation of the quantitative and constructive aspects of the fluid within bone. The results provide a significant addition and validation to previous experiments performed by [Robinson and Elliot, 1957] and [Lees et al., 1979b]. We accomplished weight fractions (for HBSS: WF_{H_2O}=0.1129; WF_{org}=0.2063; WF_{HA}=0.6808, and for Xylene: WF_{H_2O}=0.1383; WF_{org}=0.1949; WF_{HA}=0.6680) closely matching the weight fractions of ([Lees et al., 1979b]) (WF_{H_2O}=0.1250; WF_{org}=0.2210; WF_{HA}=0.6530).

2.3.1 Fluid selection

The polarity determines the surface tension property of a fluid. In the case of polar fluids e.g. [H_2O] and HBSS, the molecules tend to be attracted to each other. This cohesive force creates a "film" around the surface of the bone. The excess of fluid contained within the "film" influences the measured mass of fluid in a saturated sample. To solve this issue, we wiped the excess of HBSS from the surface of the samples. To determine if this method removed a significant amount of fluid from the outer surface pores, we adopted a second non-polar fluid i.e. Xylene. Non-polar fluids have lower surface tensions than polar fluids. Therefore, the excess of non-polar fluid at the surface of the bone is not as difficult to remove as of the polar fluid. The obtained results demonstrated that there is no significant difference between using both fluids and procedures.

[Newman and Newman, 1958] claimed that the chemical composition and pH are the same for the bone fluid located either in the *PV*, *PL*, or *Pultra*. Consequently, we employed the properties of HBSS or Xylene to calculate the volume fractions and weight fractions when the samples were immersed in each of the two fluids. We tested in the (ICP-OES) the "blank" fluids to detect the existence of mineral content. Therefore, either the distilled water, 0.5M EDTA, HBSS, or Xylene supplemented the bone samples with Calcium, Magnesium, or Phosphorous during the experiments.

2.3.2 Porosity

Rather than just measuring the porosity in selected areas, we calculated the complete *PV* and *PL* at the polished face of each sample. The reason for the implementation of this approach is that we observed a high porosity variation between locations in the same sample. In this context, [Atkinson and Hallsworth, 1983] stated that the vascular porosity could vary significantly between specimens in the species at the same site and of the same age group. All the more, [Dong et al., 2013] noticed porosities ranging from 3% to 33% in a single bone sample.

Considering LM related techniques, the obtained $f_{H_2O,PV}$ (for HBSS: 0.0320 and for Xylene: 0.0312) and $f_{H_2O,PL}$ (for HBSS: 0.0195 and for Xylene: 0.0169) were similar compared to the results reached by [Schaffler and Burr, 1988] (*PV*=0.040) and [Fritsch and Hellmich, 2007] (*PV*=0.030 and *PL*=0.021) on Bovine specimens. The results remained akin to the porosities attain by [Sietsema, 1995] (*PV*=0.030) [Frost, 1960] (*PL*=0.023) of Human specimens and [Sietsema, 1995] (*PV*=0.023) of Canine specimens.

In addition to the two-dimensional 2D approaches to obtain the bone porosity, there are several studies employing three-dimensional 3D means to acquire the pore volume fractions. At the European Synchrotron Radiation Facility in Grenoble, France, [Hesse et al., 2013] used Synchrotron Radiation micro-tomography (SR-μcT) to study the morphology and quantification of *PL*. The *PL* of the Human specimens were measured in the jaw, nevertheless the result of *PL*=0.020 [Hesse et al., 2013] was not that distinct from our data. Using micro-computed tomography μcT, [Palacio-Mancheno et al., 2014] constructed 3D tibia images of Murine specimens. The porosities obtained with μcT (*PV*=0.040 and *PL*=0.020) denoted a similitude to the results reflected in this paper.

Finally, with the results of the weight fractions and volume fractions we revealed the partition of bone fluid at the micro-structural and ultra-structural scale. Being bone a composite material, the allocation and quantification of fluid, along with the mineral and organic contents, are essential to a better understanding of the reaction of bones toward forces On the one hand, this is of particular interest as regards upscaling of mechanical properties from the elementary constituents, via the different organizational levels of bone, up to the macroscopic level; this concerns elasticity [Hellmich and Ulm, 2002],

[Hellmich et al., 2004], [Fritsch and Hellmich, 2007], strength [Fritsch et al., 2009], and viscoelasticty [Eberhardsteiner et al., 2014]. On the other hand, the precise quantification of fluid-filled pore spaces is essential for downscaling macroscopic strain and stress states, down to different pore pressures triggering the local cell behavior [Scheiner et al., 2016].

CHAPTER 3

CHAPTER 3

Additional experimental and technical aspects

Additional experimental and technical aspects

Authored by: Luis Zelaya-Lainez[1], Winfried Nischkauer[2], and Christian Hellmich[1]

3.1 Introduction

Bone is a composite biomaterial, and therefore contains several materials along its hierarchical structure [Katz et al., 1984]. It is well known that the mechanical properties of bone depend crucially on the material composition in terms of the mineral and organic contents [Hellmich and Ulm, 2002], [Fritsch and Hellmich, 2007], but less is known about the bone fluid content [Weiner and Wagner, 1998].

The bone fluid content is referred to the water located within the several pore spaces in bone [Cowin, 1999]. Such fluid content can be determined by the experimental hydration and dehydration of the bone samples. The calculation of the mineral and the organic content of the bone samples prompted the demineralization process of such.

This document describes a method of the experimental partition of the bone contents created originally by Sidney Lees in the 1970's [Lees et al., 1979b]. This method is characterized by a multi-state approach. The first state consist of the original hydrated bone. The second state consist of the dehydration of the original hydrated bone. The third state consist of the demineralization and then again dehydration of the samples.

3.2 Materials and Methods

Sample Preparation

The twenty-seven bone samples were harvested from a healthy bovine laminar femur. The bovine bone was purchased at a local butcher. All the samples were cut from the femur at the same cortical midsection with a handsaw. The Periosteum, the Endosteum, and the bone marrow were removed using a scalpel and a 5% ethanol solution. After cleaning the bone section with distilled water in an ultrasonic bath for five minutes, the bone section was stored in a frozen state at -20 centigrades for four days. The section was cut in two smaller sections of 8.00 mm at the transverse orientation each, then the smaller sections were cut

[1]Institute for Mechanics of Materials and Structures, Vienna University of Technology (TU Wien), Karlsplatz 13/E202, 1040 Vienna, Austria.

[2]Institute of Chemical Technologies and Analytics, Division of Instrumental Analytical Chemistry, Vienna University of Technology (TU Wien), Getreidemarkt 9/164, 1060 Vienna, Austria.

longitudinally in halves on a diamond blade saw (EXAKT Systeme, Germany). The sections were later cut into the individual twenty-seven samples and the trabecular inner-part of each sample was removed on a Isomet low speed saw (Buehler, USA) using a 1270.00 mm diameter and 0.40 mm thick cubic Boron Nitride (cBN) blade rotating at 150 rpm, using distilled water as a cooling medium. Next, the samples were stored in a 0.15 N saline solution at room temperature.

3.3 Measurements

Original wet state

The samples were hydrated with Hank's Balanced Salt Solution (HBSS) until no change in mass was noticed. The samples immersed in the HBSS were wiped free of surface water with Rotizell Tissues (Carl Roth GmbH, Germany) before measuring their mass. The samples are at this point considered to be hydrated.

Following the hydration of the samples, the volume V^{wet} of each individual sample was calculated in Eq.[3.1], with the Archimedes' Principle. The mass of each sample during immersion $M_{immersed}$ and the mass of each sample during withdrawal from the fluids M_{wet} were obtained with the precision balance Mettler Toledo model PGH403-S with the density pack assembled (Mettler-Toledo International Inc., Switzerland). The difference between M_{wet} and the perceivable reduced $M_{immersed}$ during the immersion in a fluid with density ρ^{HBSS} is the mass of the displaced fluid.

$$V^{wet} = \frac{M_{wet} - M_{immersed}}{\rho^{HBSS}} \tag{3.1}$$

The volume of water content V^{H_2O} contained within the samples was obtained by relating M_{H_2O} and ρ^{HBSS}, as presented by Eq.[3.2]. ρ^{HBSS} in Eqs.[3.1] and [3.2] is the density of HBSS.

$$V^{H_2O} = \frac{M_{H_2O}}{\rho^{HBSS}} \tag{3.2}$$

Dehydrated state

Following the hydration of the bone samples in HBSS, each of the samples was dehydrated under vacuum alongside with an orange silica gel desiccant. The mass from each of the samples was monitored in a precision balance Mettler Toledo model PGH403-S (Mettler-Toledo International Inc., Switzerland) until no change was noticed, that being around the seventh day. At this point, the samples are considered to be dehydrate and to have a mass M_{dry}, i.e. the bone samples are dry in equilibrium with a water-free environment and at room temperature. Eq.[3.3] states that the mass of water M_{H_2O} contained within each sample is the difference between M_{wet} of the fluid saturated sample and M_{dry} of the dehydrated sample.

$$M_{H_2O} = M_{wet} - M_{dry} \tag{3.3}$$

Demineralized state

The samples were demineralized using EDTA solution. To accomplish the demineralization of the samples, each sample was immersed individually in a 0.5M EDTA pH 7.5 solution three times for a seven-day period. After each of the immersions, the samples were cleaned with a 30% ethanol solution in an ultrasonic bath for fifteen minutes and subsequently, they were cleaned with distilled water in an ultrasonic bath for fifteen minutes. Later, the 0.5 M EDTA solutions of the three immersions from each sample were examined in an ICP-OES in order to detect the presence of Calcium, Magnesium, or Phosphorous. After not detecting any of the before-mentioned minerals in the last 0.5 M EDTA solutions, the samples are considered to be demineralized at this point and to have a mass M_{org}. The mass of the organic content found within the bone samples M_{org} is the result of removing M_{H_2O} through the dehydration process

and the mass of the mineral content found within the bone samples M_{HA} through the demineralization process from M_{wet}, as expressed by Eq.[3.4]. Following the last immersion, the samples were treated with increasing 30%, 50%, 70%, 90%, 98%, and 99% ethanol solutions for a seven-day period each. Finally, each of the samples was dehydrated under vacuum alongside with an orange silica gel desiccant until no change of mass was noticed.

$$M_{org} = M_{wet} - M_{H_2O} - M_{HA} \tag{3.4}$$

Equation [3.5] determines the volume of mineral content V^{HA} contained within the samples by relating M_{HA} and the mass density of the mineral content ρ^{HA}.

$$V^{HA} = \frac{M_{HA}}{\rho^{HA}} \tag{3.5}$$

As developed in Eq.[3.6], the volume of organic content V^{org} of the samples was the vestigial volume after dehydrating and demineralizing each sample with volume V^{wet}.

$$V^{org} = V^{wet} - V^{H_2O} - V^{HA} \tag{3.6}$$

Density, Weight Fractions, and Volume Fractions

The density of the hydrated bone samples ρ^{wet} was determined by relating V^{wet} and M_{wet}, as seen in Eq.[3.7].

$$\rho^{wet} = \frac{M_{wet}}{V^{wet}} \tag{3.7}$$

The mass of the bone contents are normally given in terms of the content weight fraction, and yields according to

$$WF_i = \frac{M_i}{M_{wet}}, \tag{3.8}$$

with $i = H_2O$ for the water content, $i = org$ for the organic content, and $i = HA$ for the mineral content within the bone samples. For the samples immersed in HBSS, M_{H_2O} in Eq.[3.8] is the mass of HBSS within M_{wet}. As for the samples immersed in Xylene, M_{fluid} is the mass of Xylene within M_{wet}. The relation presented in Eq.[3.9] is derived from Eq.[3.8].

$$WF_{H_2O} + WF_{org} + WF_{HA} = 1 \tag{3.9}$$

Equation [3.10] displays the ratio of V^{H_2O} and V^{wet}, calculating the volume fraction of the water content f^{fluid}.

$$f_{H_2O} = \frac{V^{H_2O}}{V^{wet}} \tag{3.10}$$

The volume fraction of the mineral content f_{HA} is obtained by the ratio of V^{HA} and V^{wet}, as indicated by Eq.[3.11]. The mass density of the mineral content in Eq.[3.5] is ρ^{HA}= 3g/cc [Robinson and Elliot, 1957], [Gong et al., 1964], [Hellmich et al., 2004].

$$f_{HA} = \frac{V^{HA}}{V^{wet}} \tag{3.11}$$

According to Eq.[3.12], the volume fraction of the organic content f_{org} is obtained by the ratio of V^{org} and V^{wet}.

$$f_{org} = \frac{V^{org}}{V^{wet}} \tag{3.12}$$

f_{H_2O}, f_{HA}, and f_{org} constitute together the relation followed by Eq.[3.13].

$$f_{H_2O} + f_{HA} + f_{org} = 1 \tag{3.13}$$

3.4 Results and Discussion

The motivation of this technical report is provide a validation to previous experiments performed by [Lees et al., 1979b]. We accomplished weight fractions (for HBSS: WF_{H_2O}=0.12; WF_{org}=0.21; WF_{HA}=0.67) closely matching the weight fractions of [Lees et al., 1979b] (WF_{H_2O}=0.13; WF_{org}=0.22; WF_{HA}=0.65).

We tested in the ICP-OES the "blank" fluids to detect the existence of any mineral content. Therefore, either the distilled water, 0.5M EDTA, or HBSS supplemented the bone samples with Calcium, Magnesium, or Phosphorous during the experiments. Furthermore, to prevent contamination, the surfaces and instruments in contact with the bone samples were previously cleaned with a nitric acid solution.

3.4.1 Methodology at the laboratory

The sample preparation and the measurements described in this work were achieved in the Interfacultary Laboratory for Micro- and Nanomechanics of Biological and Biomimetical Materials[3]. While the detection using an Inductively Coupled Plasma Optical Emission Spectrometer of the minerals within the Ethylenediaminetetraacetic acid solutions after the demineralization process was performed with the cooperation of the research group Inorganic Trace Analysis [4]

To prevent any contamination, all the surfaces in the laboratory were cleaned with Bacillol (Hartmann, Germany), and the instruments in contact with the bone specimens were disinfected with a nitric acid solution. The distilled water, EDTA, sodium hydroxide pellets, the HBSS, and xylene used in the experiments were all from the same source (Carl Roth, Germany). All of these procedures were made to prevent outer contamination affecting our results or the variation due to the utilization of different chemicals.

Before using the xylene isomer, the occupational health department[1] was informed to obtain allowance. According to European Union regulation[5], xylene $[CH_3]_2C_6H_4$ with molar mass of 106.17 $\frac{grams}{mol}$ is a harmful substance, and therefore a special personal protective equipment (PPE) is required to handle it.

The EDTA solution used to demineralize the bone samples was prepared with EDTA disodium salt $C_{10}N_{16}[N_2O_8]$ with molar mass of 292.25 $\frac{grams}{mol}$, distilled water, and was brought to the required pH 7.5 with sodium hydroxide pellets $NaOH$ with molar mass 39.997 $\frac{grams}{mol}$. The EDTA salt and the distilled water were stirred in a magnetic stirrer R1000 (Carl Roth, Germany). The stirring velocity has to be set fast to prevent solidification. The stirring of the mixture requires several hours. Once the salt is dissolved completely in the distilled water, sodium hydroxide pellets are poured slowly into the solution, while the stirrer continues engaged. To monitor the instant pH and temperature, a Mettler Toledo Fe20/EI 20 (Mettler-Toledo International Inc., Switzerland) was used. A high temperature can provoke that the chemicals in the solution react too fast, and an undesired foam is created. The EDTA solutions for each of the three bathes were formulated at the same time. The several bathes is due to the fact that the concentration of demineralizing agent will be depleted as it combines with the calcium, phosphorous, or magnesium ions. The solutions had to be renewed several times during the demineralization process, and a sufficient amount of solution had to be deposit along with each bone sample, although the ICP-OES does not requires a large amount of EDTA solution sample. To prevent the misguiding detection of mineral, the samples were meticulously cleaned with ethanol and distilled water solution between each of the EDTA bathes, as explained in chapter 2.

In order to observe PV and PL of the cross-section face from the bone samples under the LM and in a FESEM, the cross-section face of each specimen had to be polished in a two-step polishing process, explained in chapter 2. As an additional entry, we would like to comment on the difference between polishing a frozen sample and a non-frozen sample. The frozen samples showed a better contrivance to the polishing procedures. The frozen samples took less time at each of the two polishing steps, and the results were cleaner images, due to the introduction of less machining scratches. For the polishing

[3] Vienna University of Technology (TU WIEN)

[4] Institute of Chemical Technologies and Analytics from the Vienna University of Technology (TU WIEN).

[5] CLP regulation: Regulation (EC) No 1272/2008

procedures, [Lees et al., 1979b] embedded the samples in a resin. We decided not to introduce any more chemicals to our procedures. We were also concerned of blocking an unknown amount of pores with the resin, which could affect our results of hydration. To solve this problem, a custom-made holder was designed with the Computer Aided Design program SolidWorks (Dassault Systèmes SolidWorks, France) and elaborated at the Laboratorium für makroskopische Werkstoffversuche[6].

3.4.2 The relationship between the three major components

The proportions of organic, mineral, and bone fluid contents can vary widely between the different types of bone [Robinson and Elliot, 1957]. According to [Weiner and Wagner, 1998], the volume fraction of the organic content remains basically the same, but is the mineralization degree of the mineralized bone matrix and the volume fraction of bone fluid found within wet bone that change at expense of reducing the volume fraction between themselves. This variability can be further seen in the different porosities within a single human bone specimen observed by [Dong et al., 2013]. Furthermore, we could observed a great difference between the porosities in the samples by just moving a couple hundred micrometers.

The weight fractions and volume fractions for each of the three major components found within bovine bone specimen can be observed in Tables[3.1 and 3.2].

[6]Institute for mechanics of materials and structure from the Vienna University of Technology (TU Wien)

Table 3.1: Density and Weight Fractions of samples immersed in HBSS

Sample	WF_{H_2O} Eq.[3.8]	WF_{org} Eq.[3.8]	WF_{HA} Eq.[3.8]	ρ^{wet} (g/cc) Eq.[3.7]
C01	0.13	0.20	0.67	1.88
C02	0.11	0.21	0.68	1.90
C03	0.13	0.20	0.67	2.14
C04	0.10	0.20	0.70	1.82
C05	0.12	0.24	0.64	1.70
C06	0.13	0.19	0.68	2.29
C07	0.13	0.20	0.67	2.14
C08	0.11	0.22	0.67	2.00
C09	0.13	0.19	0.68	2.29
D01	0.12	0.25	0.63	2.00
D02	0.16	0.17	0.67	2.00
D03	0.14	0.18	0.68	1.69
D04	0.07	0.22	0.71	2.00
D05	0.10	0.17	0.73	2.14
D06	0.07	0.21	0.72	1.65
D07	0.10	0.22	0.68	1.79
D08	0.10	0.20	0.70	2.00
D09	0.11	0.22	0.67	2.00
E01	0.17	0.23	0.60	2.00
E02	0.09	0.22	0.69	2.13
E03	0.14	0.18	0.68	1.87
E04	0.09	0.21	0.70	1.89
E05	0.11	0.22	0.67	1.93
E06	0.13	0.22	0.66	2.00
E07	0.10	0.23	0.68	2.07
E08	0.13	0.22	0.65	2.00
E09	0.15	0.23	0.62	2.17
mean	0.12	0.21	0.67	1.99

Table 3.2: Volume Fractions of samples immersed in HBSS

Sample	f_{H_2O} Eq.[3.10]	f_{org} Eq.[3.12]	f_{HA} Eq.[3.11]
C01	0.25	0.33	0.42
C02	0.20	0.37	0.43
C03	0.28	0.24	0.48
C04	0.18	0.40	0.42
C05	0.20	0.43	0.37
C06	0.29	0.19	0.52
C07	0.29	0.24	0.47
C08	0.22	0.33	0.45
C09	0.29	0.19	0.52
D01	0.25	0.33	0.42
D02	0.33	0.22	0.45
D03	0.23	0.39	0.38
D04	0.14	0.38	0.48
D05	0.21	0.26	0.53
D06	0.12	0.49	0.39
D07	0.19	0.38	0.43
D08	0.20	0.33	0.47
D09	0.22	0.33	0.45
E01	0.33	0.27	0.40
E02	0.20	0.31	0.49
E03	0.27	0.31	0.42
E04	0.17	0.39	0.44
E05	0.22	0.35	0.43
E06	0.25	0.31	0.44
E07	0.20	0.33	0.47
E08	0.25	0.31	0.44
E09	0.33	0.22	0.45
mean	0.23	0.32	0.45

Porosity observations under LM

The following selection of LM images represent a small part of the whole collection of LM images obtained during the experiment phase of this work. To calculate the PV and PL of our bone samples a Zeiss Axio Imager LM with a mounted AxioCam MRc5 digital camera (Carl Zeiss AG, Germany) was used. The LM images have a resolution of 1292×968 pixels^2.

To identify approximately the sizes of PV and PL, some additional samples were observed in a FESEM at USTEM[7]. The FESEM resolutions of 3072x2207 pixels^2 and the FESEM magnification capability permitted a better identification of the pores and their sizes than LM. The drawbacks of the FESEM, and SEM, is that the areas of interest have to relatively smaller than in LM. The work to accomplish that performed by the LM, can take more time if performed by the FESEM, as well as more care when moving the area of focus is necessary with the FESEM. The bone samples had to be sputtered with a conductive layer which also could made some pores not visible. The sputtering with a thin gold-palladium layer was performed in a Sputter Coater Quorum Q150T S^3 (Quorum technologies, UK). Due to the methodology used in this work i.e. acquiring the PV and PL of the whole cross section area from each of the bone samples, the FESEM or SEM technology was just useful for identification, and not for quantification.

As a reminder, all the images are from the same bone specimen, and a magnification of 100x was used. The structural differences between different location of the same bone specimen can be observed in the following collection of images. The distances between these samples is just about a couple of μm.

[7]University Service Center for Transmission Electron Microscopy from the Vienna University of Technology (TU WIEN)

APPENDIX

APPENDIX A

Light Microscope images

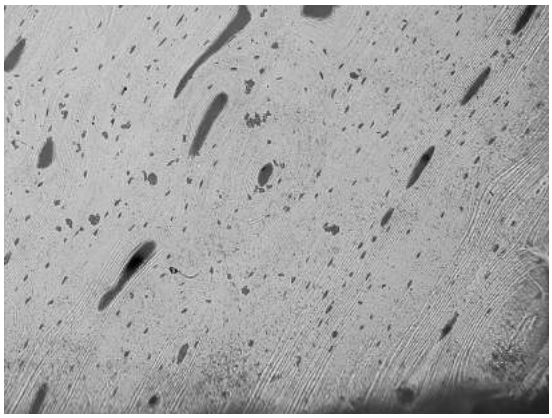

(a) Porosity of the axial-polished face image sample F01 part 1/21

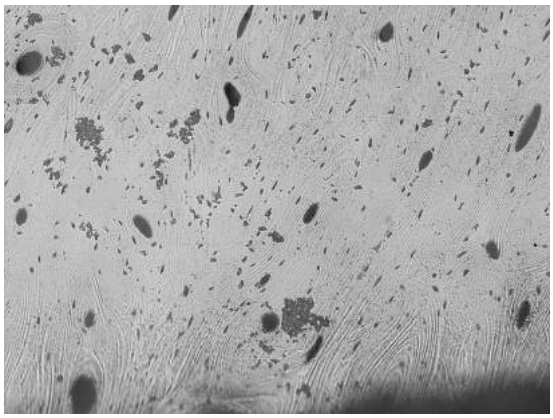

(b) Porosity of the axial-polished face image sample F01 part 2/21

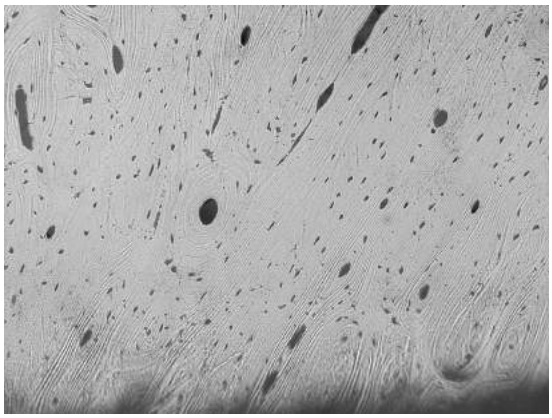

(c) Porosity of the axial-polished face image sample F01 part 3/21

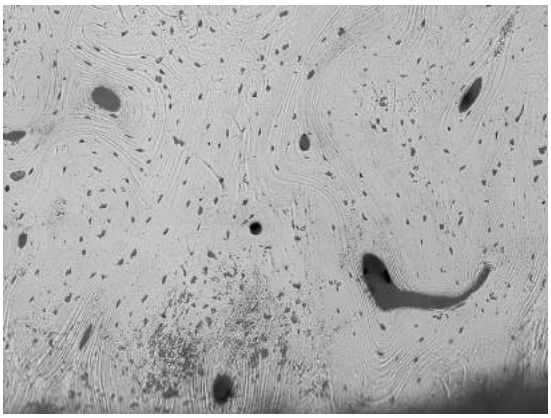

(d) Porosity of the axial-polished face image sample F01 part 4/21

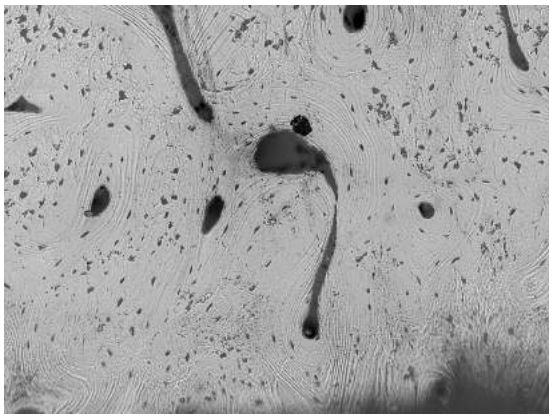

(e) Porosity of the axial-polished face image sample F01 part 5/21

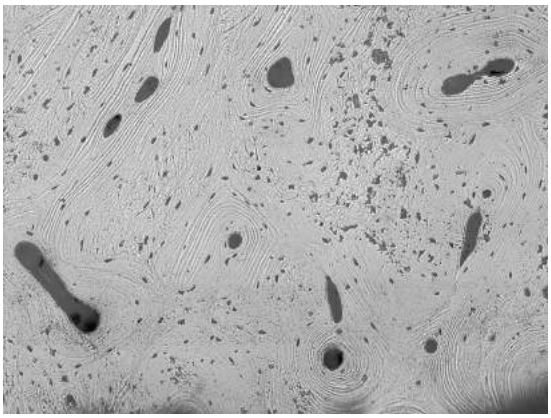

(f) Porosity of the axial-polished face image sample F01 part 6/21

Figure A.1: Porosity of axial-polished face from sample F01. LM magnification of 100x

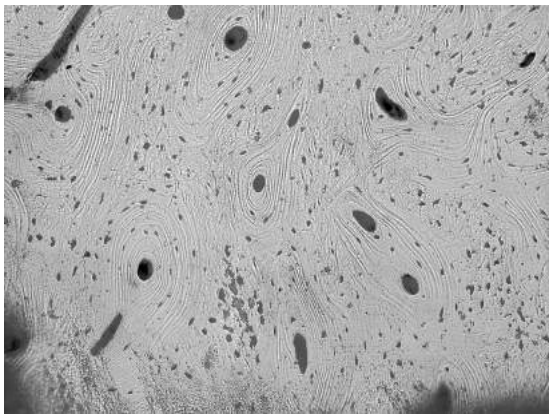

(a) Porosity of the axial-polished face image sample F01 part 7/21

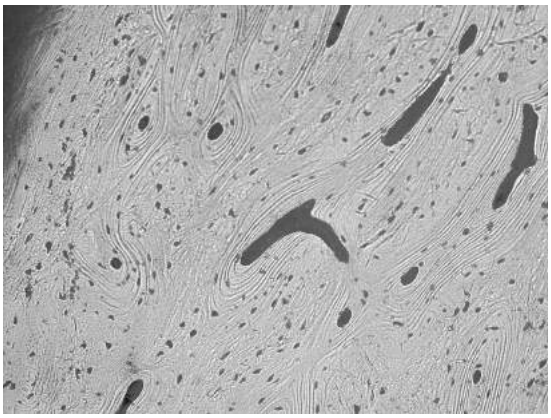

(b) Porosity of the axial-polished face image sample F01 part 8/21

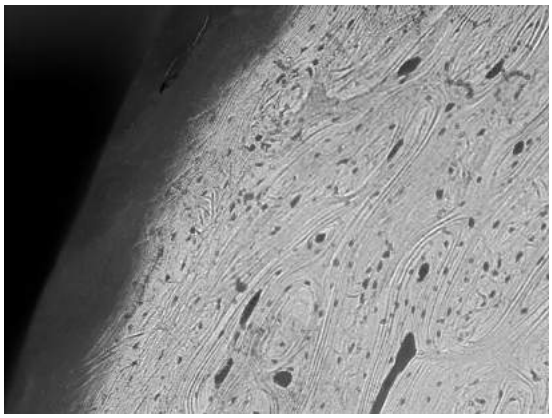

(c) Porosity of the axial-polished face image sample F01 part 9/21

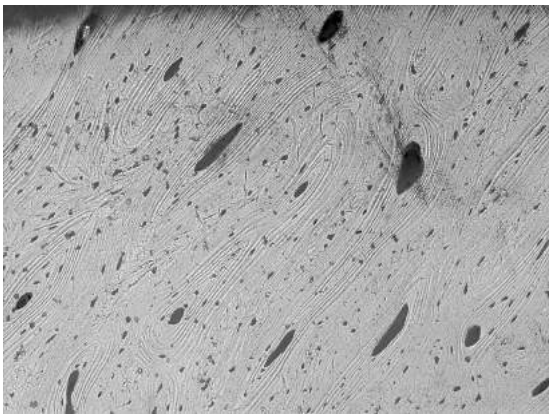

(d) Porosity of the axial-polished face image sample F01 part 10/21

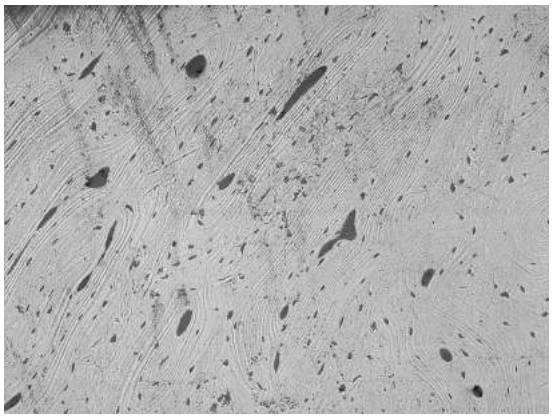

(e) Porosity of the axial-polished face image sample F01 part 11/21

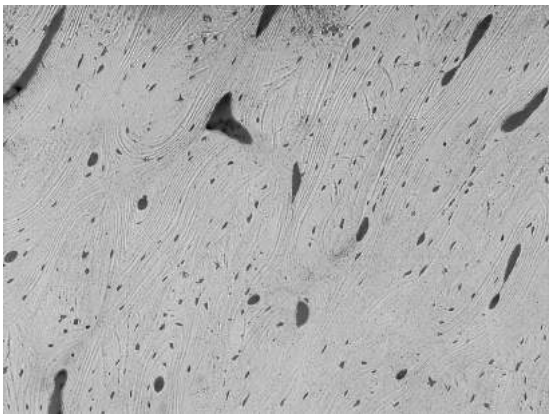

(f) Porosity of the axial-polished face image sample F01 part 12/21

Figure A.2: Porosity of axial-polished face from sample F01. LM magnification of 100x

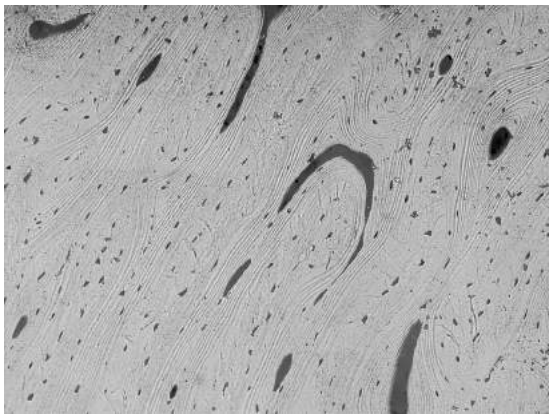

(a) Porosity of the axial-polished face image sample F01 part 13/21

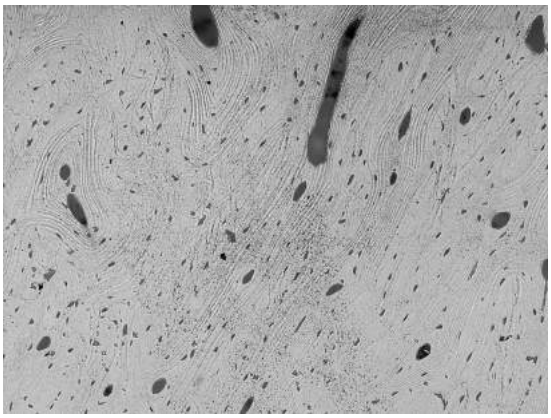

(b) Porosity of the axial-polished face image sample F01 part 14/21

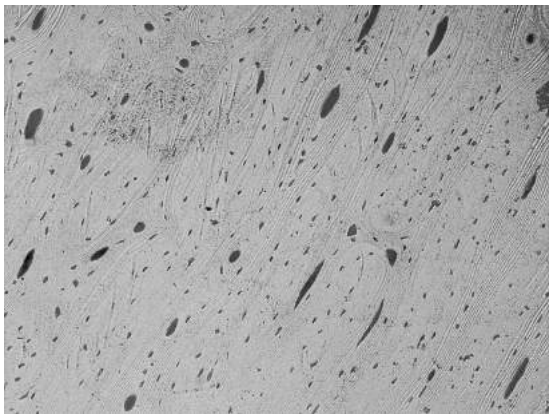

(c) Porosity of the axial-polished face image sample F01 part 15/21

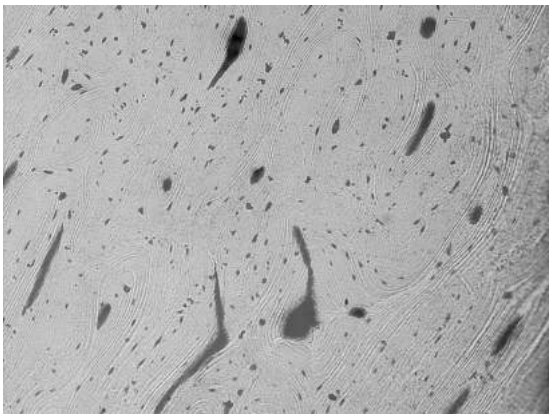

(d) Porosity of the axial-polished face image sample F01 part 16/21

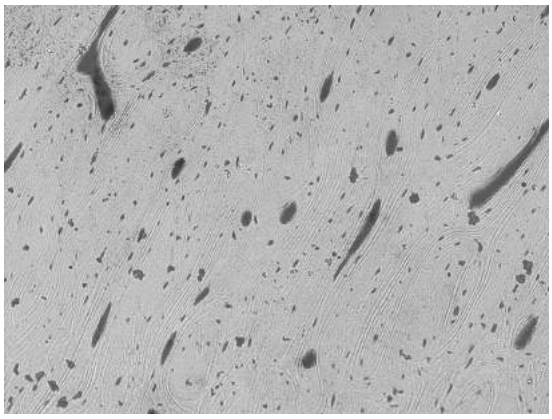

(e) Porosity of the axial-polished face image sample F01 part 17/21

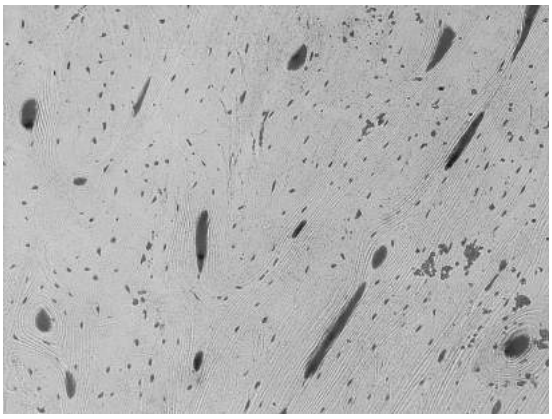

(f) Porosity of the axial-polished face image sample F01 part 18/21

Figure A.3: Porosity of axial-polished face from sample F01. LM magnification of 100x

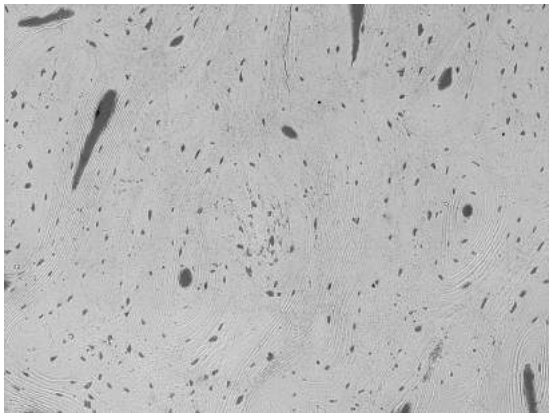

(a) Porosity of the axial-polished face image sample F01 part 19/21

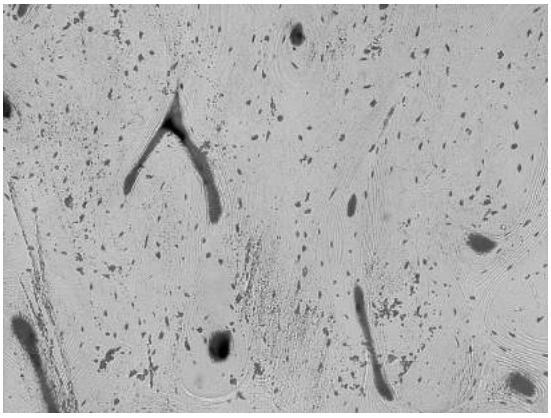

(b) Porosity of the axial-polished face image sample F01 part 20/21

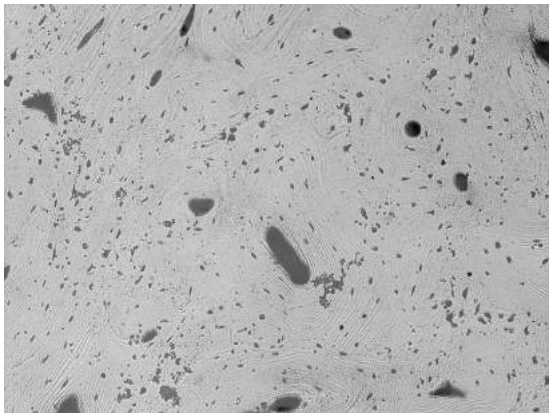

(c) Porosity of the axial-polished face image sample F01 part 21/21

Figure A.4: Porosity of axial-polished face from sample F01. LM magnification of 100x

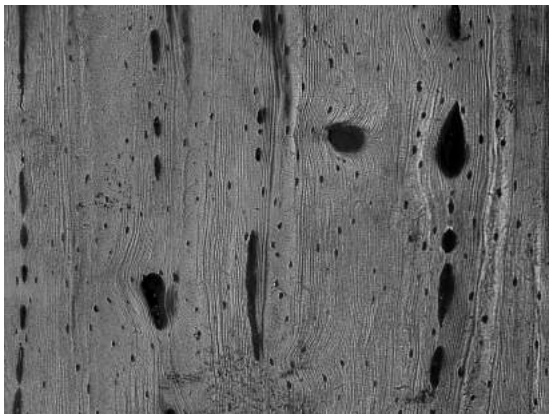

(a) Porosity of the axial-polished face image sample F02 part 1/10

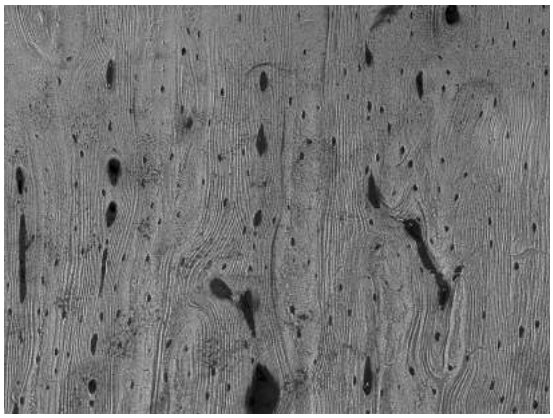

(b) Porosity of the axial-polished face image sample F02 part 2/10

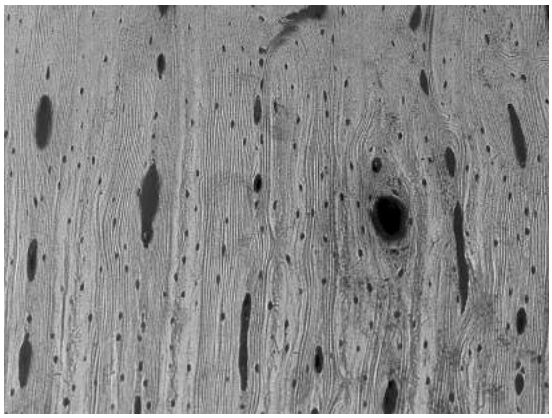

(c) Porosity of the axial-polished face image sample F02 part 3/10

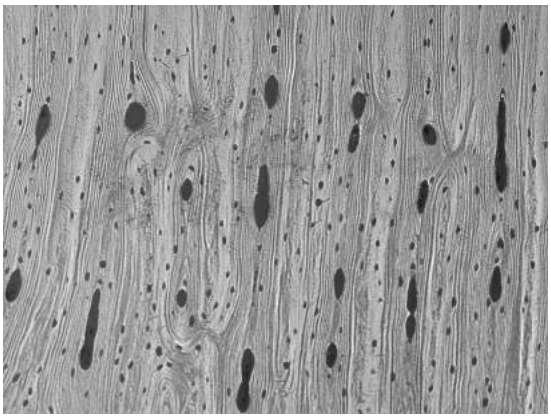

(d) Porosity of the axial-polished face image sample F02 part 4/10

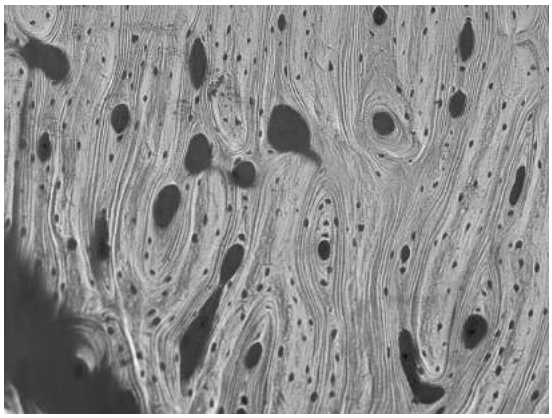

(e) Porosity of the axial-polished face image sample F02 part 5/10

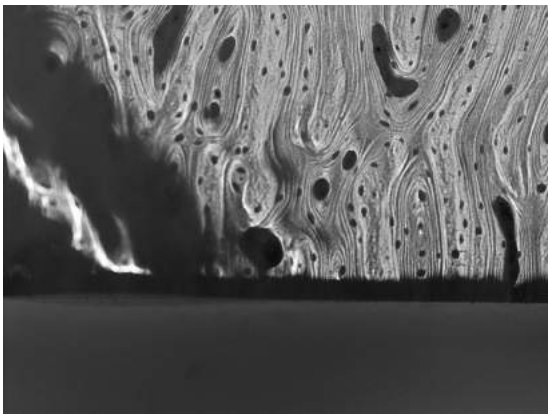

(f) Porosity of the axial-polished face image sample F02 part 6/10

Figure A.5: Porosity of axial-polished face from sample F02. LM magnification of 100x

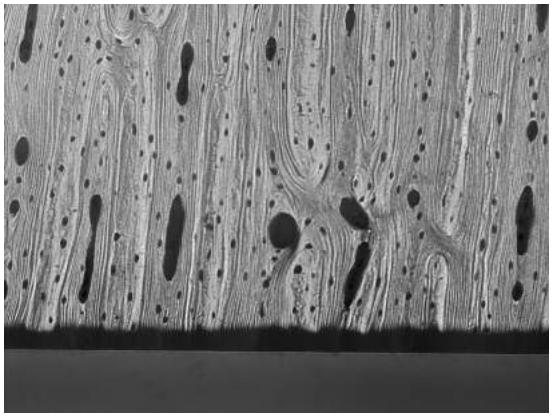

(a) Porosity of the axial-polished face image sample F02 part 7/10

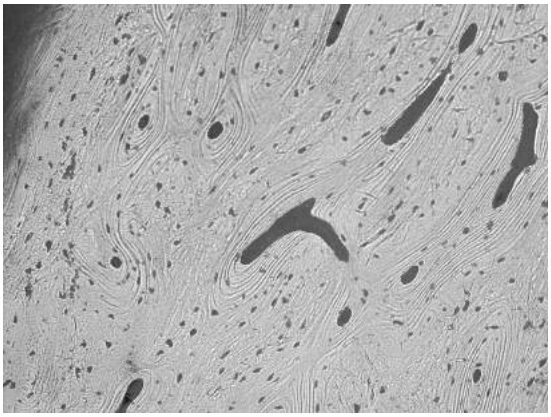

(b) Porosity of the axial-polished face image sample F01 part 8/10

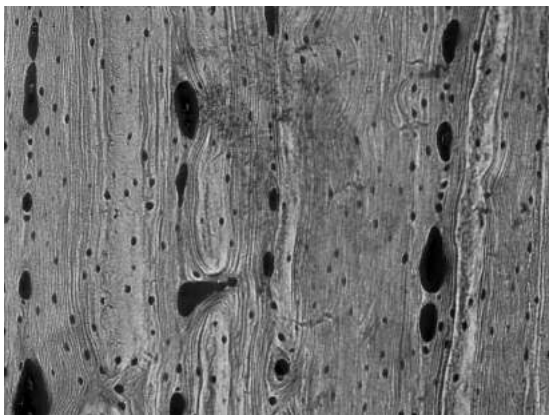

(c) Porosity of the axial-polished face image sample F02 part 9/10

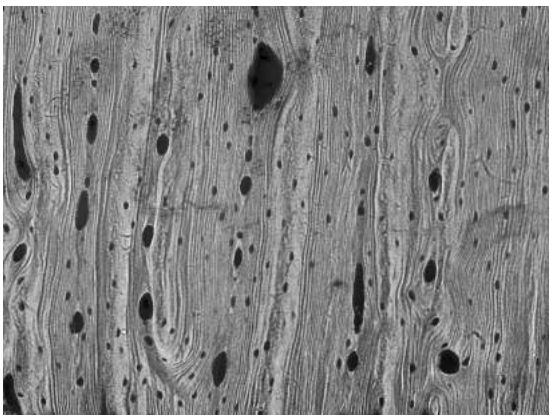

(d) Porosity of the axial-polished face image sample F02 part 10/10

Figure A.6: Porosity of axial-polished face from sample F02. LM magnification of 100x

(a) Porosity of the axial-polished face image sample F03 part 1/12

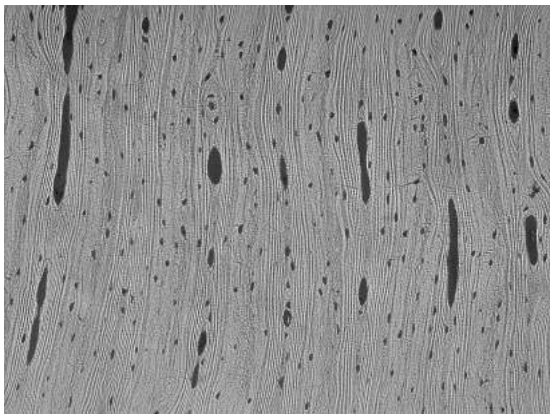

(b) Porosity of the axial-polished face image sample F03 part 2/12

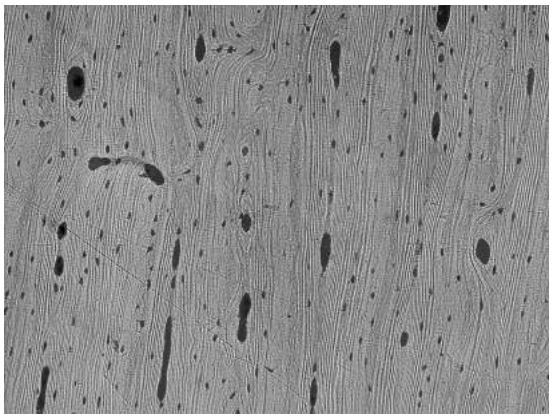

(c) Porosity of the axial-polished face image sample F03 part 3/12

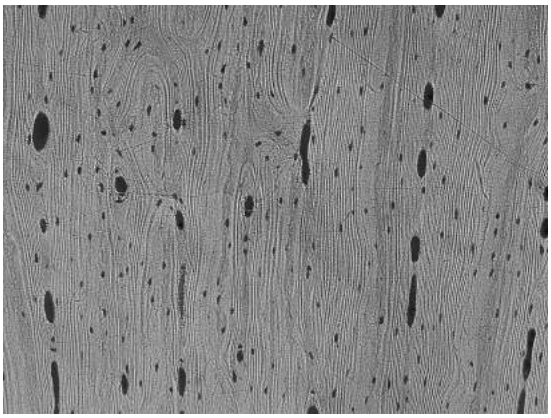

(d) Porosity of the axial-polished face image sample F03 part 4/12

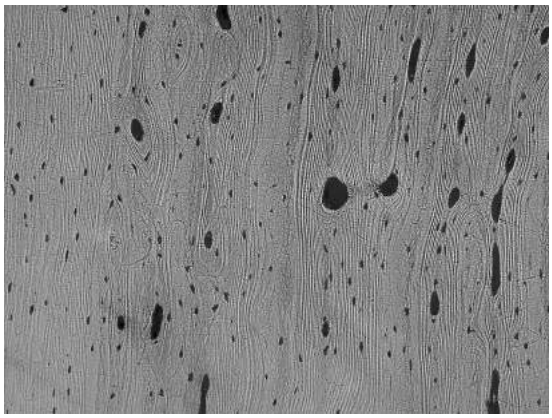

(e) Porosity of the axial-polished face image sample F03 part 5/12

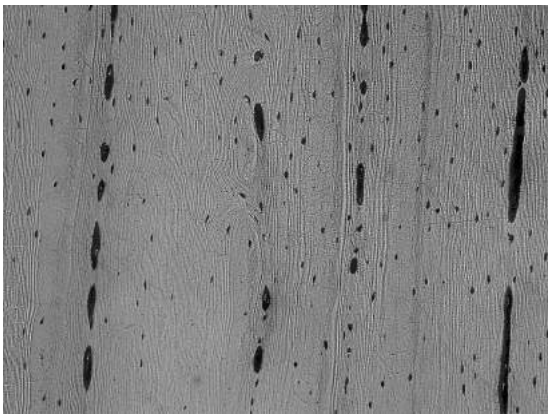

(f) Porosity of the axial-polished face image sample F03 part 6/12

Figure A.7: Porosity of axial-polished face from sample F03. LM magnification of 100x

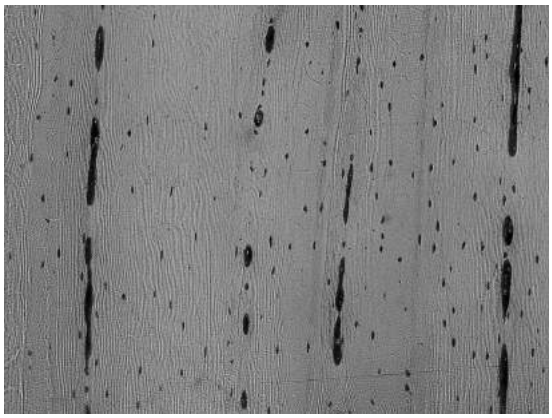

(a) Porosity of the axial-polished face image sample F03 part 7/12

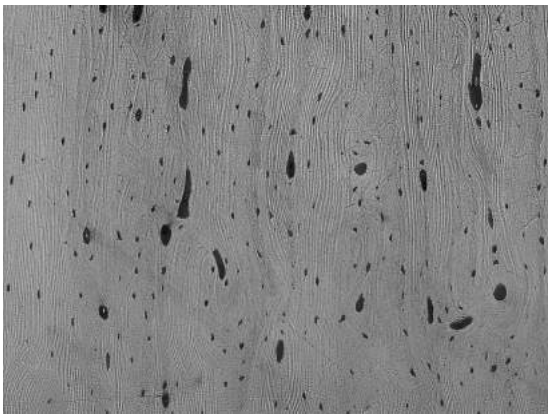

(b) Porosity of the axial-polished face image sample F03 part 8/12

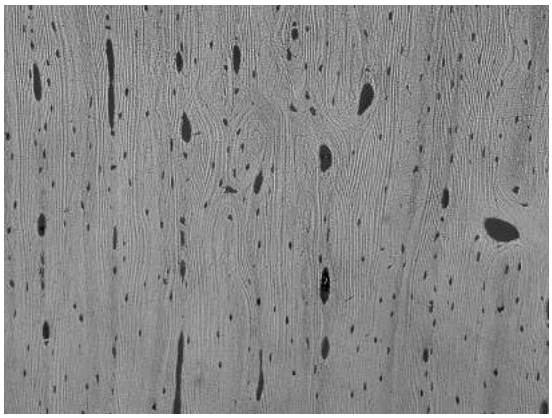

(c) Porosity of the axial-polished face image sample F03 part 9/12

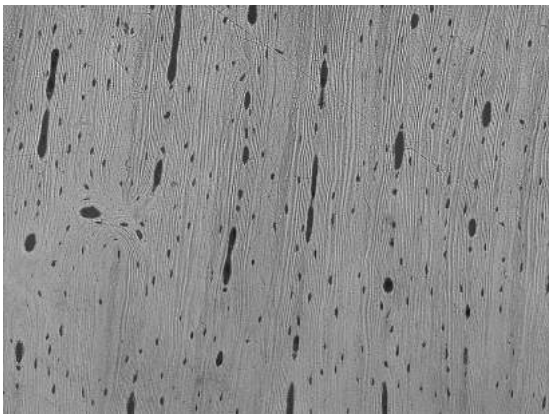

(d) Porosity of the axial-polished face image sample F03 part 10/12

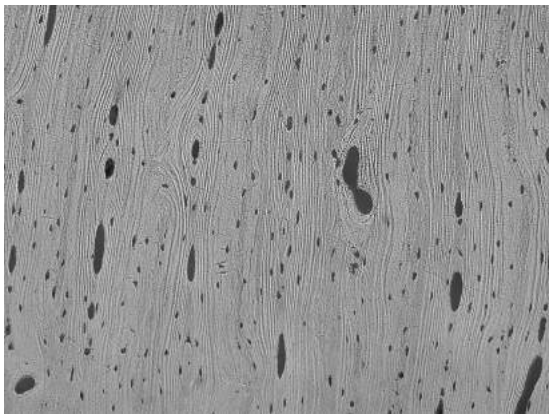

(e) Porosity of the axial-polished face image sample F03 part 11/12

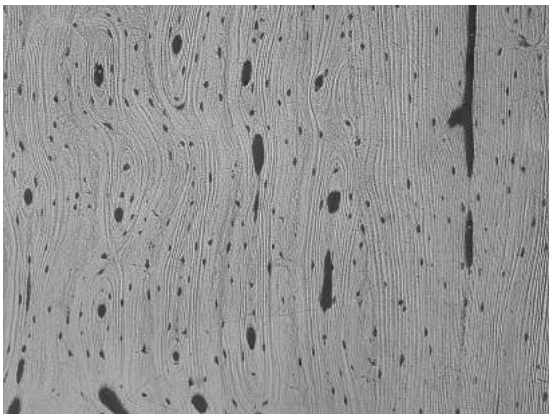

(f) Porosity of the axial-polished face image sample F03 part 12/12

Figure A.8: Porosity of axial-polished face from sample F03. LM magnification of 100x

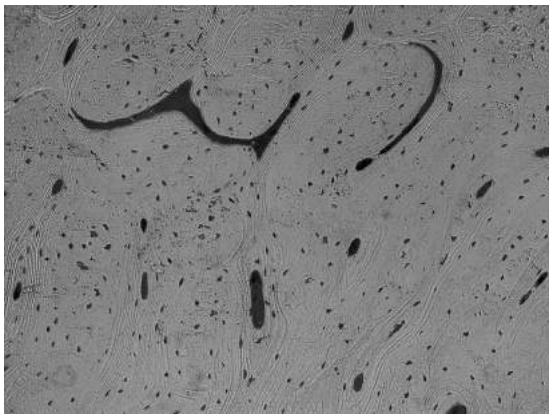

(a) Porosity of the axial-polished face image sample F04 part 1/12

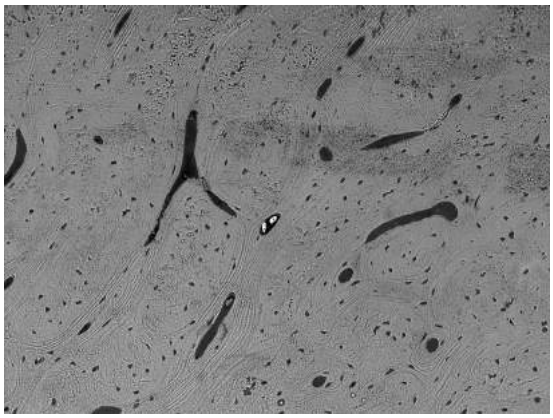

(b) Porosity of the axial-polished face image sample F04 part 2/12

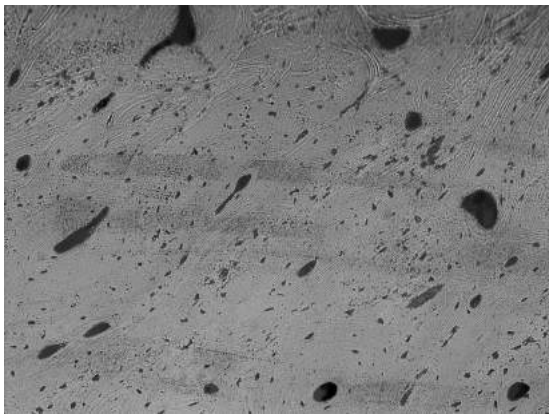

(c) Porosity of the axial-polished face image sample F04 part 3/12

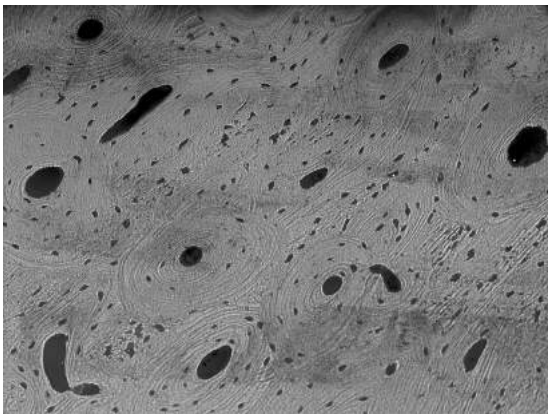

(d) Porosity of the axial-polished face image sample F04 part 4/12

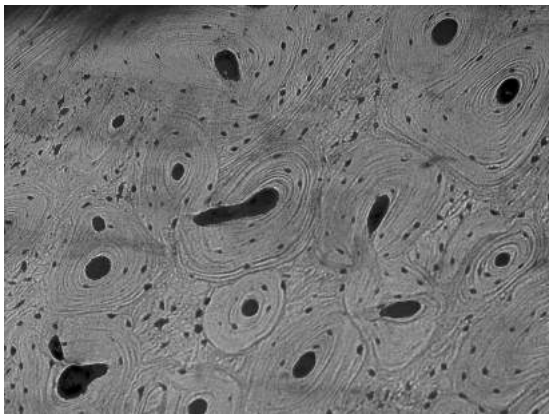

(e) Porosity of the axial-polished face image sample F04 part 5/12

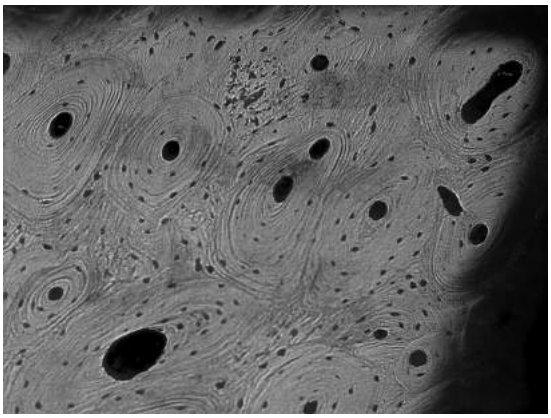

(f) Porosity of the axial-polished face image sample F04 part 6/12

Figure A.9: Porosity of axial-polished face from sample F04. LM magnification of 100x

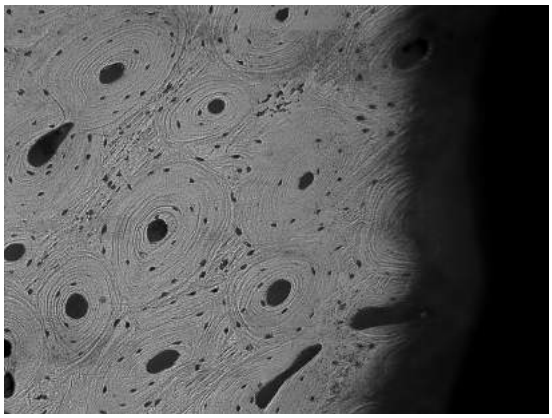

(a) Porosity of the axial-polished face image sample F04 part 7/12

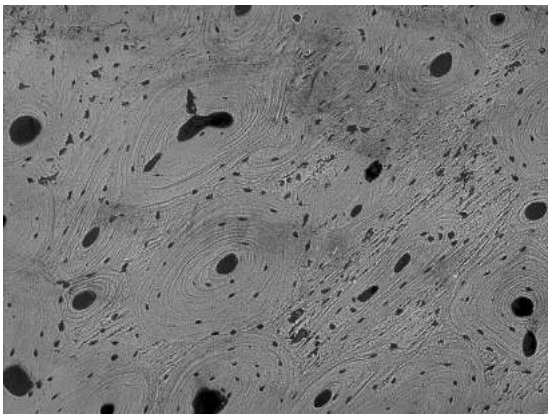

(b) Porosity of the axial-polished face image sample F04 part 8/12

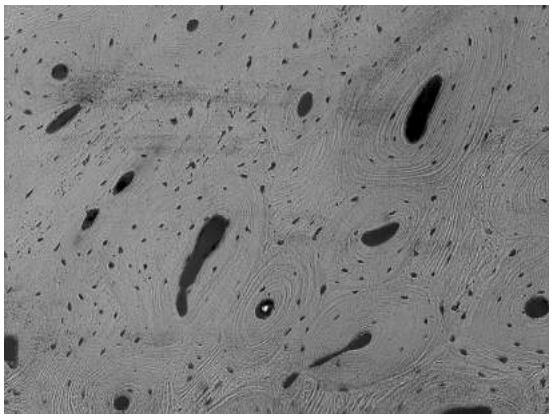

(c) Porosity of the axial-polished face image sample F04 part 9/12

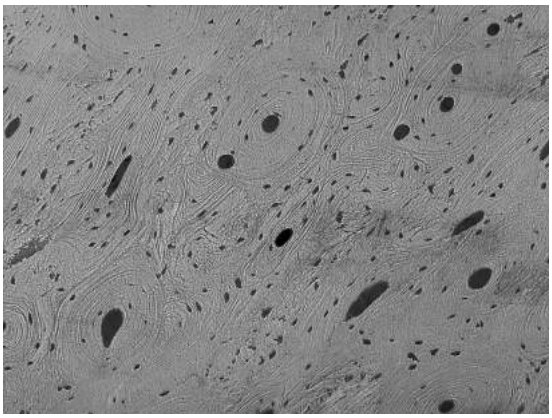

(d) Porosity of the axial-polished face image sample F04 part 10/12

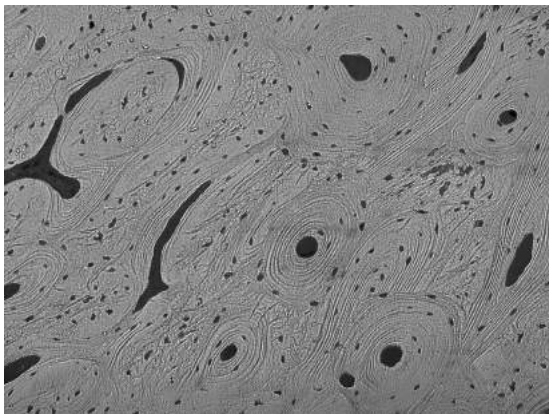

(e) Porosity of the axial-polished face image sample F04 part 11/12

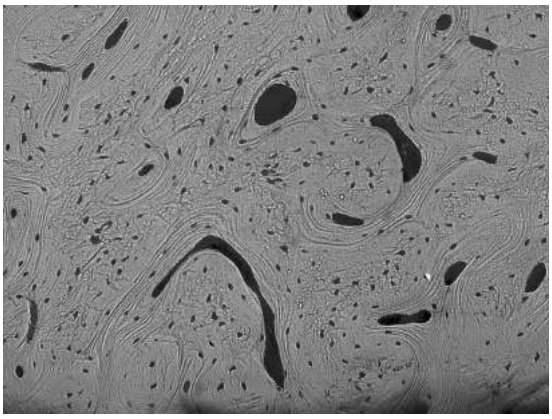

(f) Porosity of the axial-polished face image sample F04 part 12/12

Figure A.10: Porosity of axial-polished face from sample F04. LM magnification of 100x

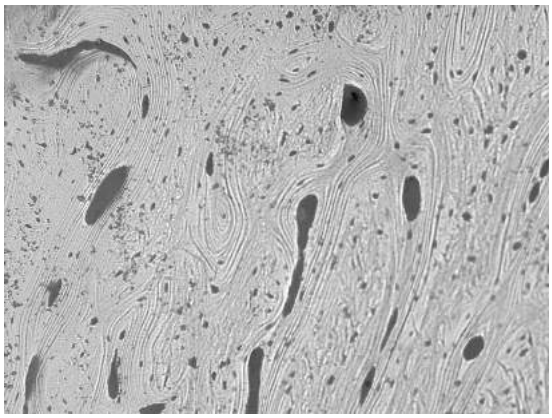

(a) Porosity of the axial-polished face image sample F05 part 1/11

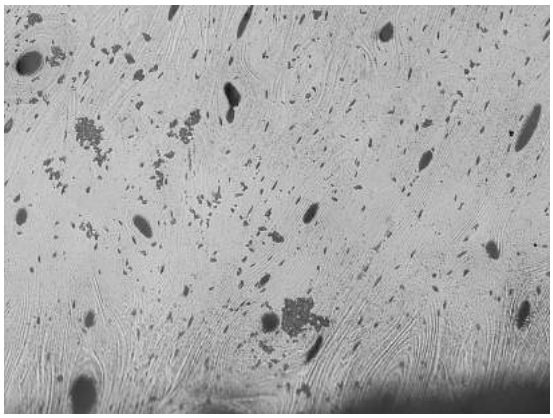

(b) Porosity of the axial-polished face image sample F05 part 2/11

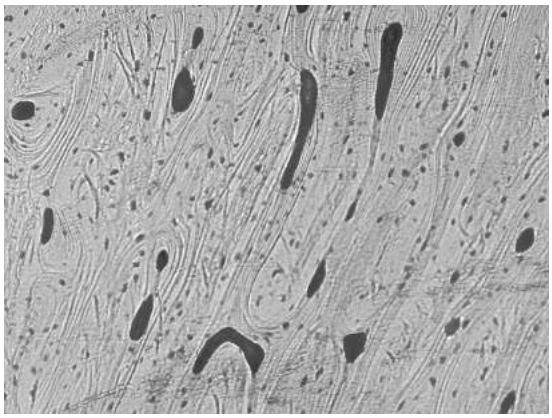

(c) Porosity of the axial-polished face image sample F05 part 3/11

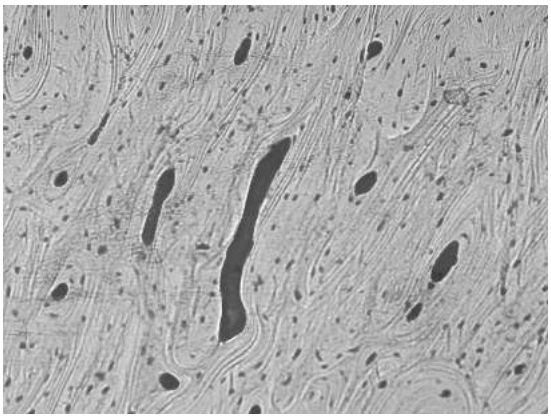

(d) Porosity of the axial-polished face image sample F05 part 4/11

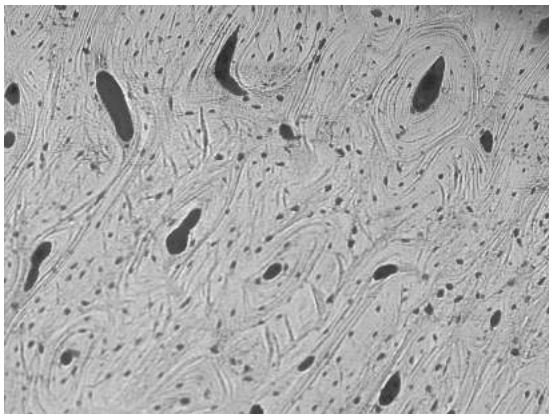

(e) Porosity of the axial-polished face image sample F05 part 5/11

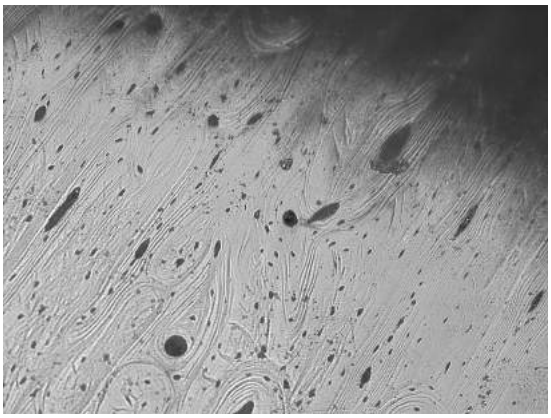

(f) Porosity of the axial-polished face image sample F05 part 6/11

Figure A.11: Porosity of axial-polished face from sample F05. LM magnification of 100x

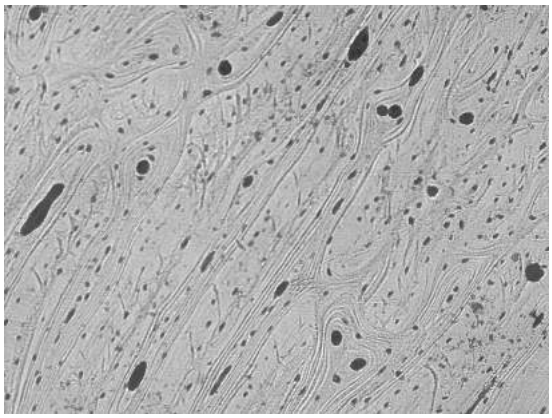

(a) Porosity of the axial-polished face image sample F05 part 7/11

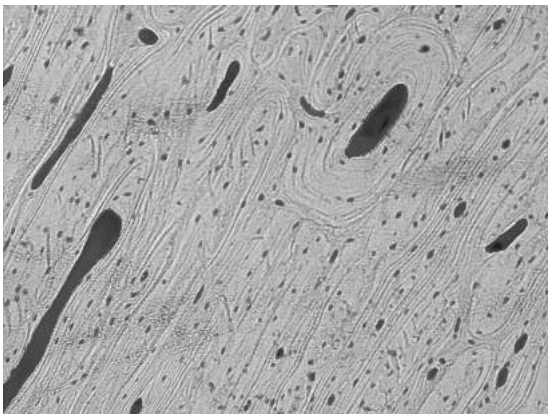

(b) Porosity of the axial-polished face image sample F05 part 8/11

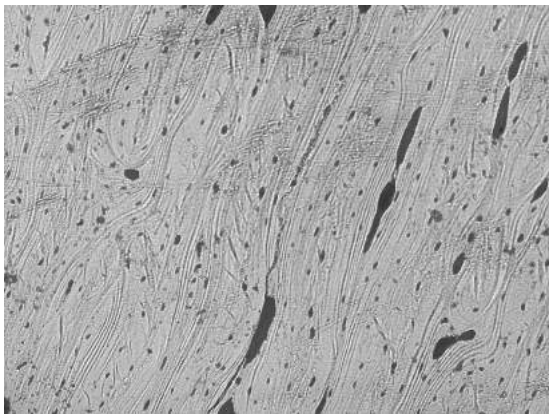

(c) Porosity of the axial-polished face image sample F05 part 9/11

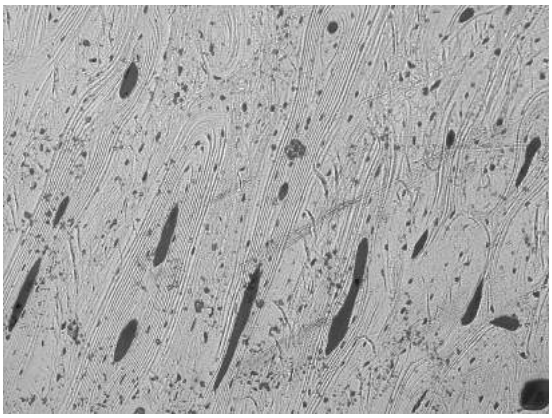

(d) Porosity of the axial-polished face image sample F05 part 10/11

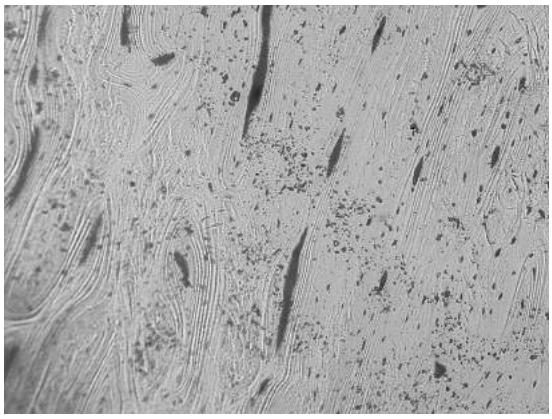

(e) Porosity of the axial-polished face image sample F05 part 11/11

Figure A.12: Porosity of axial-polished face from sample F05. LM magnification of 100x

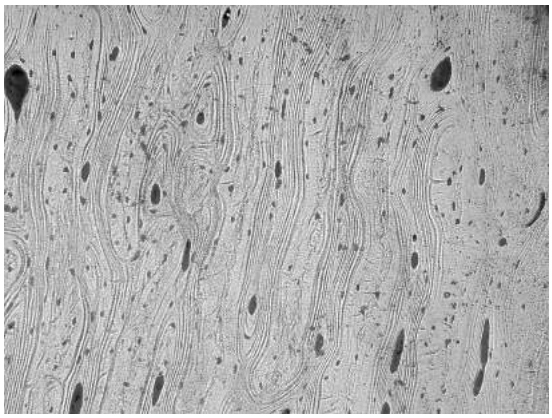

(a) Porosity of the axial-polished face image sample F06 part 1/10

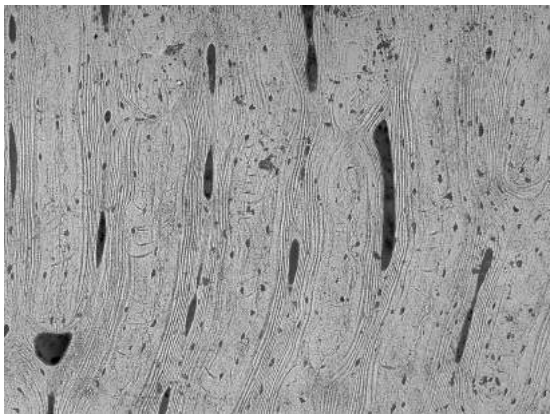

(b) Porosity of the axial-polished face image sample F02 part 2/10

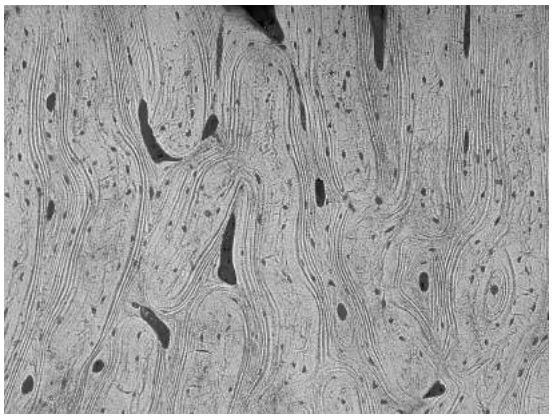

(c) Porosity of the axial-polished face image sample F06 part 3/10

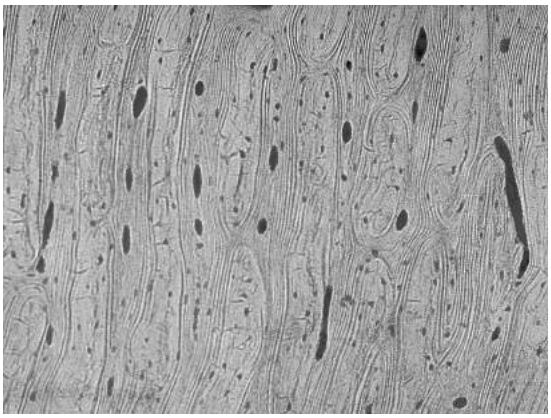

(d) Porosity of the axial-polished face image sample F06 part 4/10

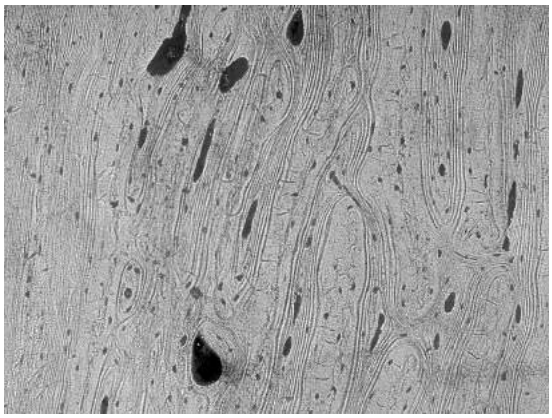

(e) Porosity of the axial-polished face image sample F06 part 5/10

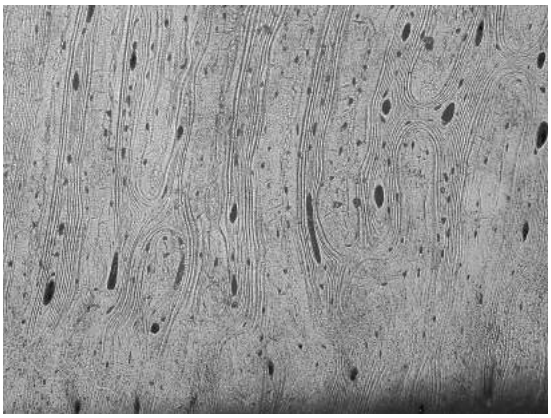

(f) Porosity of the axial-polished face image sample F06 part 6/10

Figure A.13: Porosity of axial-polished face from sample F06. LM magnification of 100x

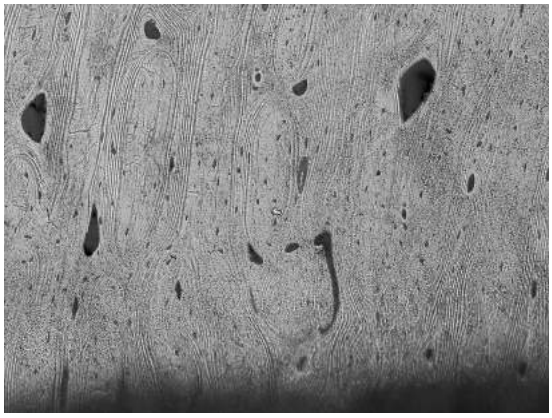

(a) Porosity of the axial-polished face image sample F06 part 7/10

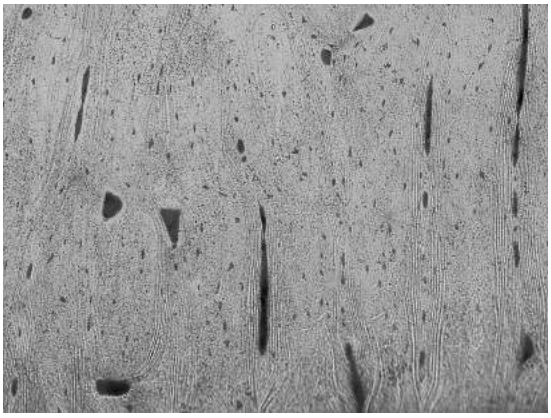

(b) Porosity of the axial-polished face image sample F06 part 8/10

(c) Porosity of the axial-polished face image sample F06 part 9/10

(d) Porosity of the axial-polished face image sample F06 part 10/10

Figure A.14: Porosity of axial-polished face from sample F06. LM magnification of 100x

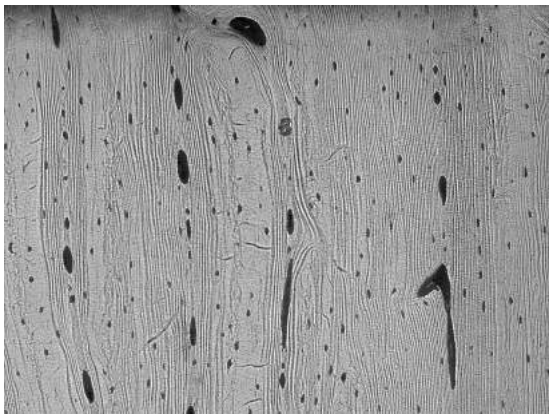

(a) Porosity of the axial-polished face image sample F07 part 1/12

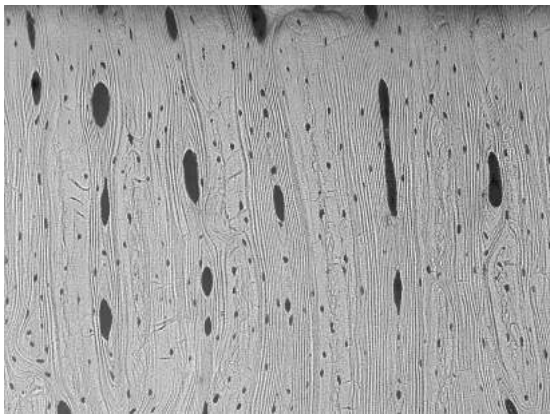

(b) Porosity of the axial-polished face image sample F07 part 2/12

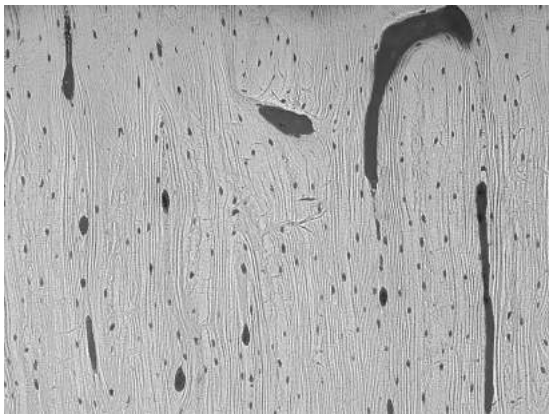

(c) Porosity of the axial-polished face image sample F07 part 3/12

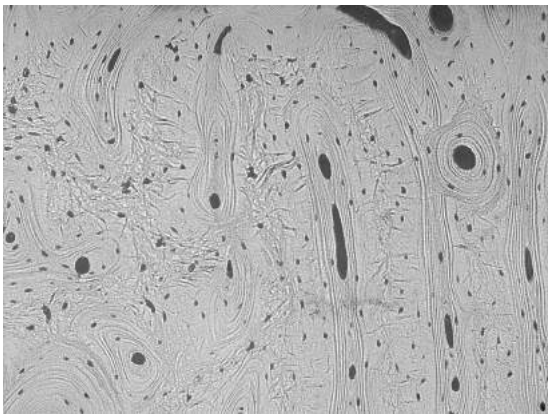

(d) Porosity of the axial-polished face image sample F07 part 4/12

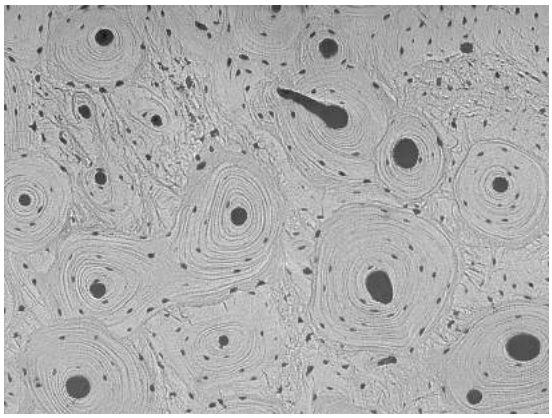

(e) Porosity of the axial-polished face image sample F07part 5/12

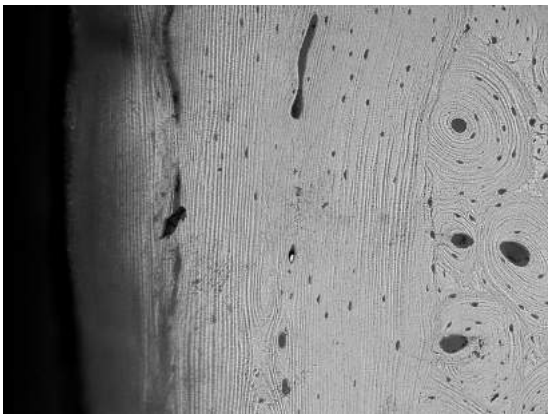

(f) Porosity of the axial-polished face image sample F04 part 6/12

Figure A.15: Porosity of axial-polished face from sample F07. LM magnification of 100x

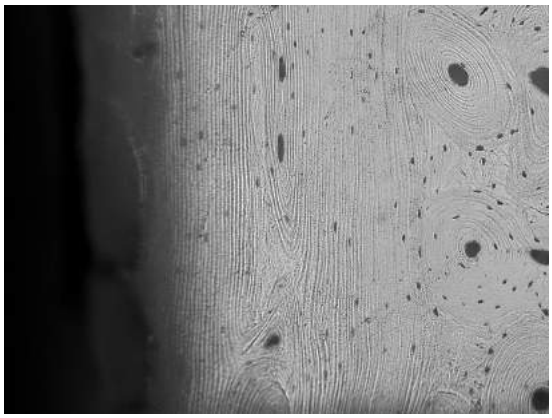

(a) Porosity of the axial-polished face image sample F07 part 7/12

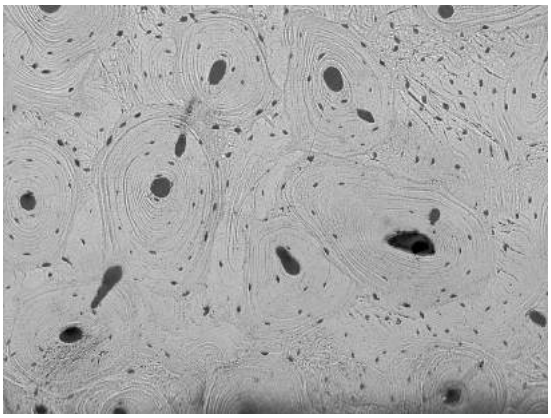

(b) Porosity of the axial-polished face image sample F07 part 8/12

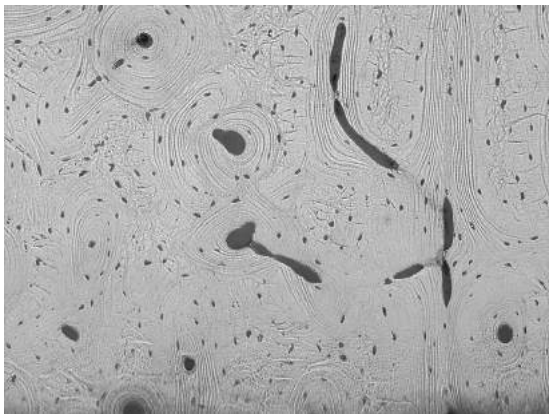

(c) Porosity of the axial-polished face image sample F07 part 9/12

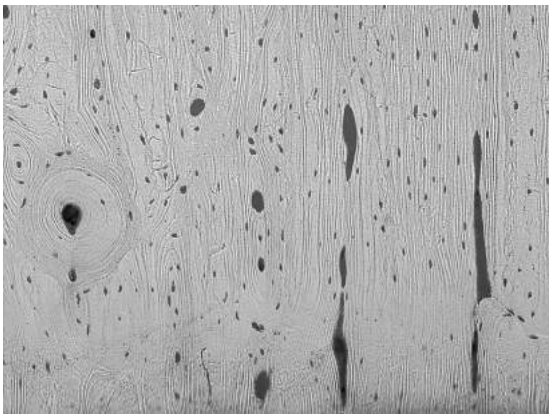

(d) Porosity of the axial-polished face image sample F07 part 10/12

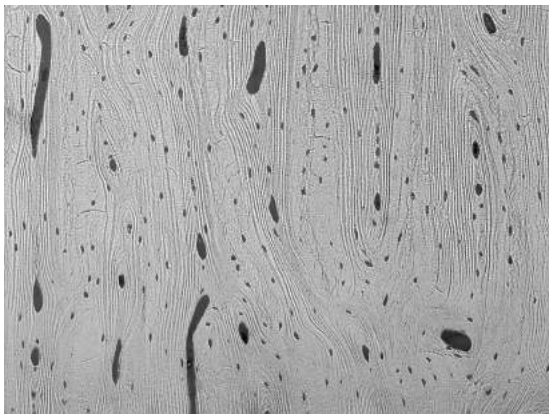

(e) Porosity of the axial-polished face image sample F07 part 11/12

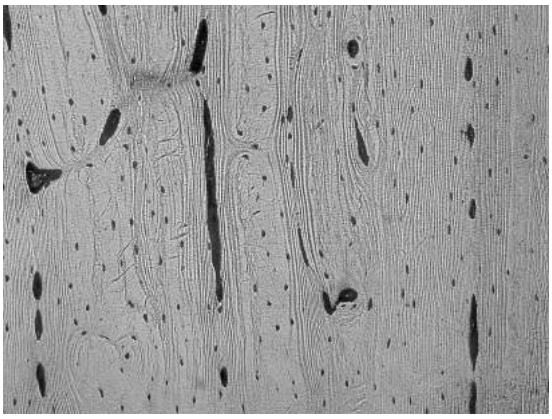

(f) Porosity of the axial-polished face image sample F07 part 12/12

Figure A.16: Porosity of axial-polished face from sample F07. LM magnification of 100x

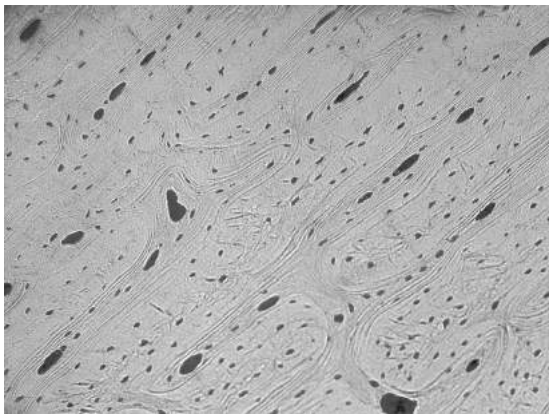

(a) Porosity of the axial-polished face image sample F08 part 1/12

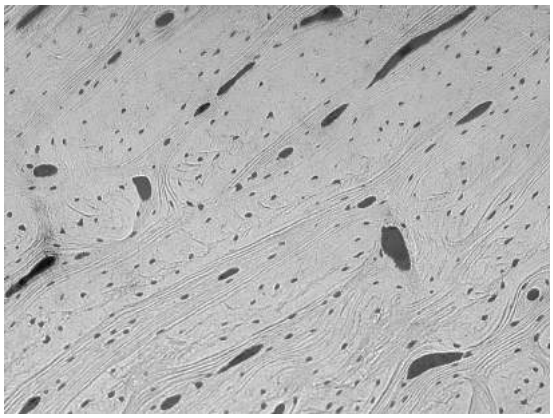

(b) Porosity of the axial-polished face image sample F08 part 2/12

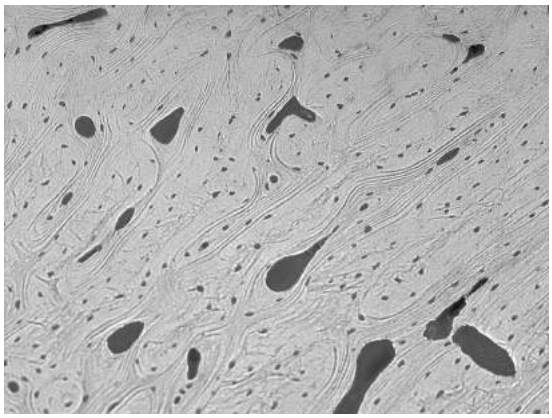

(c) Porosity of the axial-polished face image sample F08 part 3/12

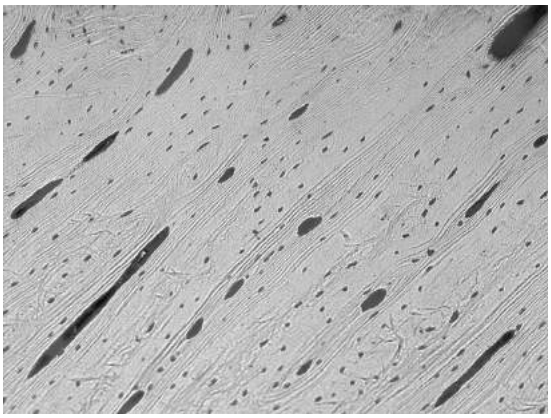

(d) Porosity of the axial-polished face image sample F08 part 4/12

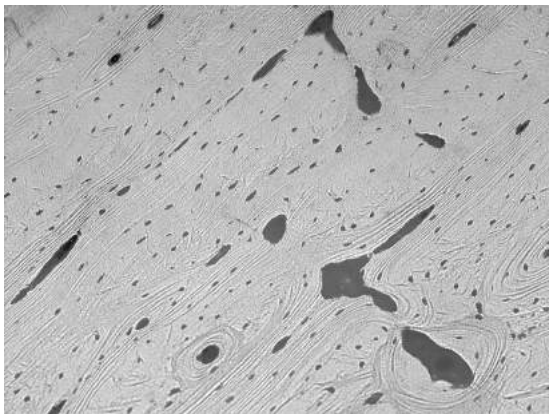

(e) Porosity of the axial-polished face image sample F08 part 5/12

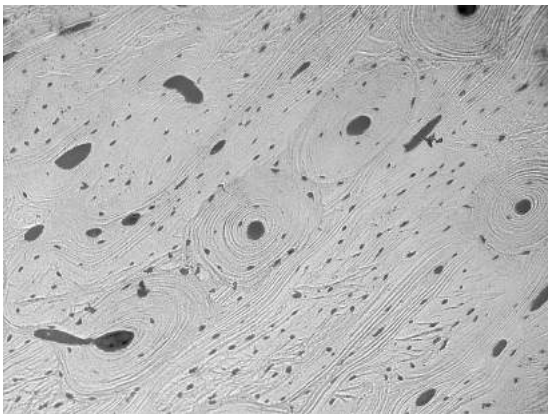

(f) Porosity of the axial-polished face image sample F08 part 6/12

Figure A.17: Porosity of axial-polished face from sample F08. LM magnification of 100x

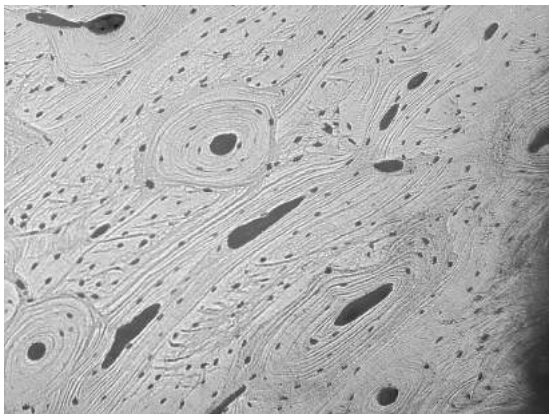

(a) Porosity of the axial-polished face image sample F08 part 7/12

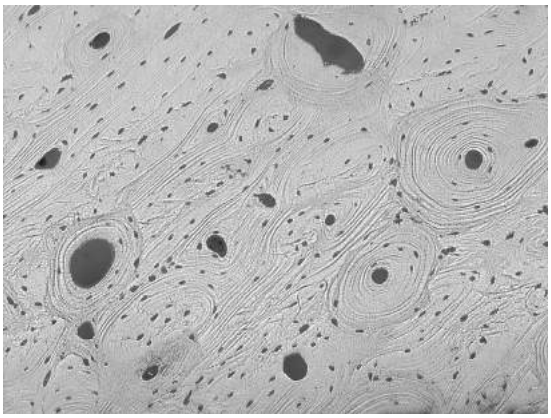

(b) Porosity of the axial-polished face image sample F08 part 8/12

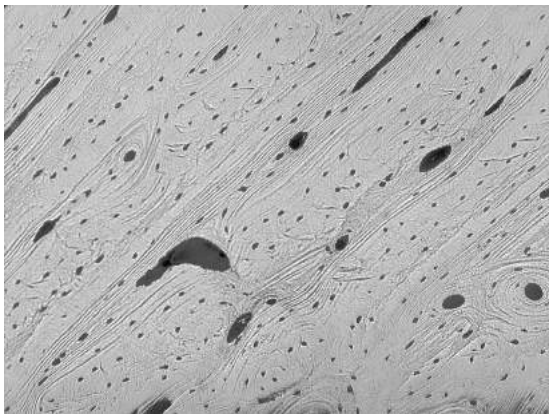

(c) Porosity of the axial-polished face image sample F08 part 9/12

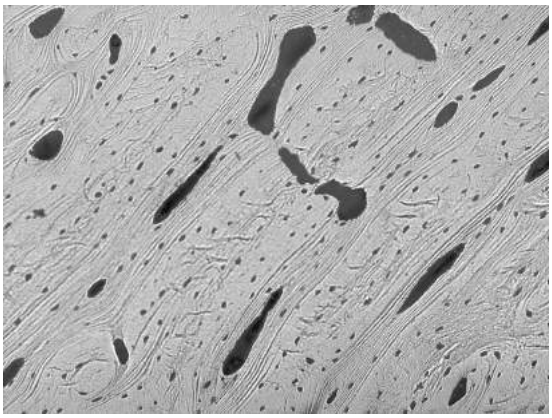

(d) Porosity of the axial-polished face image sample F08 part 10/12

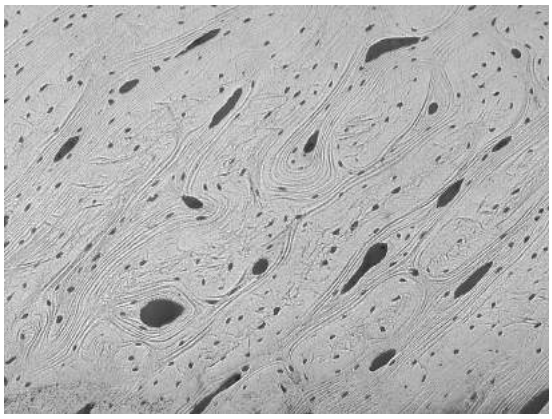

(e) Porosity of the axial-polished face image sample F08 part 11/12

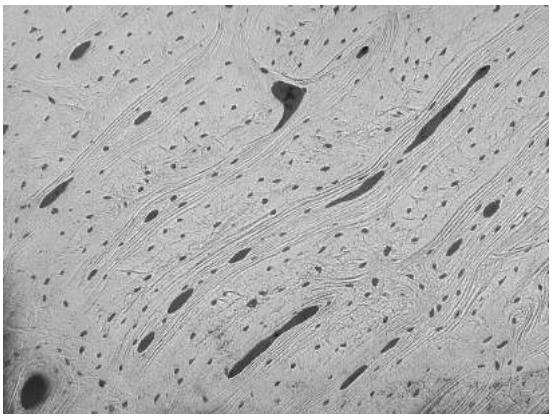

(f) Porosity of the axial-polished face image sample F08 part 12/12

Figure A.18: Porosity of axial-polished face from sample F08. LM magnification of 100x

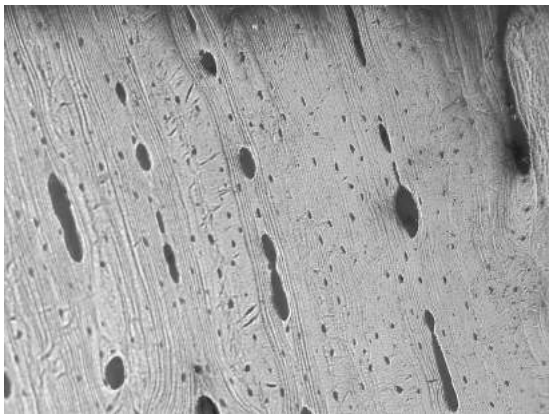

(a) Porosity of the axial-polished face image sample F09 part 1/12

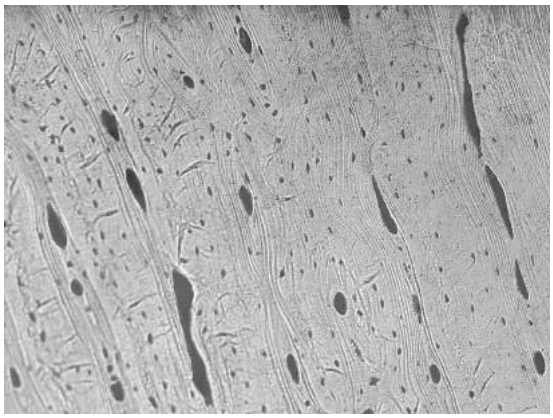

(b) Porosity of the axial-polished face image sample F09 part 2/12

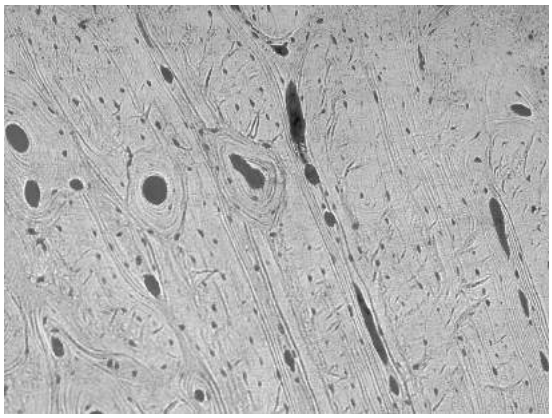

(c) Porosity of the axial-polished face image sample F09 part 3/12

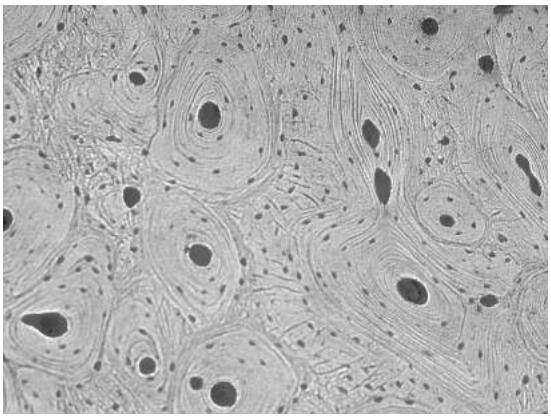

(d) Porosity of the axial-polished face image sample F09 part 4/12

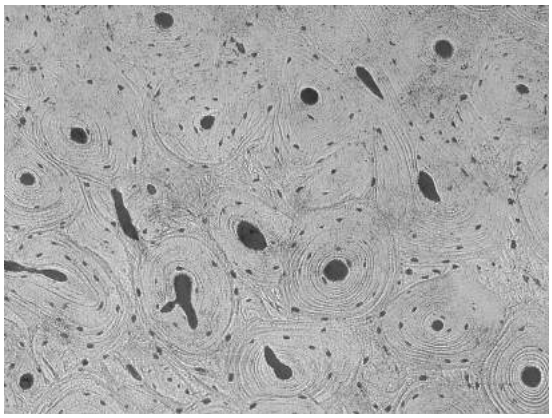

(e) Porosity of the axial-polished face image sample F09 part 5/12

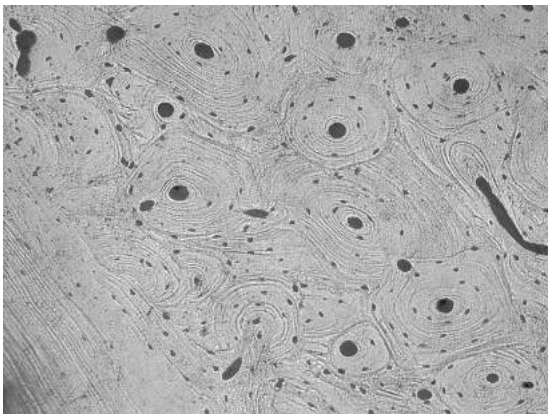

(f) Porosity of the axial-polished face image sample F09 part 6/12

Figure A.19: Porosity of axial-polished face from sample F09. LM magnification of 100x

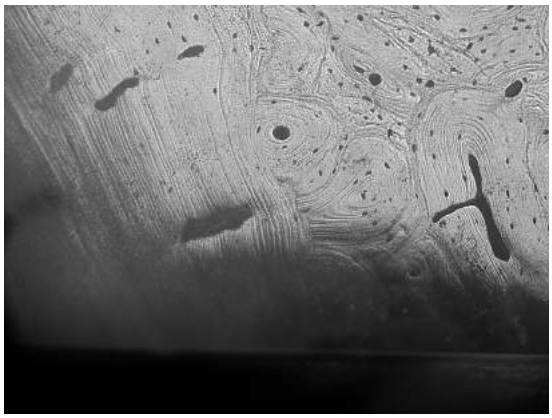

(a) Porosity of the axial-polished face image sample F09 part 7/12

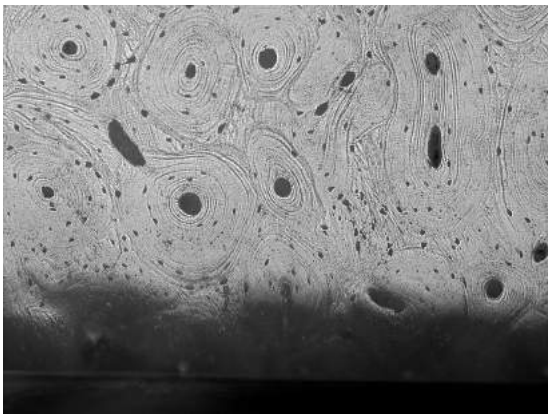

(b) Porosity of the axial-polished face image sample F09 part 8/12

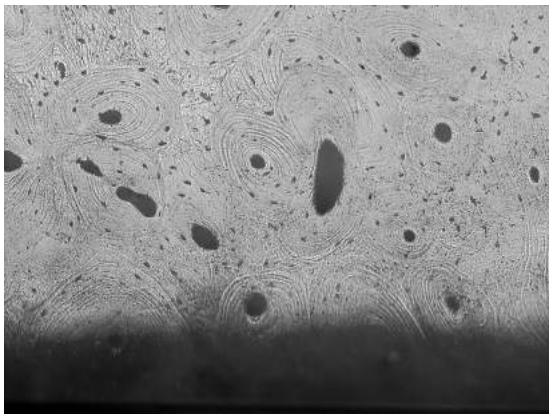

(c) Porosity of the axial-polished face image sample F08 part 9/12

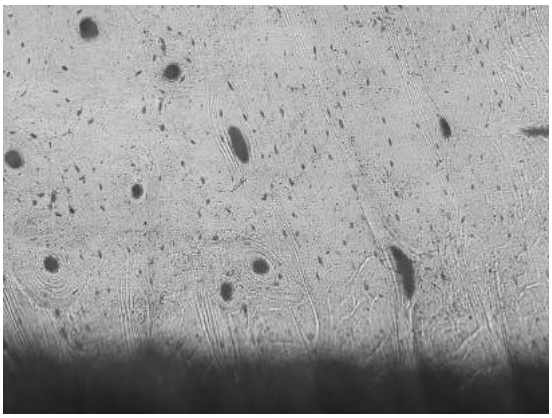

(d) Porosity of the axial-polished face image sample F09 part 10/12

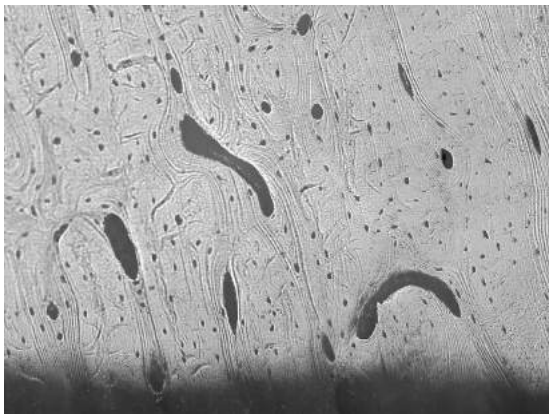

(e) Porosity of the axial-polished face image sample F09 part 11/12

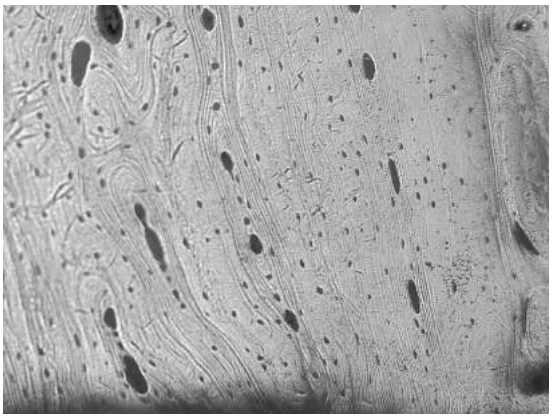

(f) Porosity of the axial-polished face image sample F09 part 12/12

Figure A.20: Porosity of axial-polished face from sample F09. LM magnification of 100x

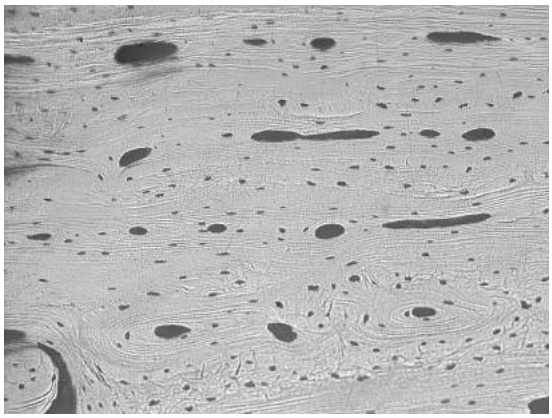

(a) Porosity of the axial-polished face image sample F10 part 1/10

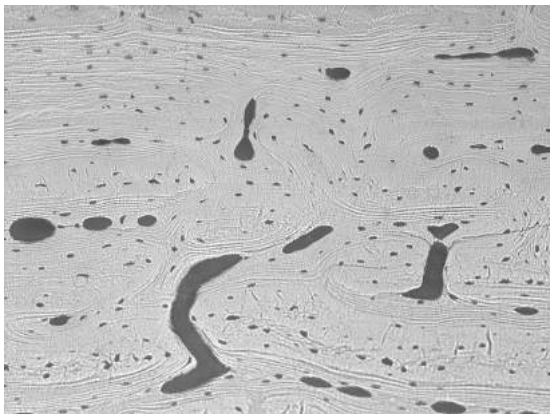

(b) Porosity of the axial-polished face image sample F10 part 2/10

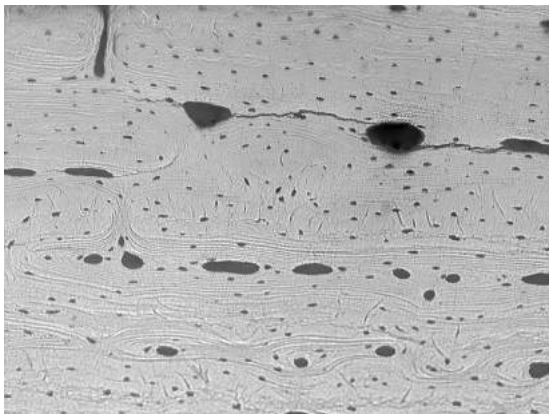

(c) Porosity of the axial-polished face image sample F10 part 3/10

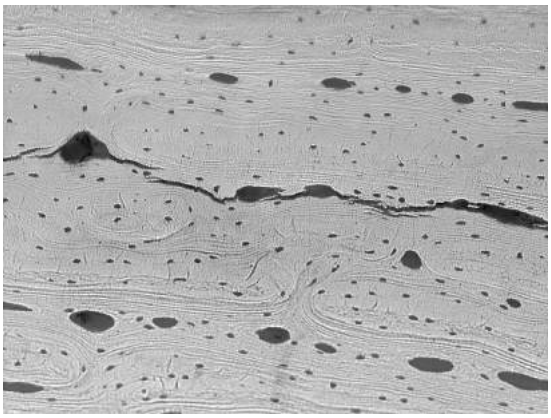

(d) Porosity of the axial-polished face image sample F10 part 4/10

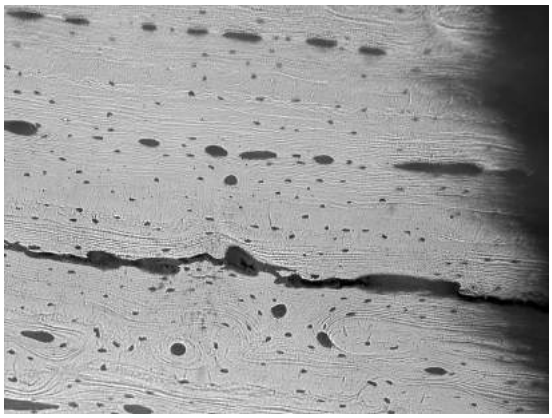

(e) Porosity of the axial-polished face image sample F10 part 5/10

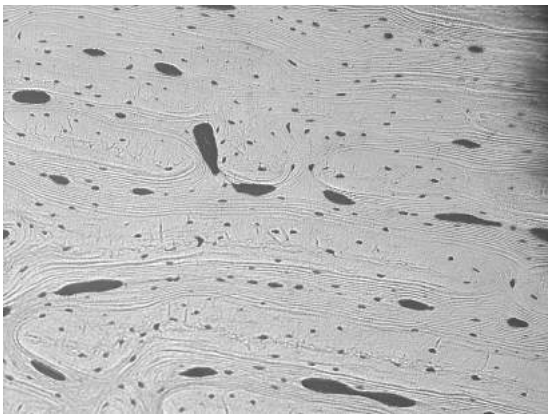

(f) Porosity of the axial-polished face image sample F10 part 6/10

Figure A.21: Porosity of axial-polished face from sample F10. LM magnification of 100x

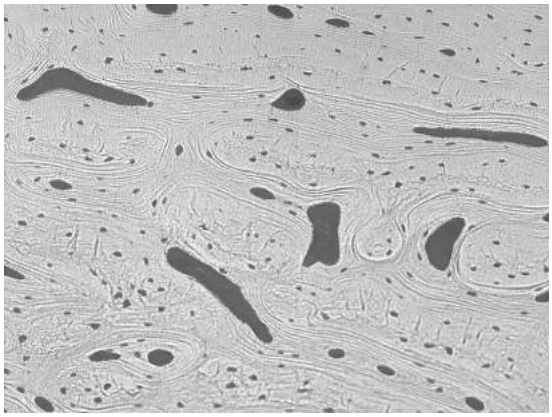

(a) Porosity of the axial-polished face image sample F10 part 7/10

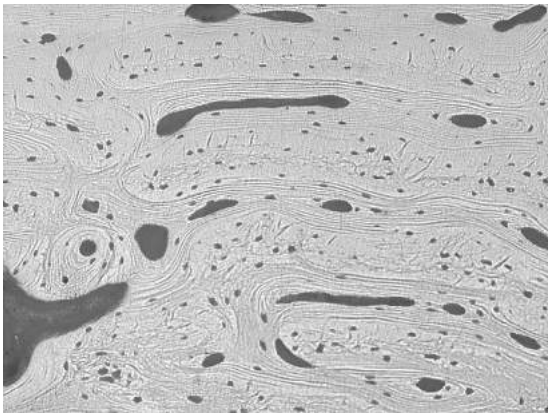

(b) Porosity of the axial-polished face image sample F10 part 8/10

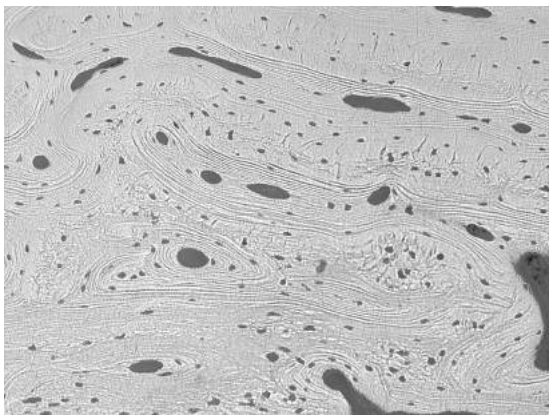

(c) Porosity of the axial-polished face image sample F10 part 9/10

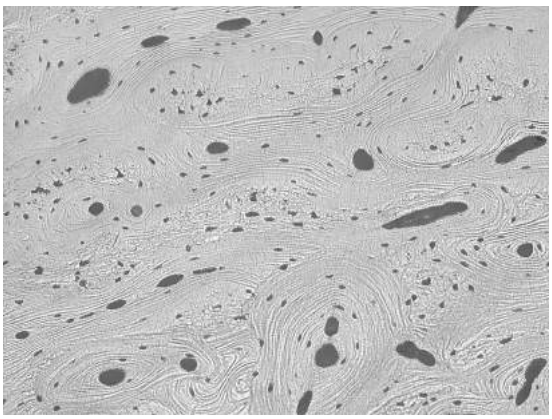

(d) Porosity of the axial-polished face image sample F10 part 10/10

Figure A.22: Porosity of axial-polished face from sample F10. LM magnification of 100x

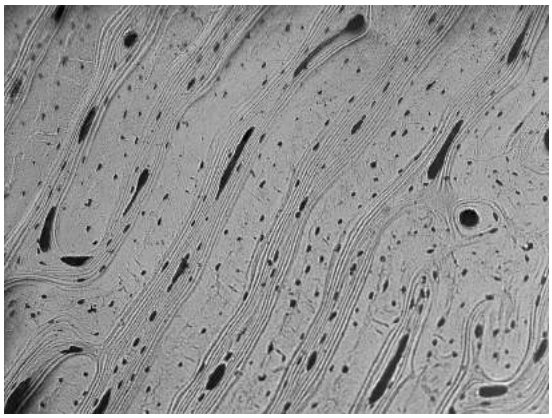

(a) Porosity of the axial-polished face image sample F11 part 1/10

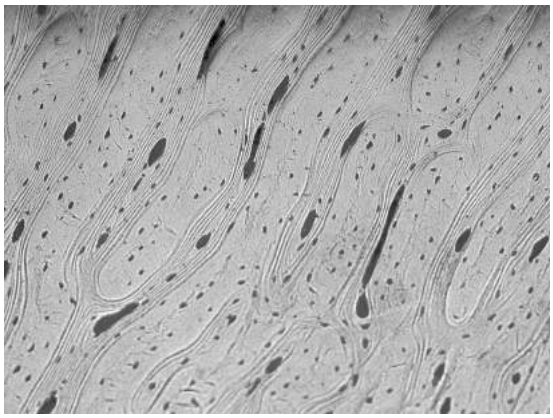

(b) Porosity of the axial-polished face image sample F11 part 2/10

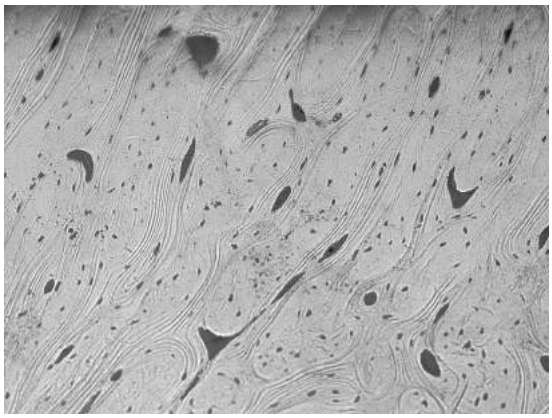

(c) Porosity of the axial-polished face image sample F11 part 3/10

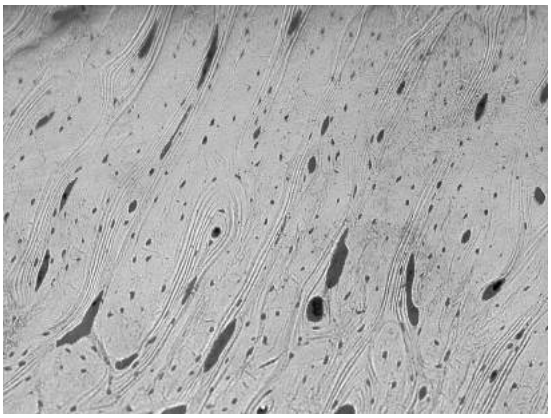

(d) Porosity of the axial-polished face image sample F11 part 4/10

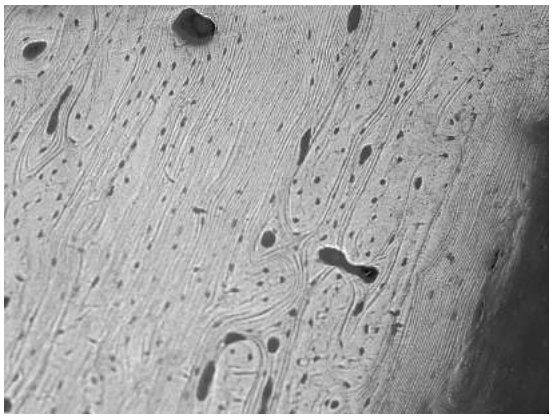

(e) Porosity of the axial-polished face image sample F11 part 5/10

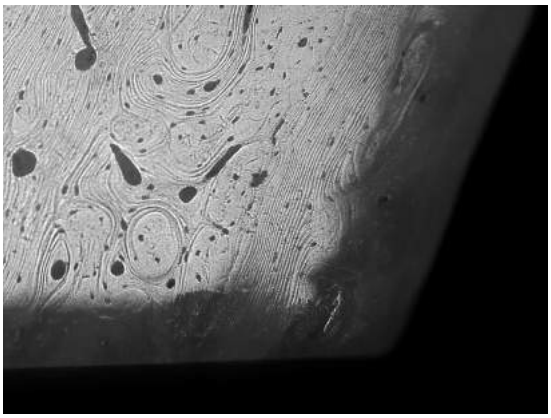

(f) Porosity of the axial-polished face image sample F11 part 6/10

Figure A.23: Porosity of axial-polished face from sample F11. LM magnification of 100x

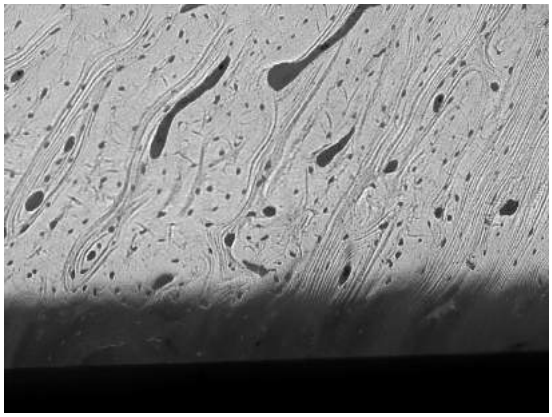

(a) Porosity of the axial-polished face image sample F11 part 7/10

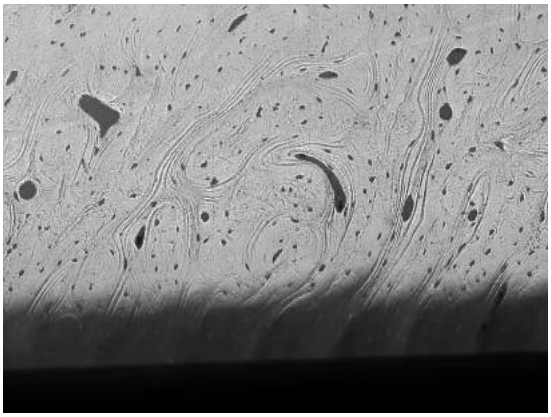

(b) Porosity of the axial-polished face image sample F11 part 8/10

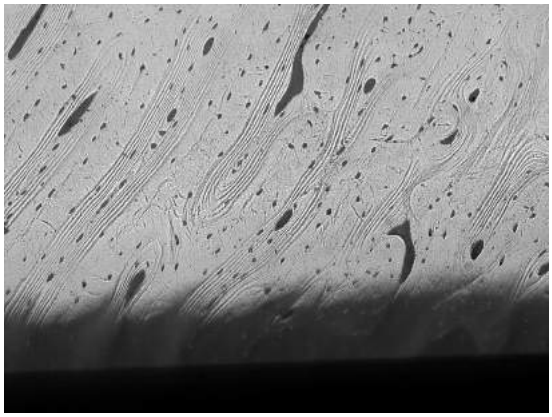

(c) Porosity of the axial-polished face image sample F11 part 9/10

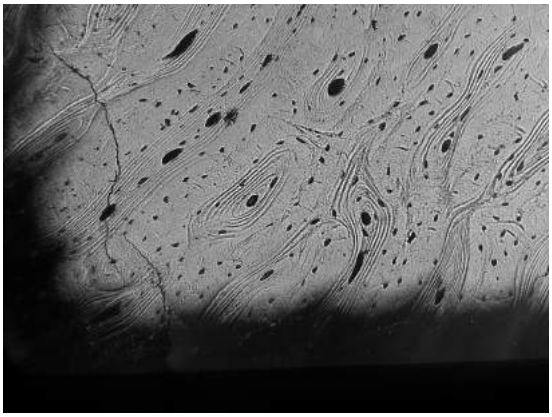

(d) Porosity of the axial-polished face image sample F11 part 10/10

Figure A.24: Porosity of axial-polished face from sample F11. LM magnification of 100x

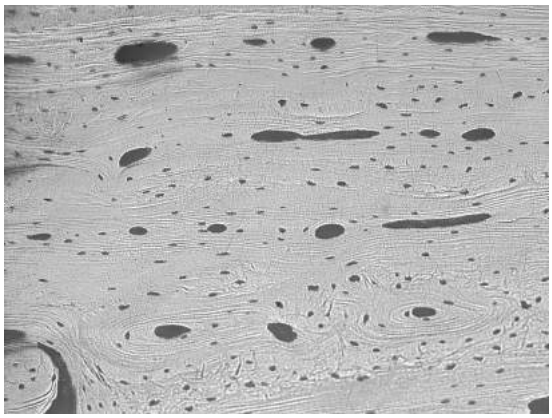

(a) Porosity of the axial-polished face image sample F10 part 1/12

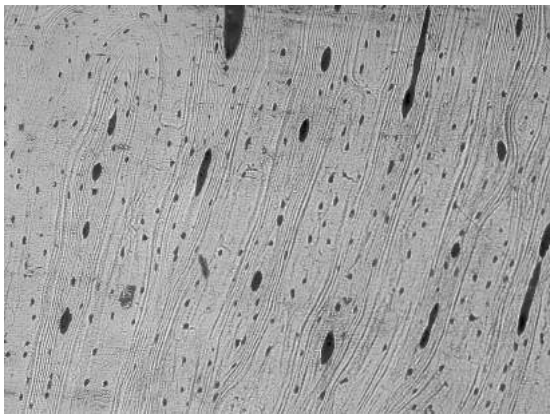

(b) Porosity of the axial-polished face image sample F12 part 2/12

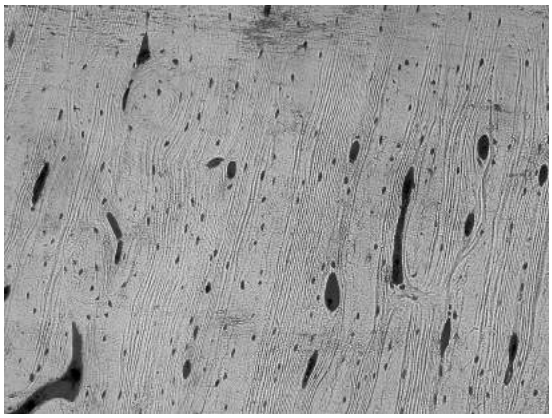

(c) Porosity of the axial-polished face image sample F12 part 3/12

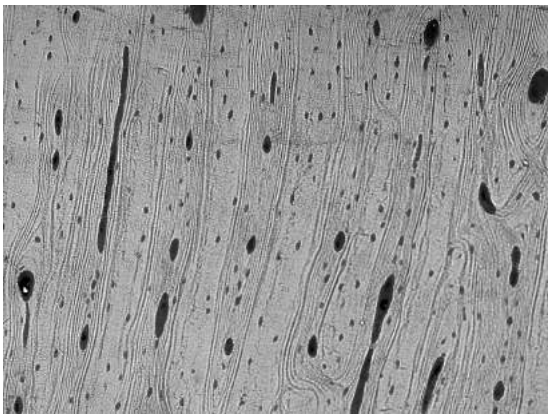

(d) Porosity of the axial-polished face image sample F12 part 4/12

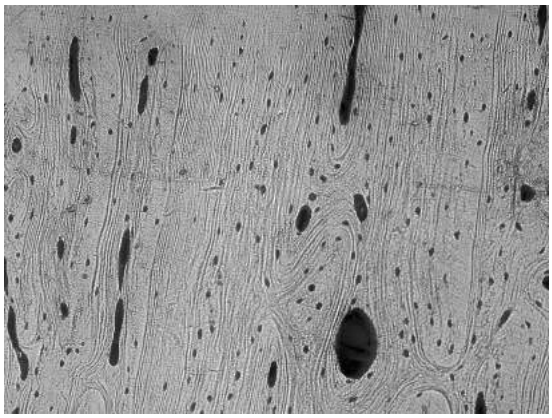

(e) Porosity of the axial-polished face image sample F12 part 5/12

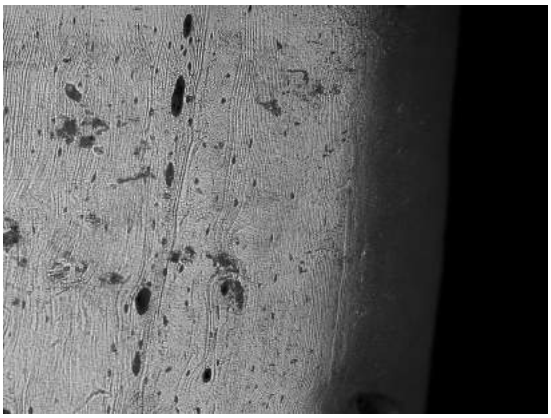

(f) Porosity of the axial-polished face image sample F12 part 6/12

Figure A.25: Porosity of axial-polished face from sample F12. LM magnification of 100x

(a) Porosity of the axial-polished face image sample F12 part 7/12

(b) Porosity of the axial-polished face image sample F12 part 8/12

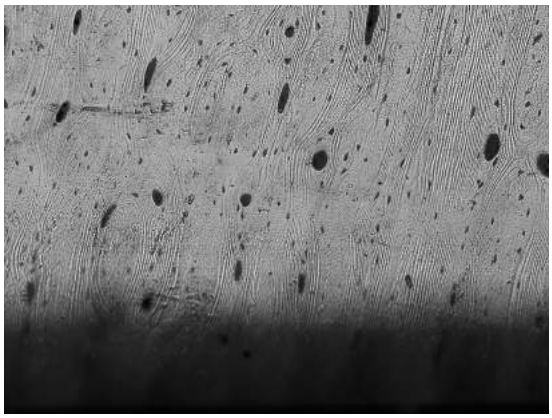

(c) Porosity of the axial-polished face image sample F12 part 9/12

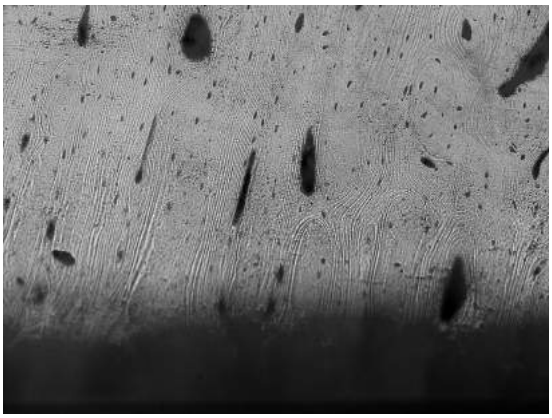

(d) Porosity of the axial-polished face image sample F12 part 10/12

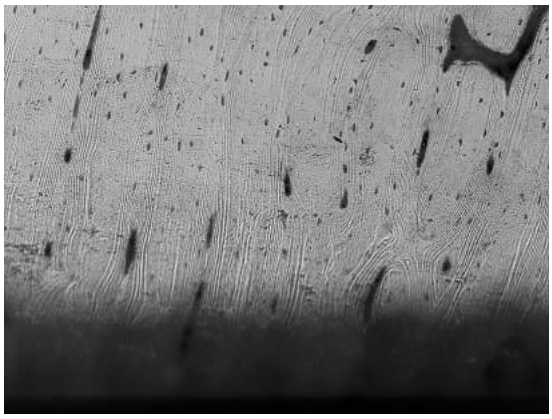

(e) Porosity of the axial-polished face image sample F12 part 11/12

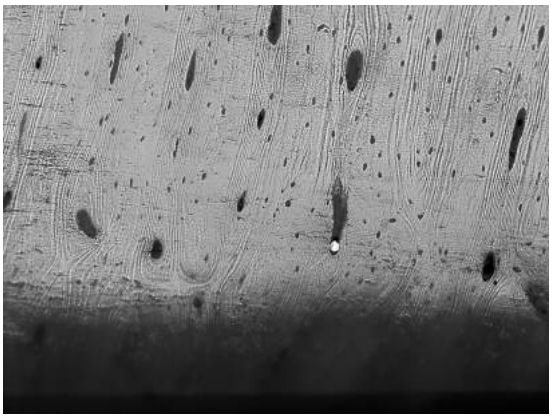

(f) Porosity of the axial-polished face image sample F12 part 12/12

Figure A.26: Porosity of axial-polished face from sample F12. LM magnification of 100x

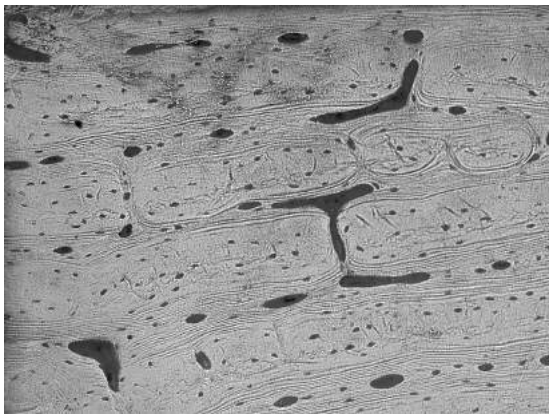

(a) Porosity of the axial-polished face image sample F13 part 1/12

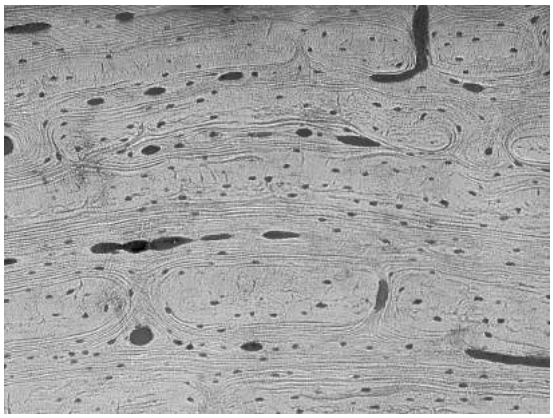

(b) Porosity of the axial-polished face image sample F13 part 2/12

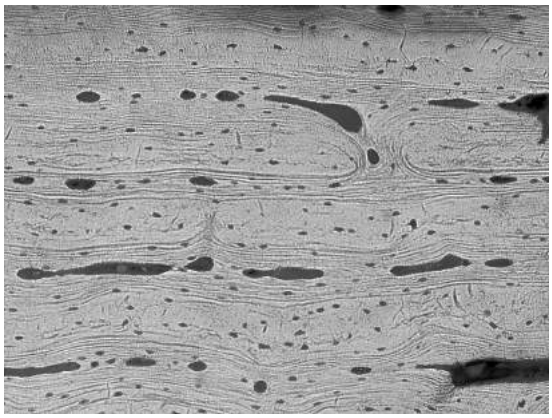

(c) Porosity of the axial-polished face image sample F13 part 3/12

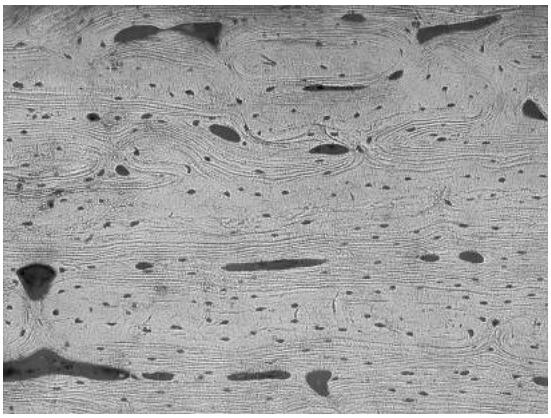

(d) Porosity of the axial-polished face image sample F13 part 4/12

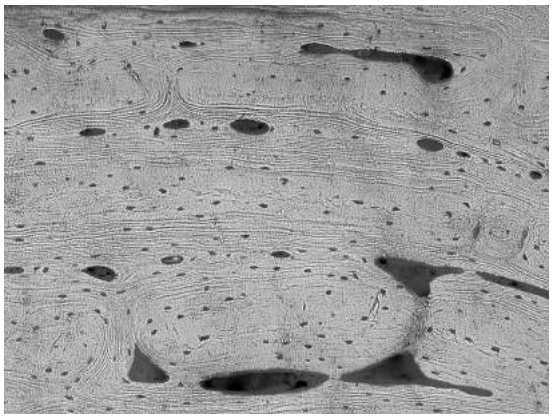

(e) Porosity of the axial-polished face image sample F13 part 5/12

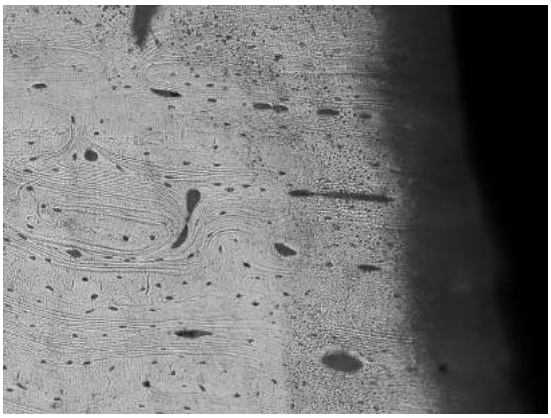

(f) Porosity of the axial-polished face image sample F13 part 6/12

Figure A.27: Porosity of axial-polished face from sample F13. LM magnification of 100x

(a) Porosity of the axial-polished face image sample F13 part 7/12

(b) Porosity of the axial-polished face image sample F13 part 8/12

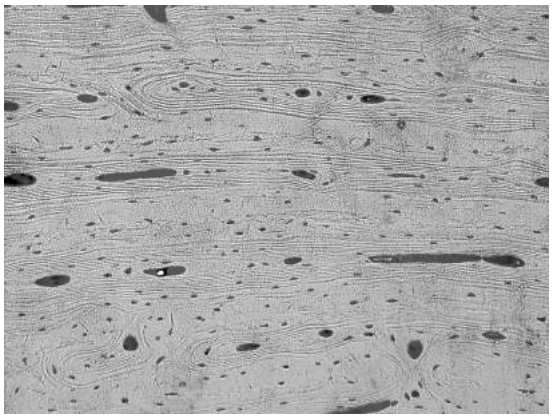

(c) Porosity of the axial-polished face image sample F13 part 9/12

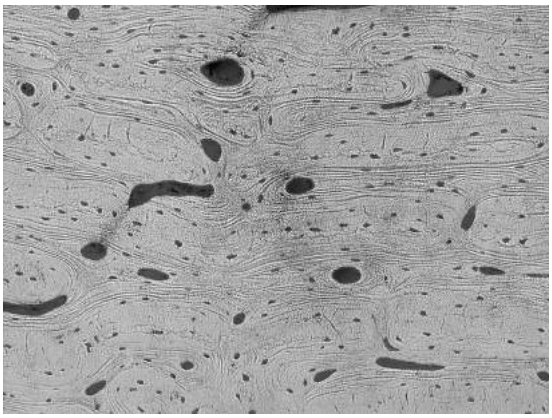

(d) Porosity of the axial-polished face image sample F13 part 10/12

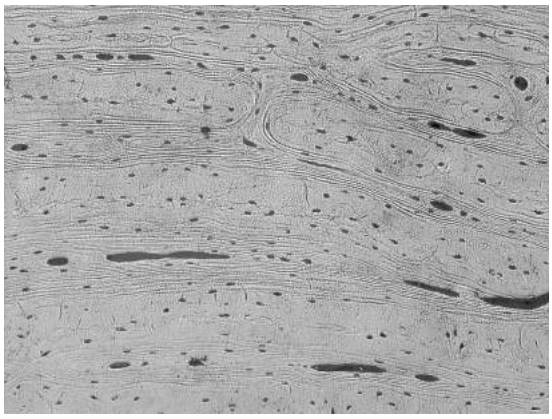

(e) Porosity of the axial-polished face image sample F13 part 11/12

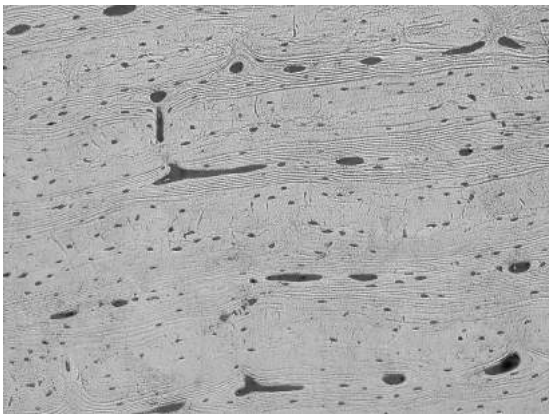

(f) Porosity of the axial-polished face image sample F13 part 12/12

Figure A.28: Porosity of axial-polished face from sample F13. LM magnification of 100x

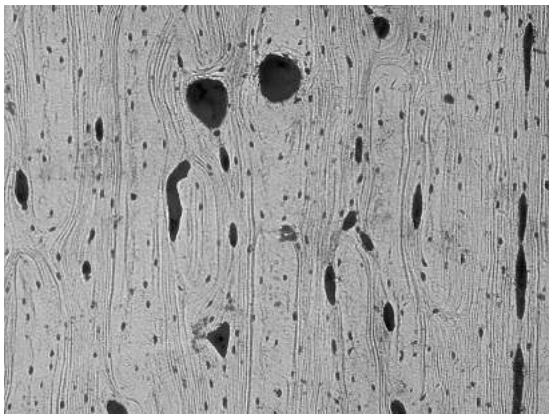

(a) Porosity of the axial-polished face image sample F14 part 1/10

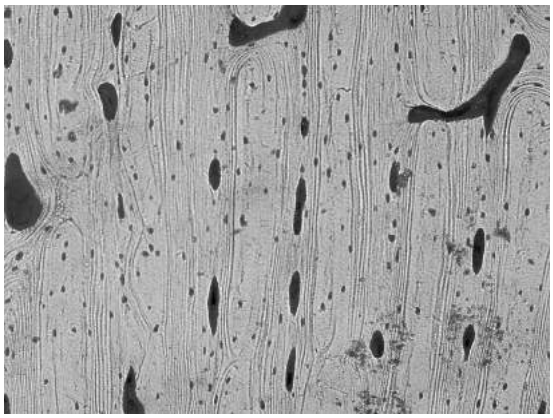

(b) Porosity of the axial-polished face image sample F14 part 2/10

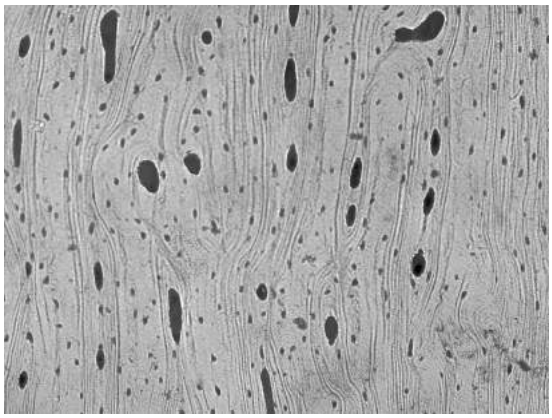

(c) Porosity of the axial-polished face image sample F14 part 3/10

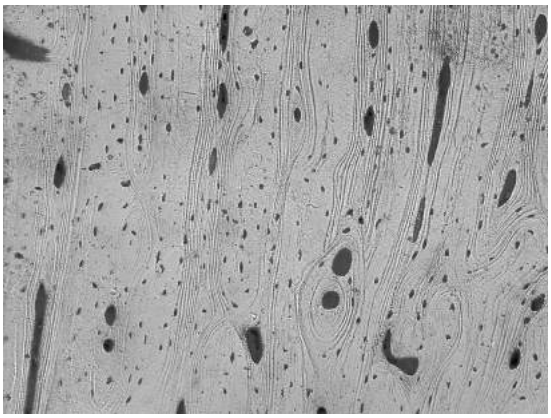

(d) Porosity of the axial-polished face image sample F14 part 4/10

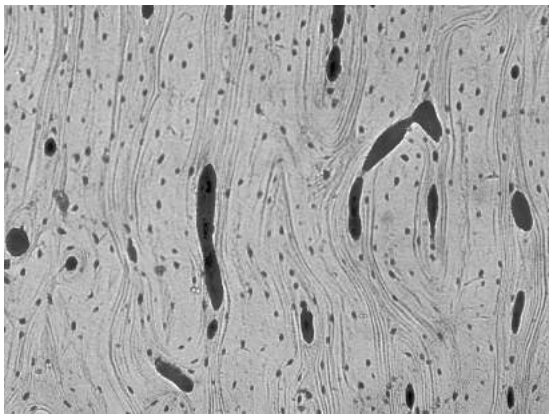

(e) Porosity of the axial-polished face image sample F14 part 5/10

(f) Porosity of the axial-polished face image sample F14 part 6/10

Figure A.29: Porosity of axial-polished face from sample F14. LM magnification of 100x

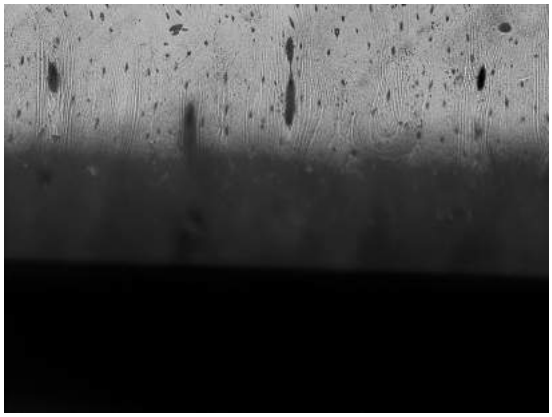

(a) Porosity of the axial-polished face image sample F14 part 7/10

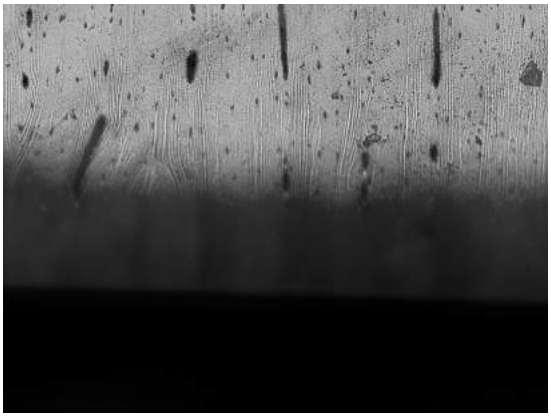

(b) Porosity of the axial-polished face image sample F14 part 8/10

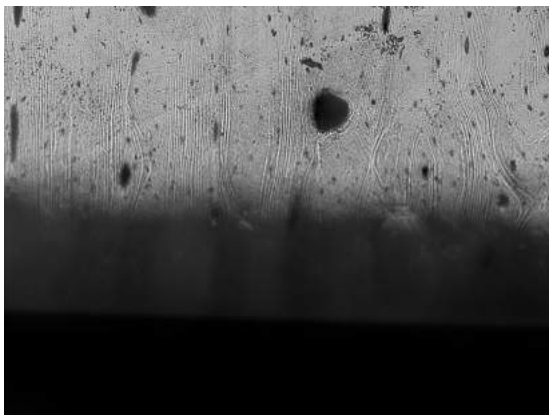

(c) Porosity of the axial-polished face image sample F14 part 9/10

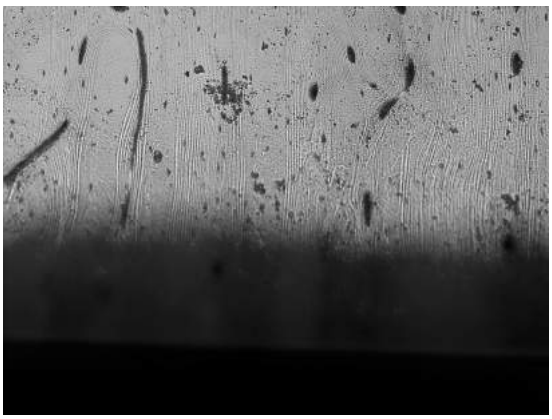

(d) Porosity of the axial-polished face image sample F14 part 10/10

Figure A.30: Porosity of axial-polished face from sample F14. LM magnification of 100x

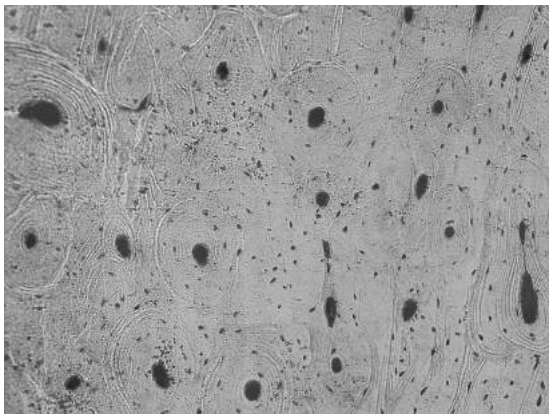

(a) Porosity of the axial-polished face image sample F15 part 1/7

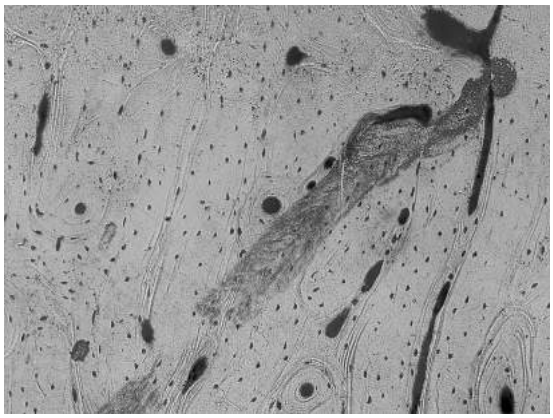

(b) Porosity of the axial-polished face image sample F15 part 2/7

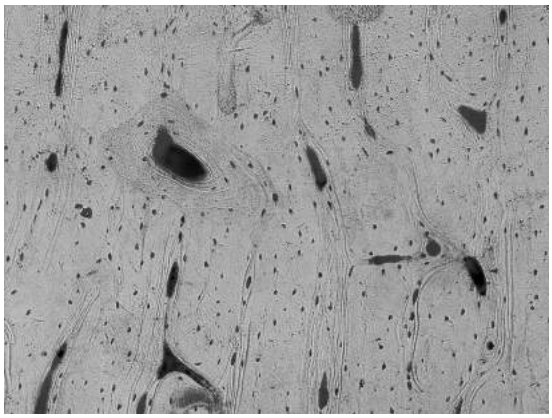

(c) Porosity of the axial-polished face image sample F15 part 3/7

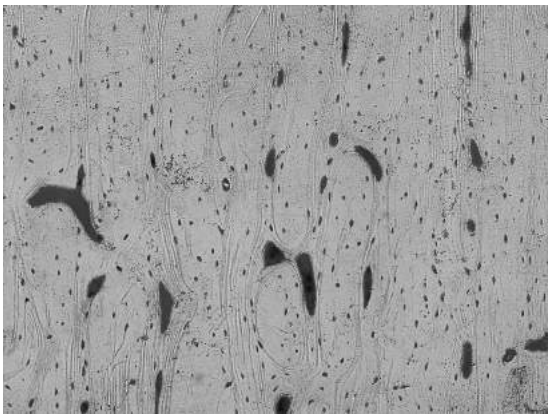

(d) Porosity of the axial-polished face image sample F15 part 4/7

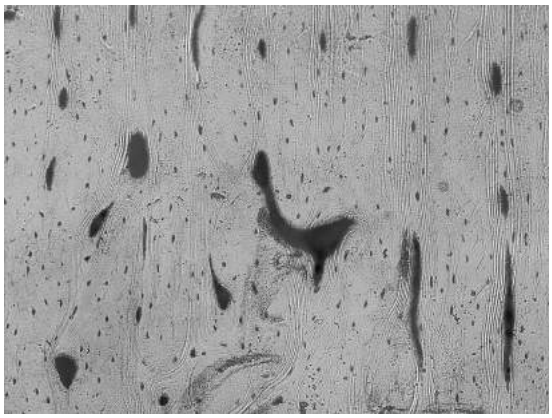

(e) Porosity of the axial-polished face image sample F15 part 5/7

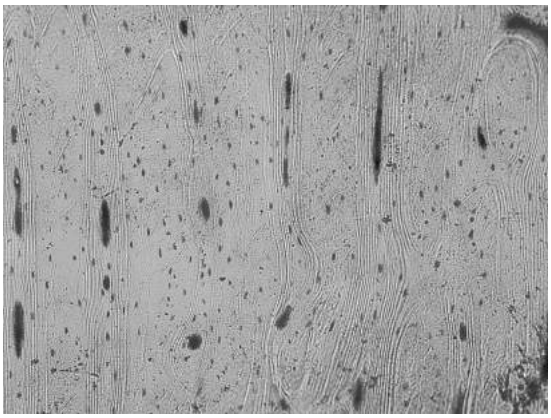

(f) Porosity of the axial-polished face image sample F15 part 6/7

Figure A.31: Porosity of axial-polished face from sample F15. LM magnification of 100x

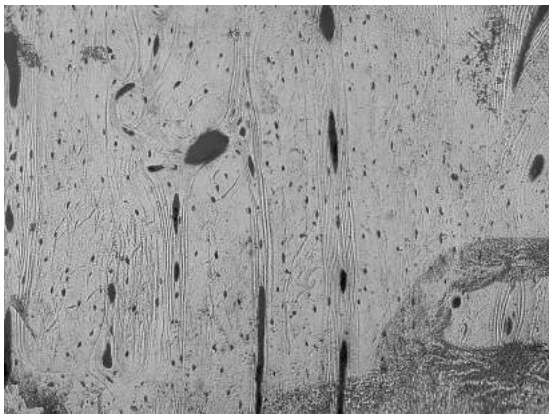

(a) Porosity of the axial-polished face image sample F15 part 7/7

Figure A.32: Porosity of axial-polished face from sample F15. LM magnification of 100x

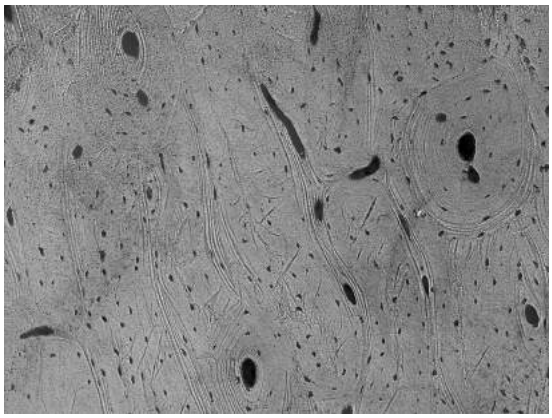

(a) Porosity of the axial-polished face image sample F16 part 1/10

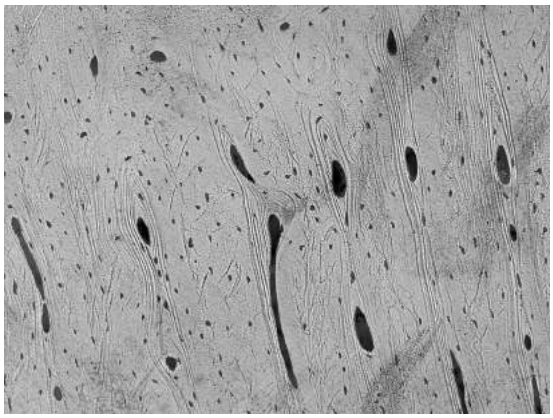

(b) Porosity of the axial-polished face image sample F16 part 2/10

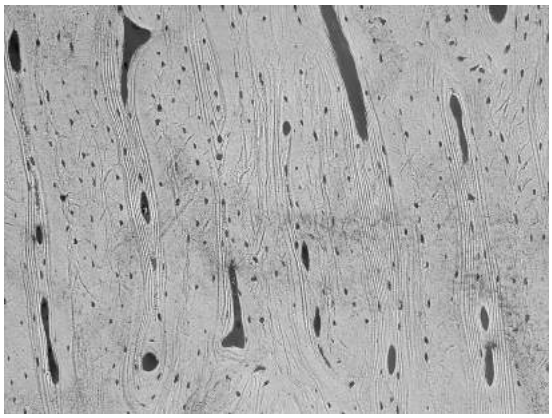

(c) Porosity of the axial-polished face image sample F16 part 3/10

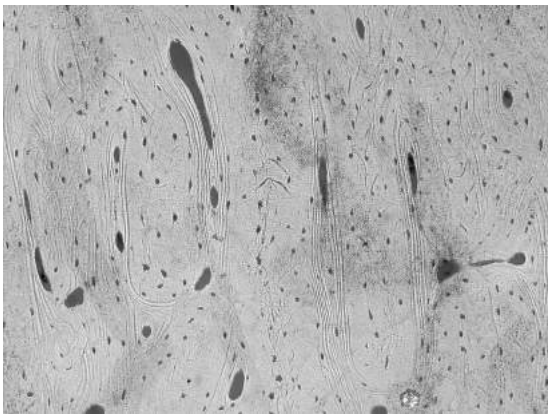

(d) Porosity of the axial-polished face image sample F16 part 4/10

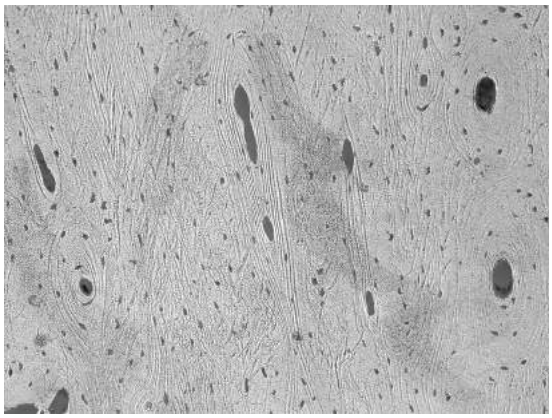

(e) Porosity of the axial-polished face image sample F16 part 5/10

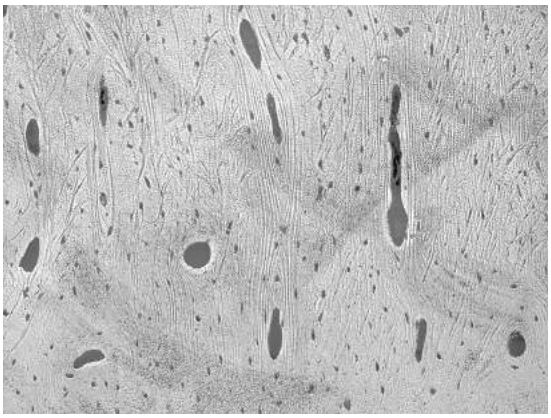

(f) Porosity of the axial-polished face image sample F16 part 6/10

Figure A.33: Porosity of axial-polished face from sample F16. LM magnification of 100x

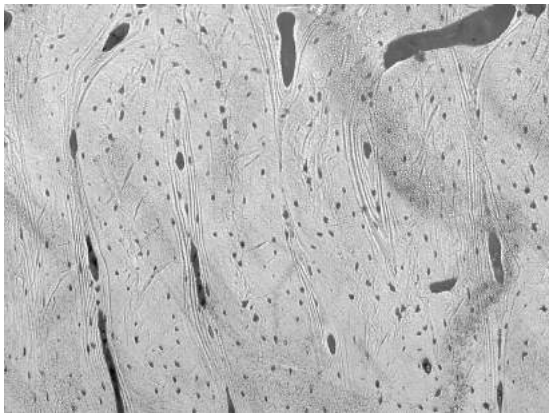

(a) Porosity of the axial-polished face image sample F16 part 7/10

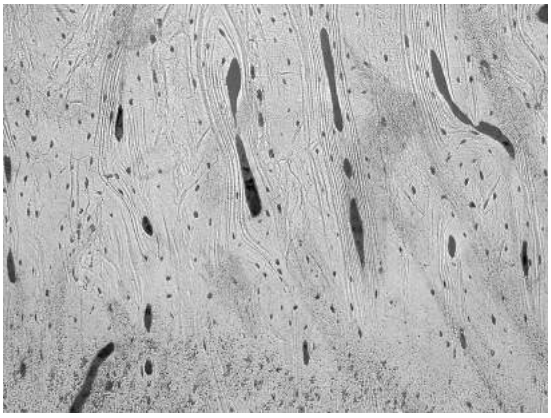

(b) Porosity of the axial-polished face image sample F16 part 8/10

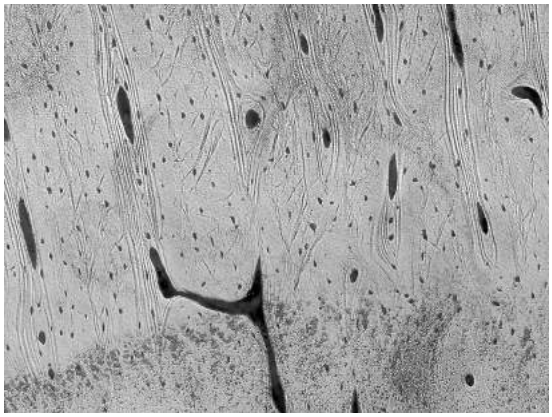

(c) Porosity of the axial-polished face image sample F16 part 9/10

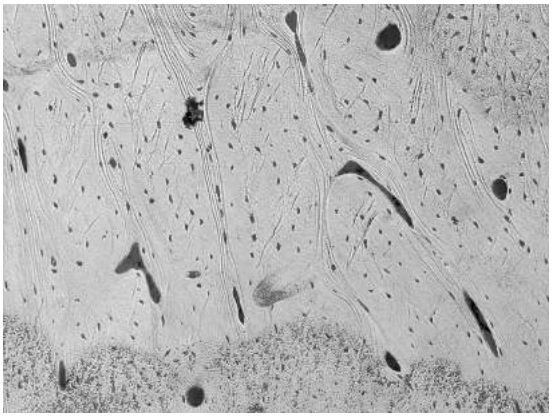

(d) Porosity of the axial-polished face image sample F16 part 10/10

Figure A.34: Porosity of axial-polished face from sample F16. LM magnification of 100x

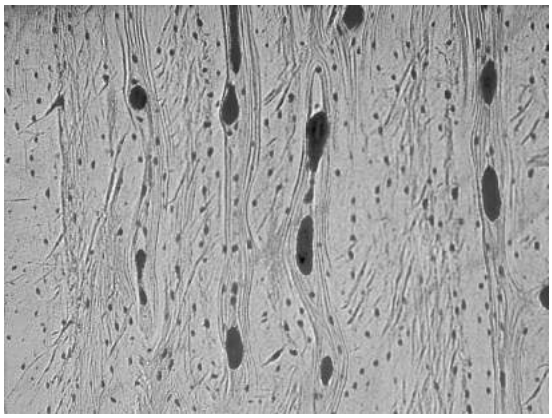

(a) Porosity of the axial-polished face image sample F17 part 1/12

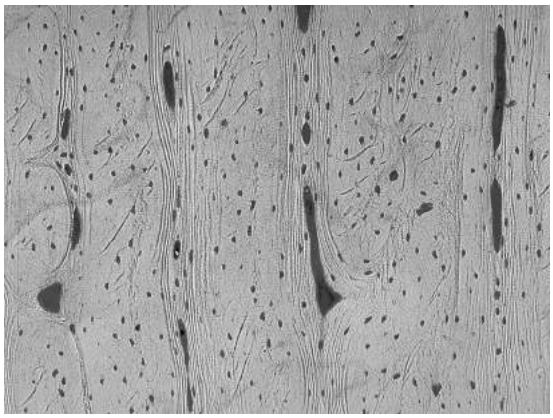

(b) Porosity of the axial-polished face image sample F17 part 2/12

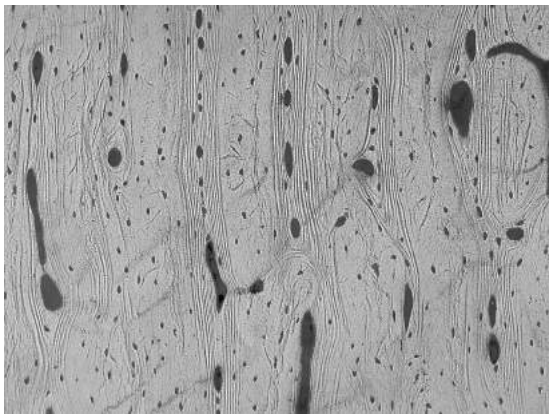

(c) Porosity of the axial-polished face image sample F17 part 3/12

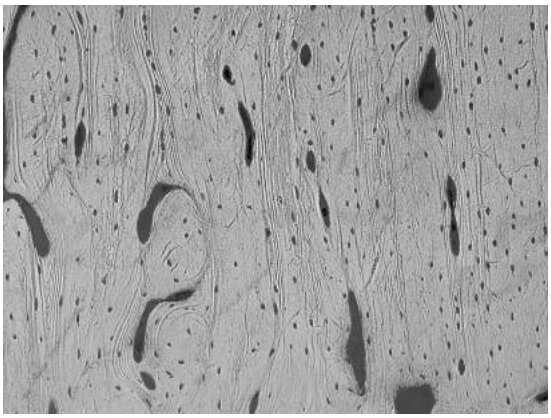

(d) Porosity of the axial-polished face image sample F17 part 4/12

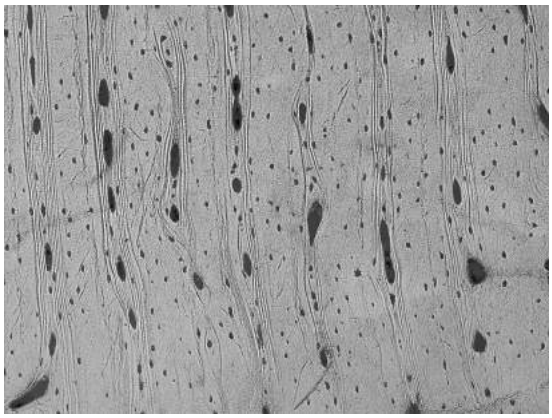

(e) Porosity of the axial-polished face image sample F17 part 5/12

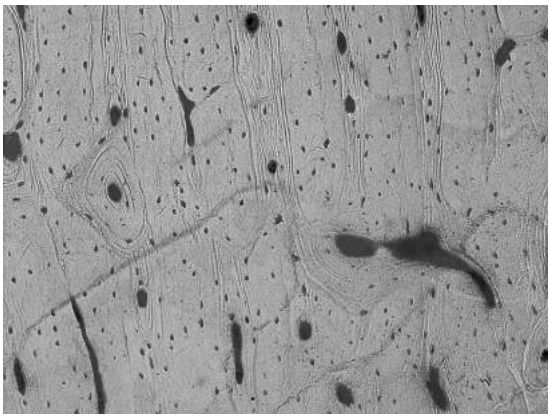

(f) Porosity of the axial-polished face image sample F17 part 6/12

Figure A.35: Porosity of axial-polished face from sample F17. LM magnification of 100x

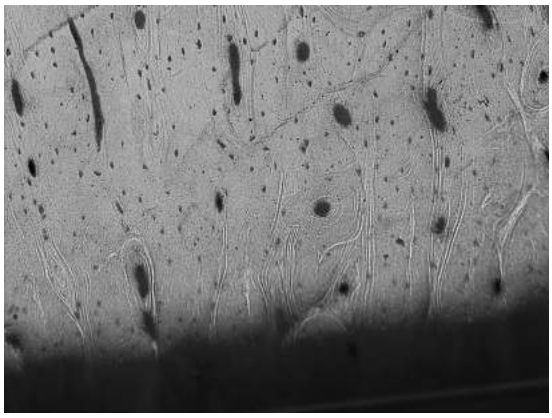

(a) Porosity of the axial-polished face image sample F17 part 7/12

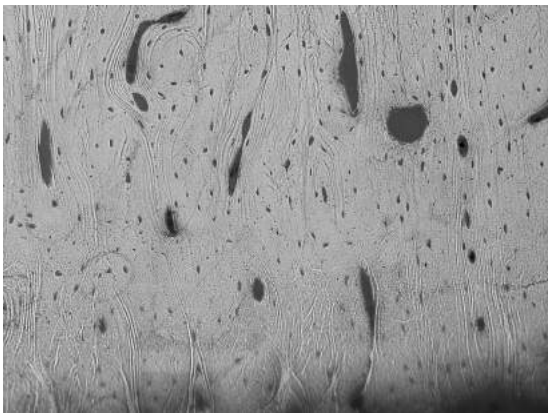

(b) Porosity of the axial-polished face image sample F17 part 8/12

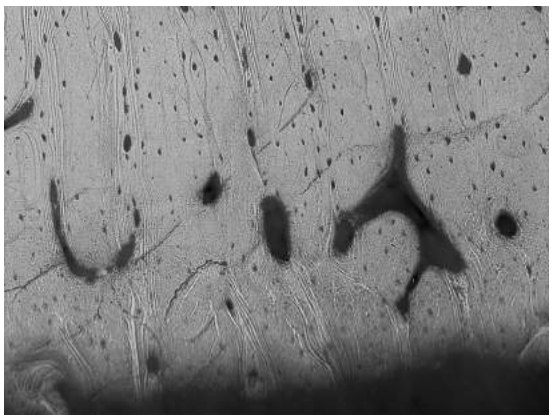

(c) Porosity of the axial-polished face image sample F17 part 9/12

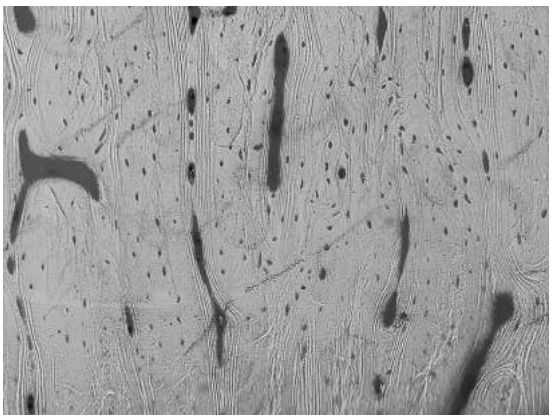

(d) Porosity of the axial-polished face image sample F17 part 10/12

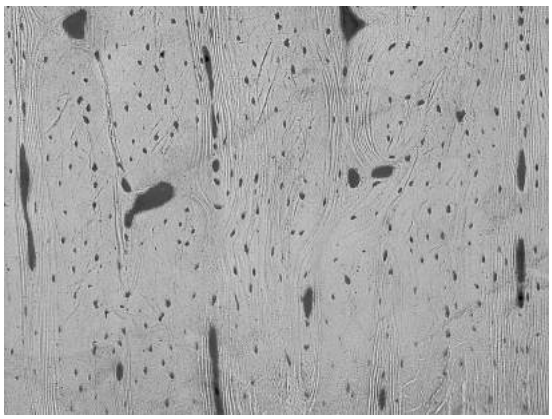

(e) Porosity of the axial-polished face image sample F17 part 11/12

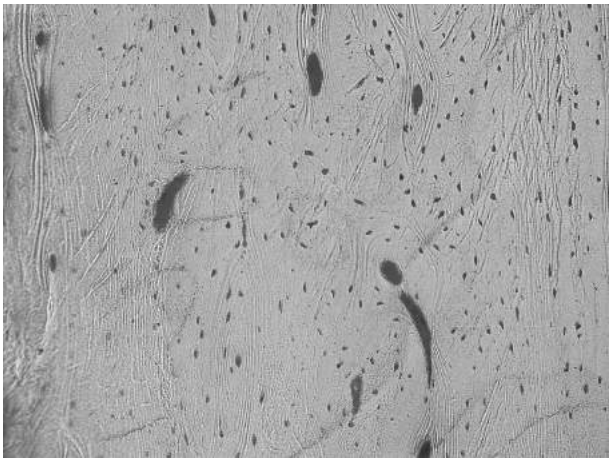

(f) Porosity of the axial-polished face image sample F17 part 12/12

Figure A.36: Porosity of axial-polished face from sample F17. LM magnification of 100x

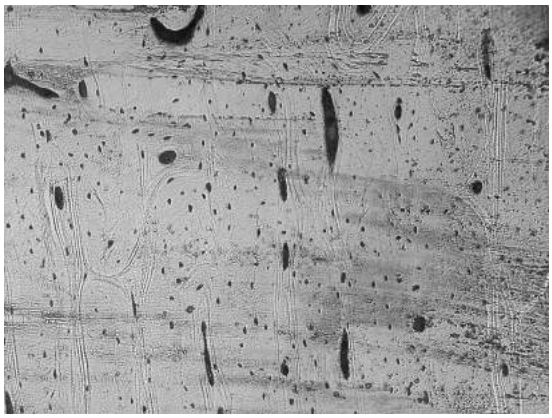

(a) Porosity of the axial-polished face image sample F18 part 1/10

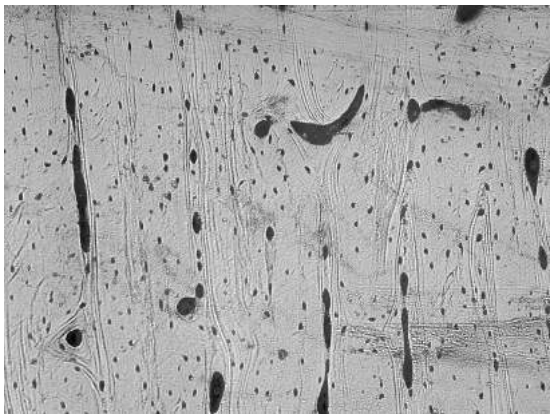

(b) Porosity of the axial-polished face image sample F18 part 2/10

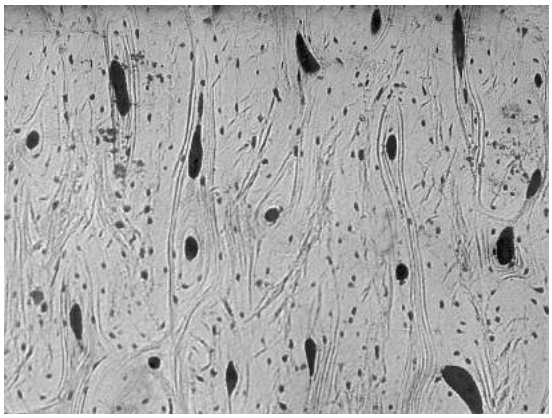

(c) Porosity of the axial-polished face image sample F18 part 3/10

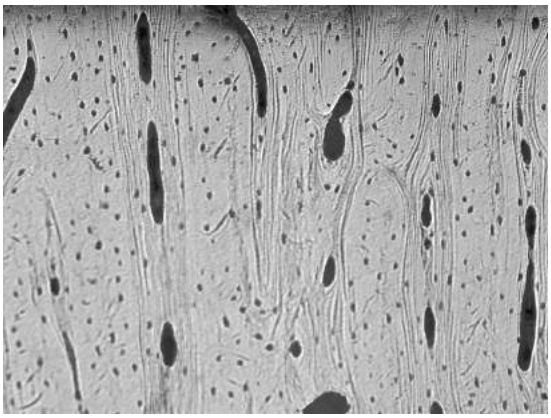

(d) Porosity of the axial-polished face image sample F18 part 4/10

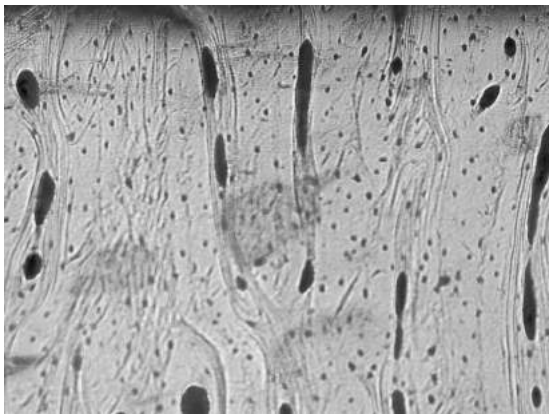

(e) Porosity of the axial-polished face image sample F18 part 5/10

(f) Porosity of the axial-polished face image sample F18 part 6/10

Figure A.37: Porosity of axial-polished face from sample F18. LM magnification of 100x

(a) Porosity of the axial-polished face image sample F18 part 7/10

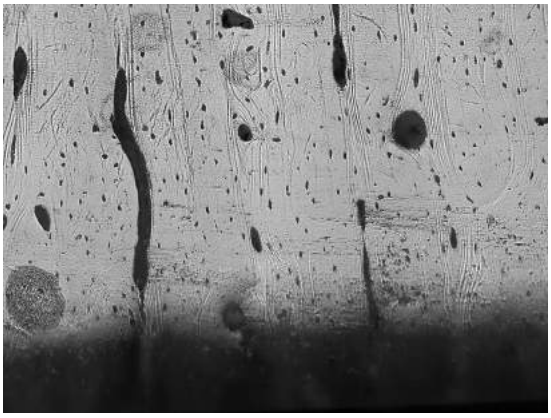

(b) Porosity of the axial-polished face image sample F18 part 8/10

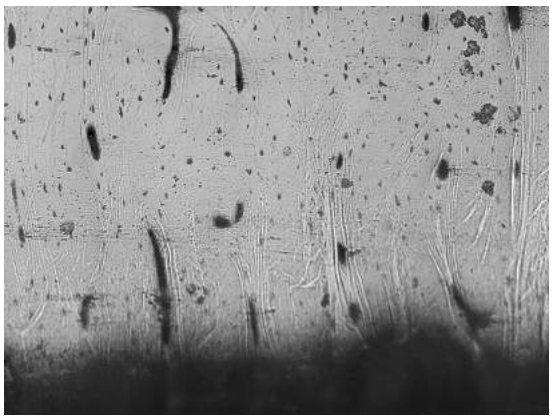

(c) Porosity of the axial-polished face image sample F18 part 9/10

(d) Porosity of the axial-polished face image sample F18 part 10/10

Figure A.38: Porosity of axial-polished face from sample F18. LM magnification of 100x

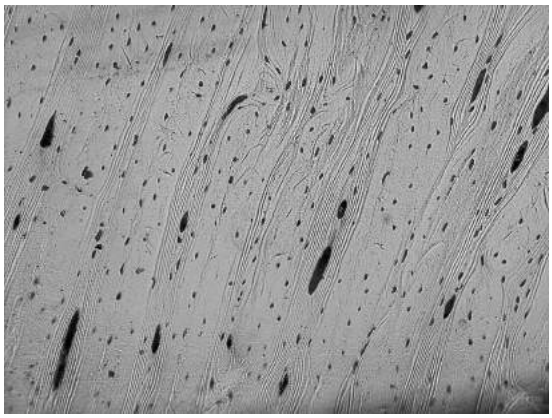

(a) Porosity of the axial-polished face image sample FX1 part 1/6

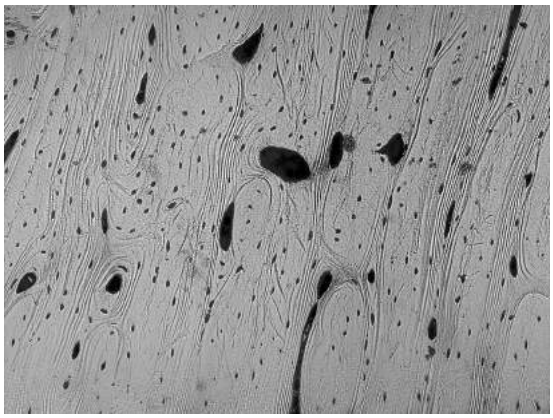

(b) Porosity of the axial-polished face image sample FX1 part 2/6

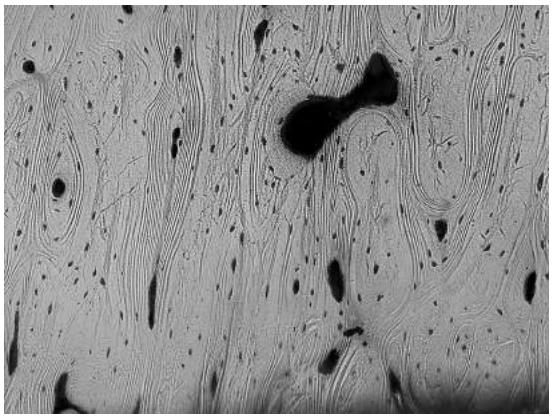

(c) Porosity of the axial-polished face image sample FX1 part 3/6

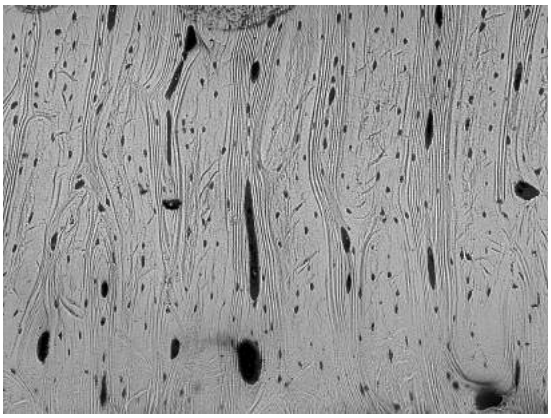

(d) Porosity of the axial-polished face image sample FX1 part 4/6

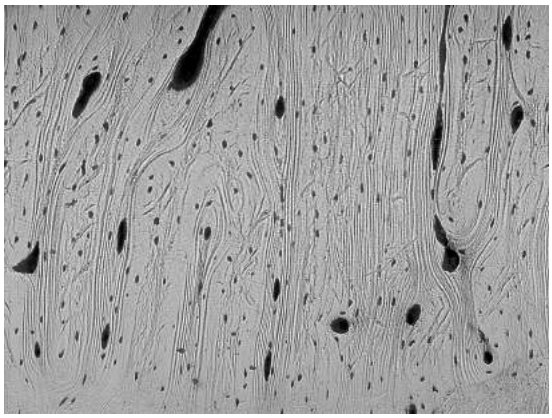

(e) Porosity of the axial-polished face image sample FX1 part 5/6

(f) Porosity of the axial-polished face image sample FX1 part 6/6

Figure A.39: Porosity of axial-polished face from sample FX1. LM magnification of 100x

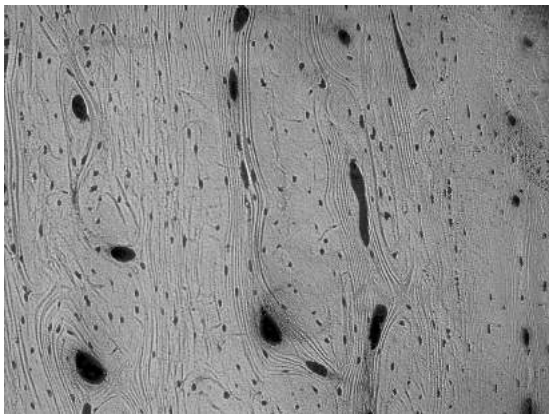

(a) Porosity of the axial-polished face image sample FX2 part 1/12

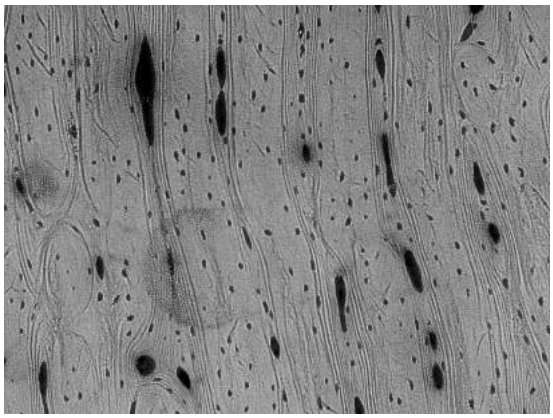

(b) Porosity of the axial-polished face image sample FX2 part 2/12

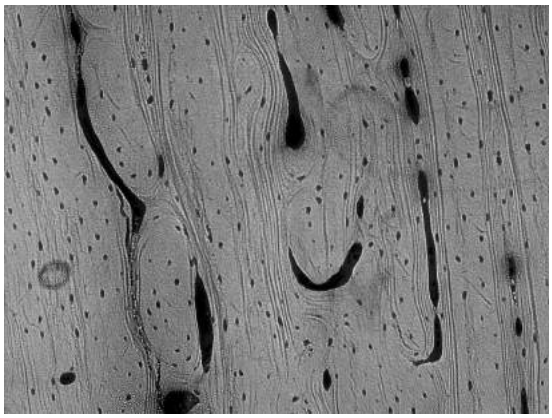

(c) Porosity of the axial-polished face image sample FX2 part 3/12

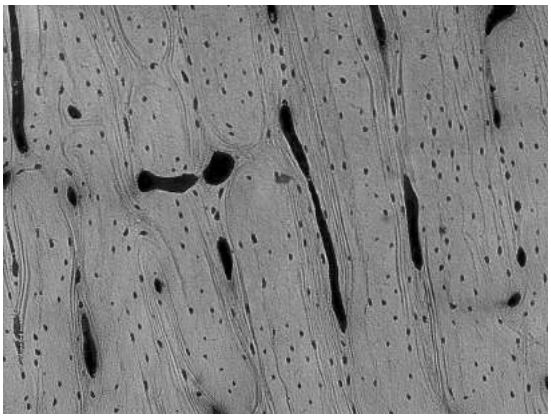

(d) Porosity of the axial-polished face image sample FX2 part 4/12

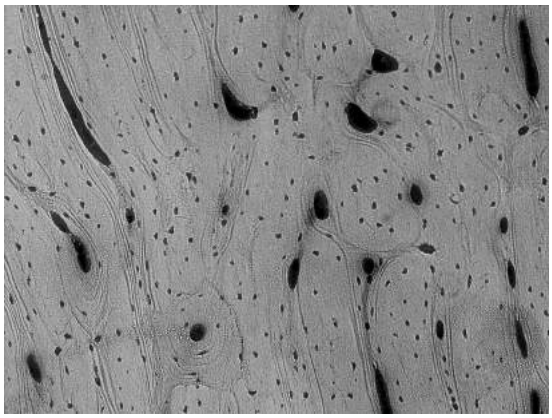

(e) Porosity of the axial-polished face image sample FX2 part 5/12

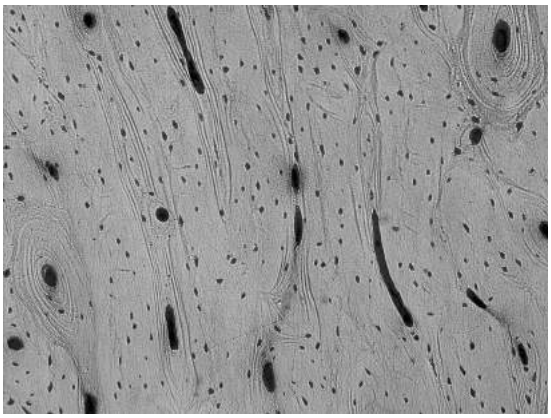

(f) Porosity of the axial-polished face image sample FX2 part 6/12

Figure A.40: Porosity of axial-polished face from sample FX2. LM magnification of 100x

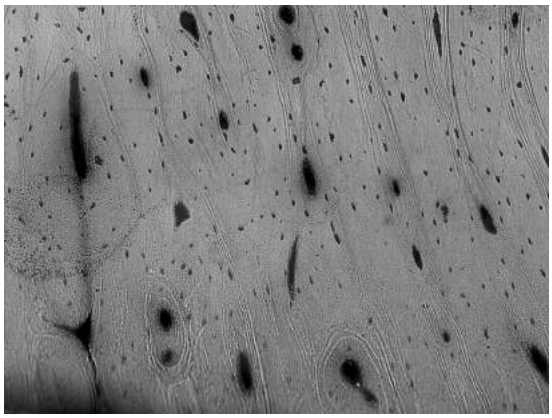

(a) Porosity of the axial-polished face image sample FX2 part 7/12

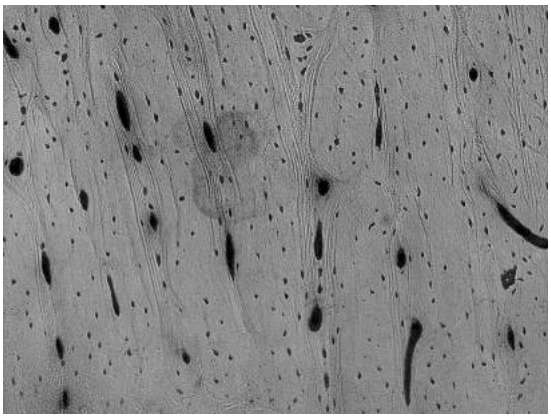

(b) Porosity of the axial-polished face image sample FX2 part 8/12

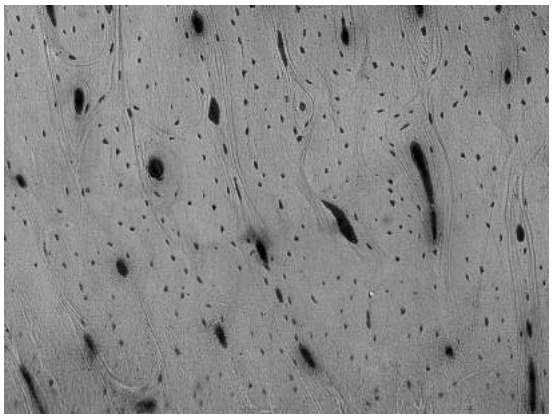

(c) Porosity of the axial-polished face image sample FX2 part 9/12

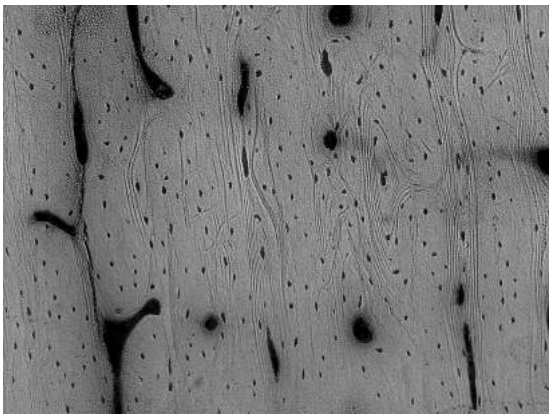

(d) Porosity of the axial-polished face image sample FX2 part 10/12

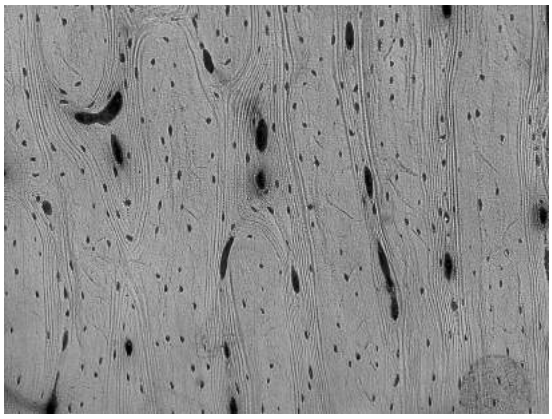

(e) Porosity of the axial-polished face image sample FX2 part 11/12

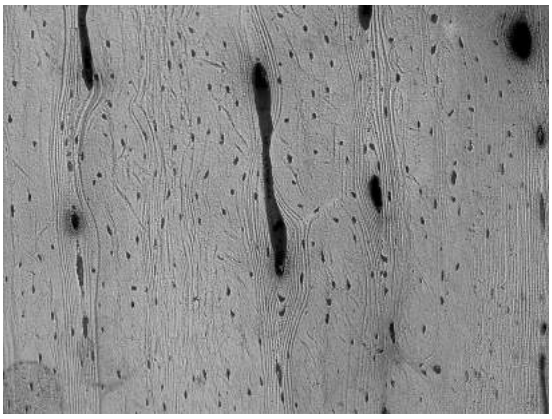

(f) Porosity of the axial-polished face image sample FX2 part 12/12

Figure A.41: Porosity of axial-polished face from sample FX2. LM magnification of 100x

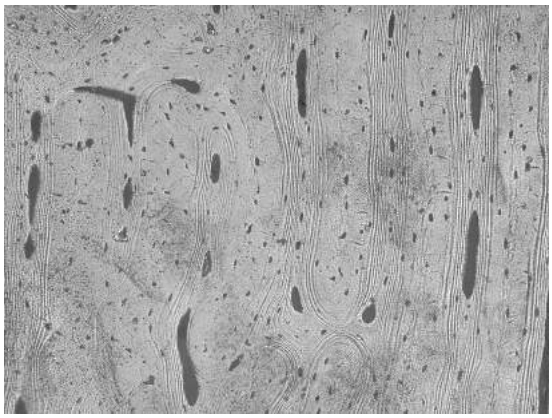

(a) Porosity of the axial-polished face image sample FX3 part 1/8

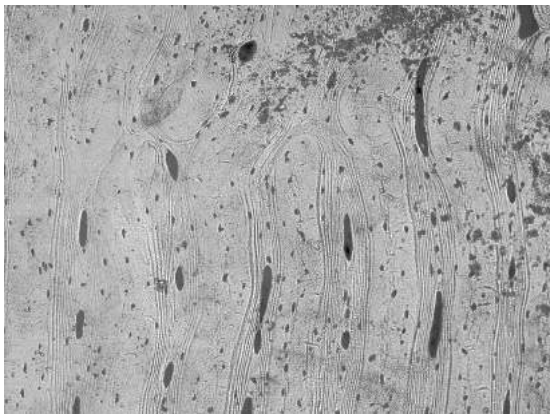

(b) Porosity of the axial-polished face image sample FX3 part 2/8

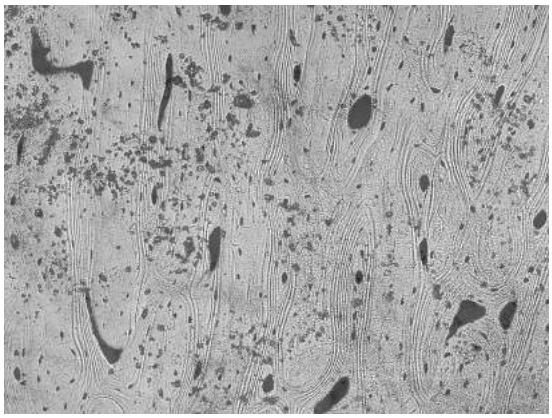

(c) Porosity of the axial-polished face image sample FX3 part 3/8

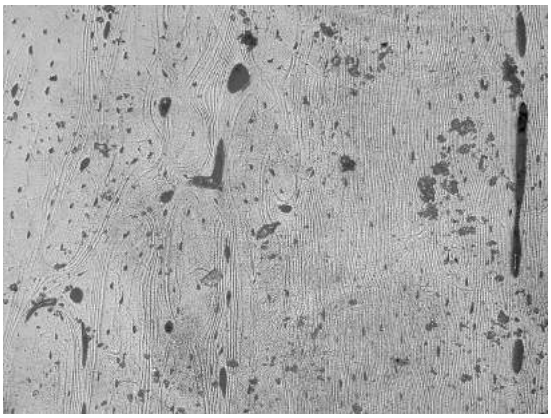

(d) Porosity of the axial-polished face image sample FX3 part 4/8

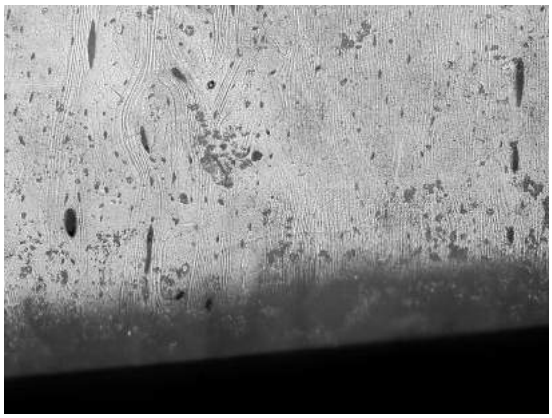

(e) Porosity of the axial-polished face image sample FX3 part 5/8

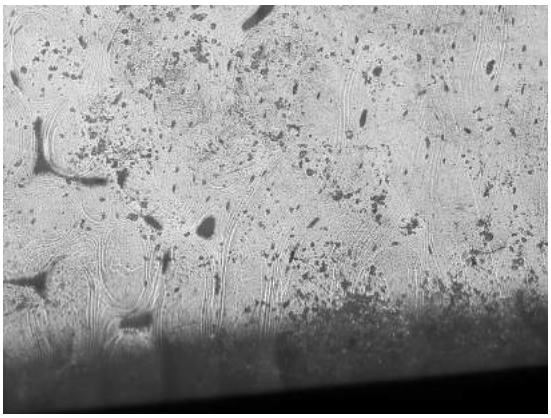

(f) Porosity of the axial-polished face image sample FX3 part 6/8

Figure A.42: Porosity of axial-polished face from sample FX3. LM magnification of 100x

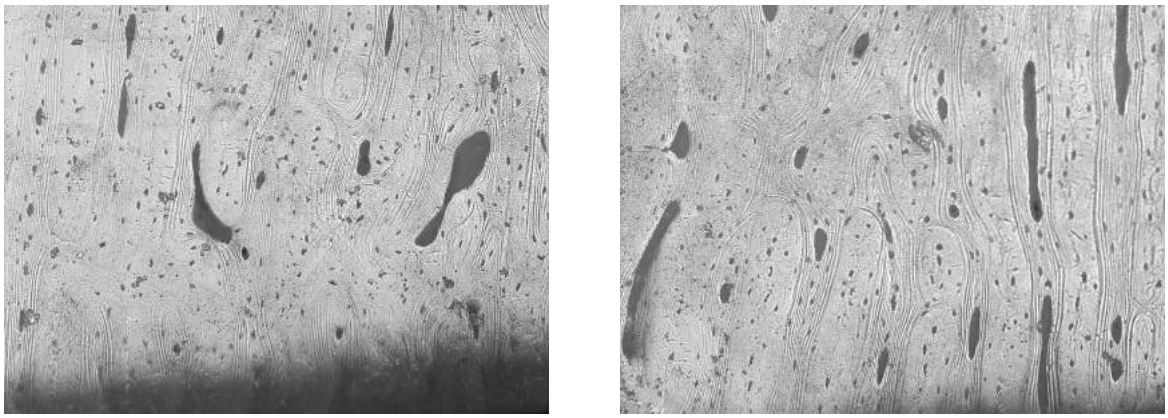

(a) Porosity of the axial-polished face image sample FX3 part 7/8

(b) Porosity of the axial-polished face image sample FX3 part 8/8

Figure A.43: Porosity of axial-polished face from sample FX3. LM magnification of 100x

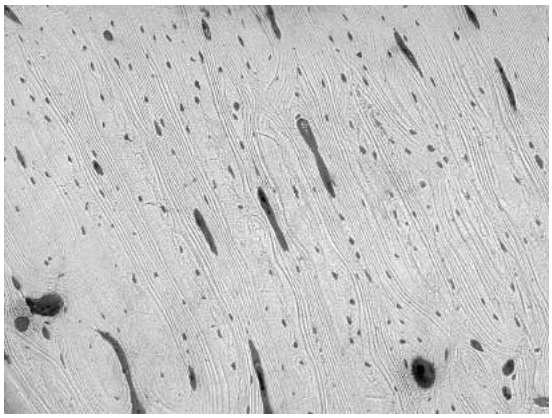

(a) Porosity of the axial-polished face image sample FX4 part 1/10

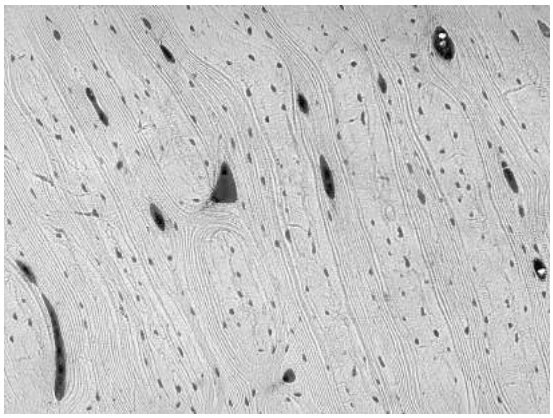

(b) Porosity of the axial-polished face image sample FX4 part 2/10

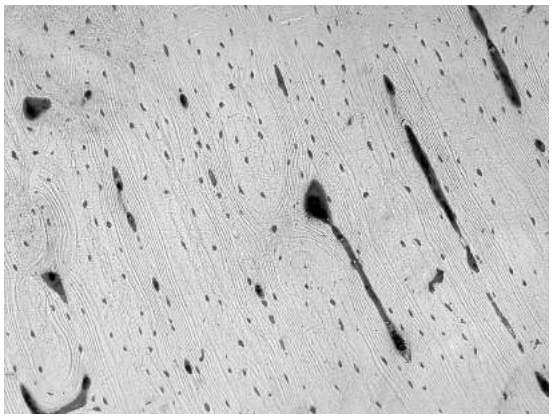

(c) Porosity of the axial-polished face image sample FX4 part 3/10

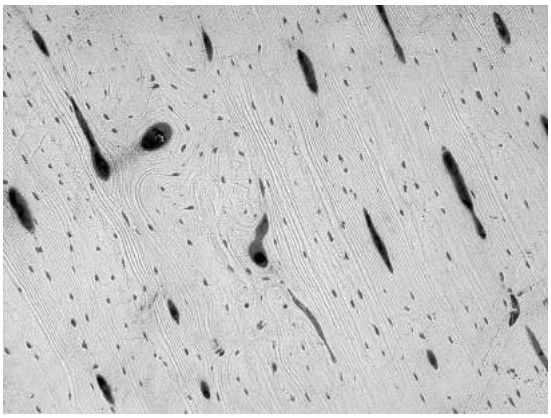

(d) Porosity of the axial-polished face image sample FX4 part 4/10

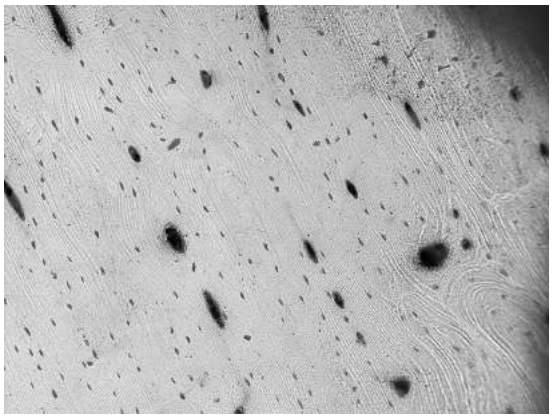

(e) Porosity of the axial-polished face image sample FX4 part 5/10

(f) Porosity of the axial-polished face image sample FX4 part 6/10

Figure A.44: Porosity of axial-polished face from sample FX4. LM magnification of 100x

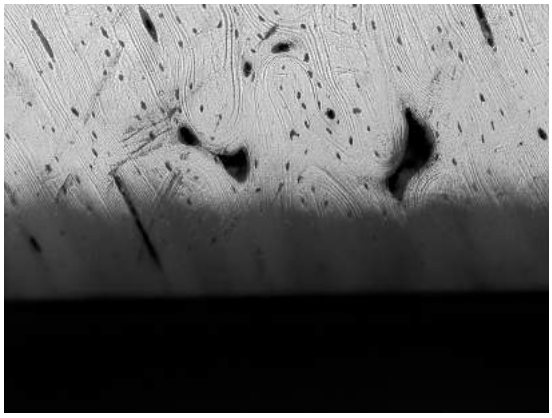

(a) Porosity of the axial-polished face image sample FX4 part 7/10

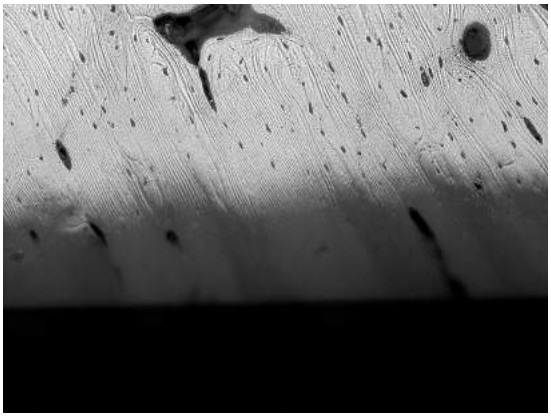

(b) Porosity of the axial-polished face image sample FX4 part 8/10

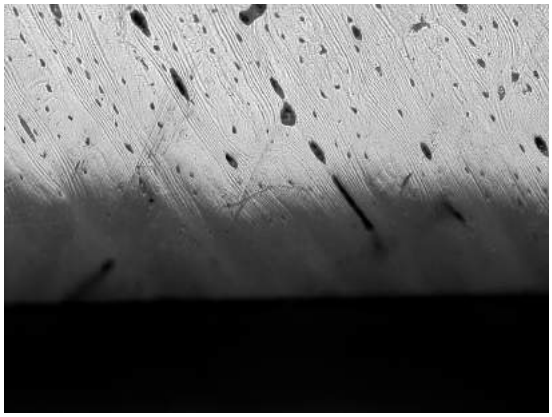

(c) Porosity of the axial-polished face image sample FX4 part 9/10

(d) Porosity of the axial-polished face image sample FX4 part 10/10

Figure A.45: Porosity of axial-polished face from sample FX4. LM magnification of 100x

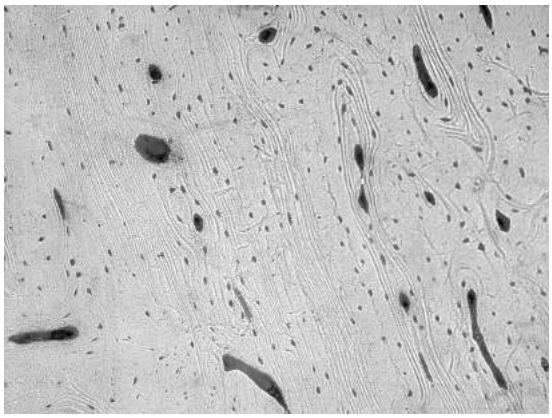

(a) Porosity of the axial-polished face image sample FX5 part 1/12

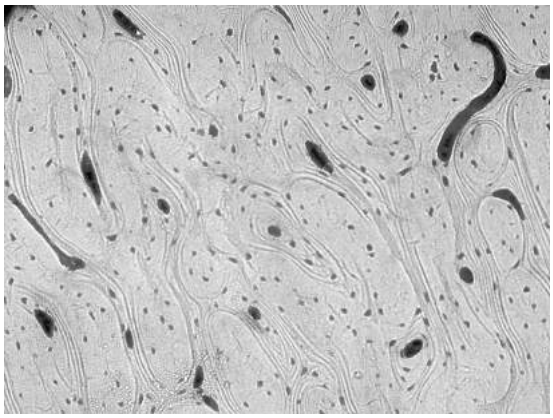

(b) Porosity of the axial-polished face image sample FX5 part 2/12

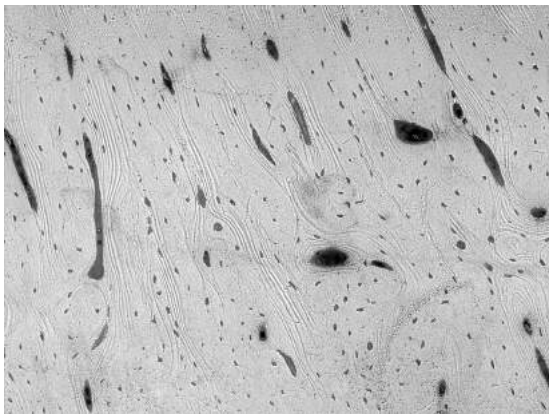

(c) Porosity of the axial-polished face image sample FX5 part 3/12

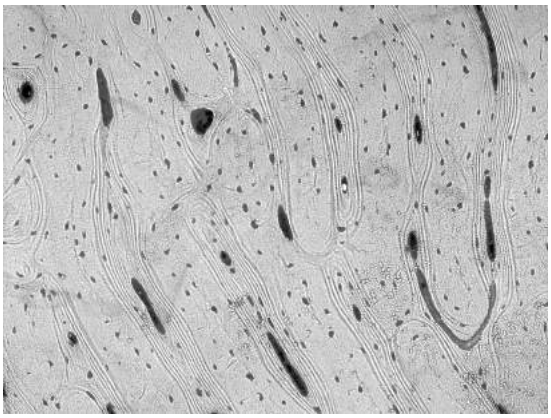

(d) Porosity of the axial-polished face image sample FX5 part 4/12

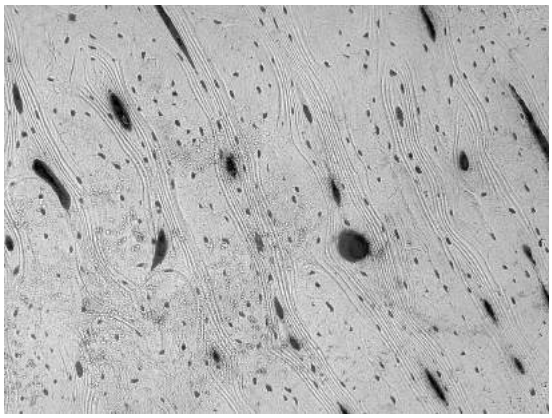

(e) Porosity of the axial-polished face image sample FX5 part 5/12

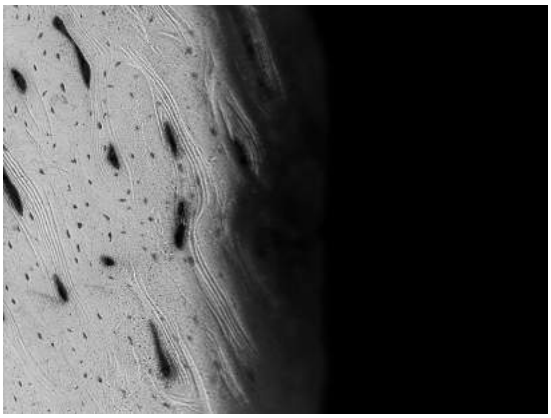

(f) Porosity of the axial-polished face image sample FX5 part 6/12

Figure A.46: Porosity of axial-polished face from sample FX5. LM magnification of 100x

(a) Porosity of the axial-polished face image sample FX5 part 7/12

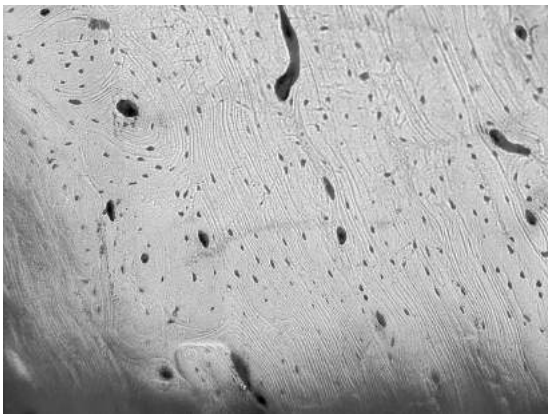

(b) Porosity of the axial-polished face image sample FX5 part 8/12

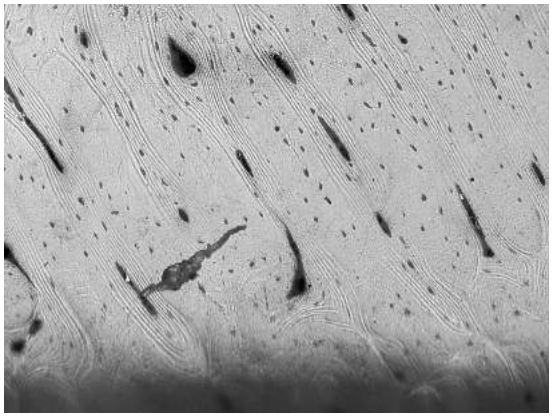

(c) Porosity of the axial-polished face image sample FX5 part 9/12

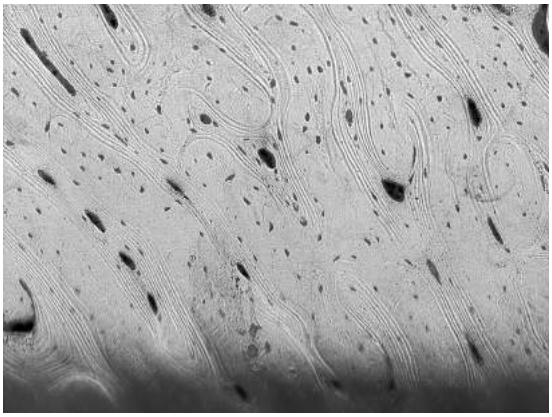

(d) Porosity of the axial-polished face image sample FX5 part 10/12

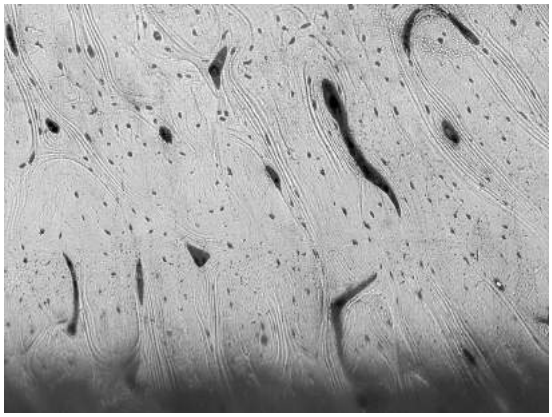

(e) Porosity of the axial-polished face image sample FX5 part 11/12

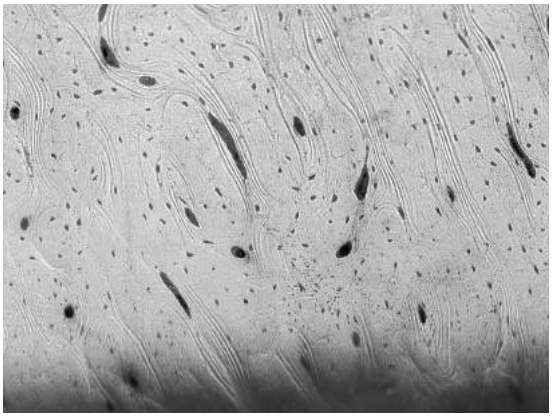

(f) Porosity of the axial-polished face image sample FX5 part 12/12

Figure A.47: Porosity of axial-polished face from sample FX5. LM magnification of 100x

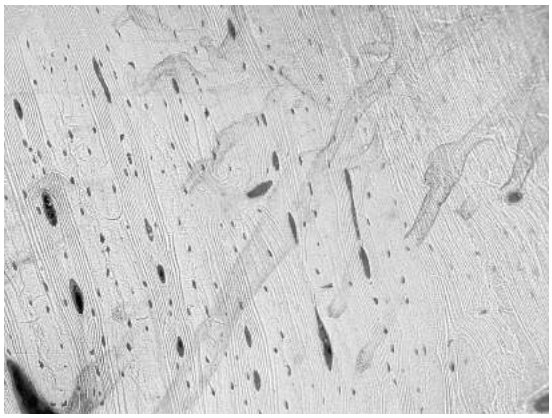

(a) Porosity of the axial-polished face image sample FX6 part 1/10

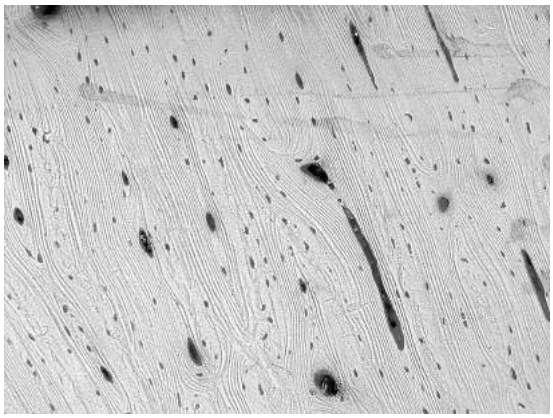

(b) Porosity of the axial-polished face image sample FX6 part 2/10

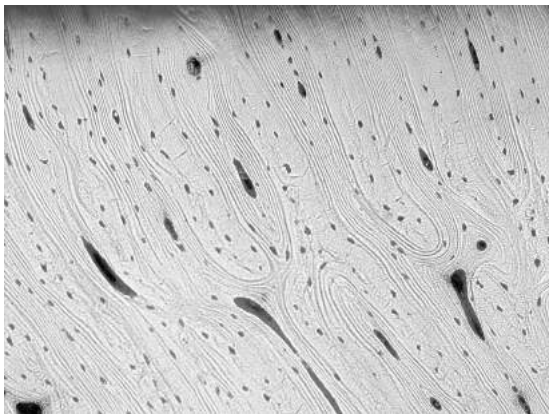

(c) Porosity of the axial-polished face image sample FX6 part 3/10

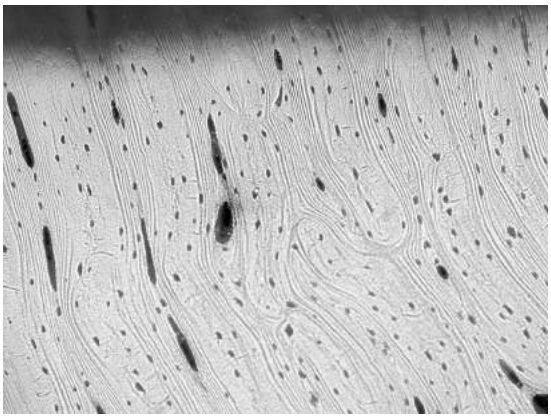

(d) Porosity of the axial-polished face image sample FX6 part 4/10

(e) Porosity of the axial-polished face image sample FX6 part 5/10

(f) Porosity of the axial-polished face image sample FX6 part 6/10

Figure A.48: Porosity of axial-polished face from sample FX6. LM magnification of 100x

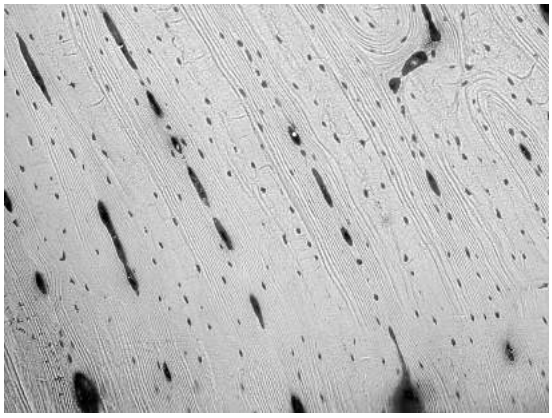

(a) Porosity of the axial-polished face image sample FX6 part 7/10

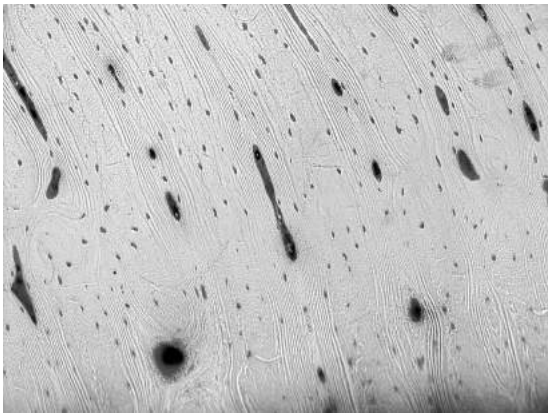

(b) Porosity of the axial-polished face image sample FX6 part 8/10

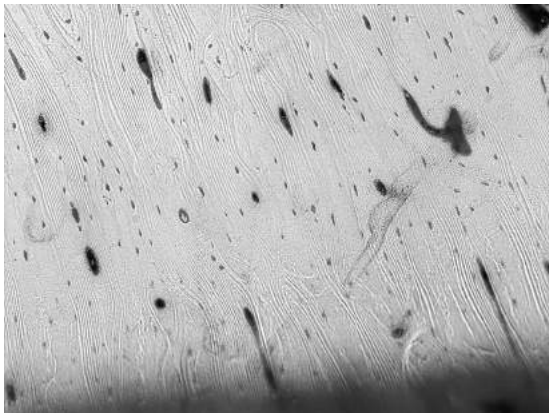

(c) Porosity of the axial-polished face image sample FX6 part 9/10

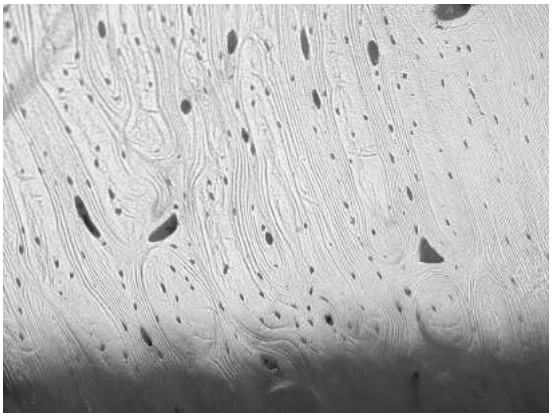

(d) Porosity of the axial-polished face image sample FX6 part 10/10

Figure A.49: Porosity of axial-polished face from sample FX6. LM magnification of 100x

APPENDIX B

Custom-made sample holder

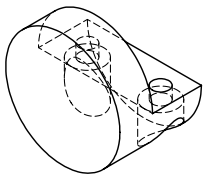

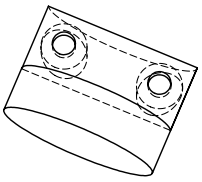

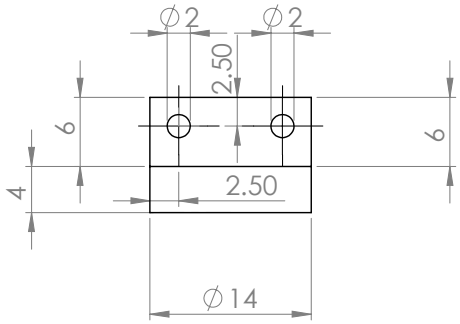

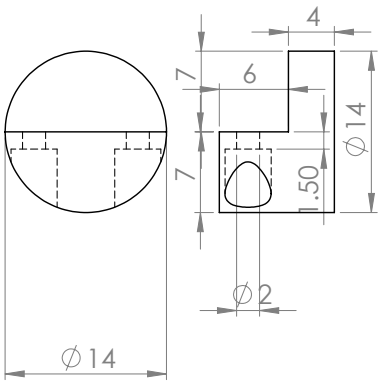

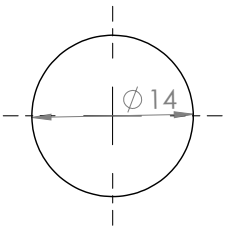

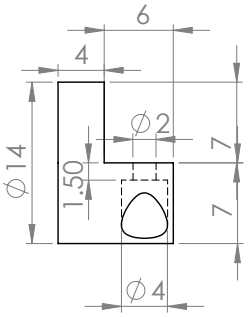

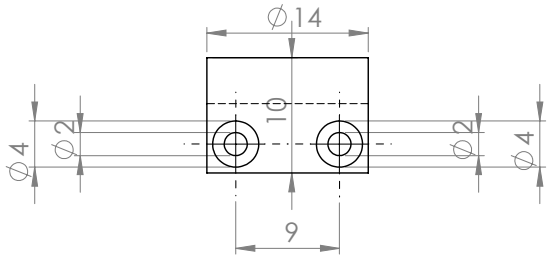

UNLESS OTHERWISE SPECIFIED: DIMENSIONS ARE IN **MILLIMETERS**	Bone sample holder 2 part from 2	Institute for Mechanics of Materials and Structures E202 TU Wien
Luis Zelaya Date: 03.12.2015	DO NOT SCALE DRAWING	TITLE: base
SHEET 1 OF 2	material: Steel Stahlmaterial	DWG NO.2 SCALE:2:1 A4

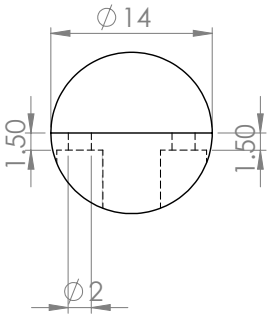

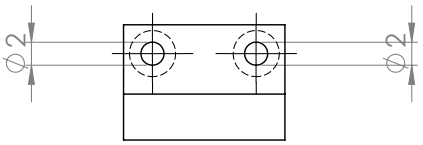

UNLESS OTHERWISE SPECIFIED:
DIMENSIONS ARE IN MILLIMETERS

Bone sample holder
2 part from 2

Institute for Mechanics of Materials and Structures
E202
TU Wien

Luis Zelaya
Date: 03.12.2015

DO NOT SCALE DRAWING

TITLE:

base

SHEET 2 OF 2

Stahlmaterial

DWG NO.2
SCALE:2:1

A4

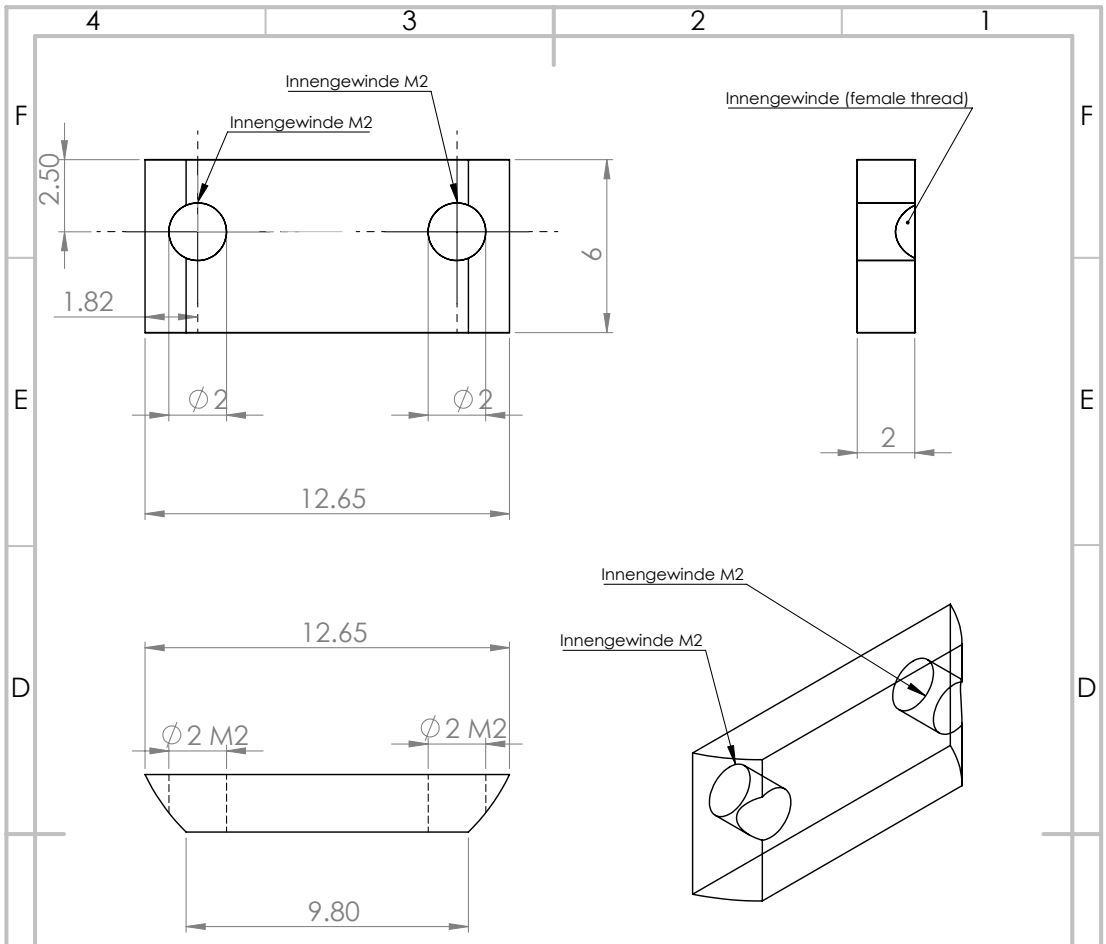

UNLESS OTHERWISE SPECIFIED: DIMENSIONS ARE IN MILLIMETERS.	Bone sample holder 1 part from 2	Institute for Mechanics of Materials and Structures E202 TU Wien
Luis Zelaya Date: 2.12.2015	DO NOT SCALE DRAWING	TITLE: female thread part
SHEET 1 OF 1	Stahlmaterial	DWG NO.1 A4 SCALE:5:1

APPENDIX C

Conference contribution

The following poster was prepared for the 33^{rd} Danubia Adria Symposium on Advances in Experimental Mechanics in Portorož, Eslovenia:

Zelaya-Lainez, L.[1], Kariem, H., Nischkauer, W., Limbeck, A., and Hellmich, C. (2016) The allocation of bone fluid in bovine cortical bone utilizing a multi-technique analysis. *Danubia Adria Symposium on Advances in Experimental Mechanics.*, 33.

[1] presenting author

TECHNISCHE UNIVERSITÄT WIEN
Vienna University of Technology

INSTITUTE FOR MECHANICS OF MATERIALS AND STRUCTURES

The allocation of bone fluid in bovine cortical bone utilizing a multi-technique analysis

Luis Zelaya-Lainez[1], Hawraa Kariem[1], Winfried Nischkauer[2], Andreas Limbeck[2], Christian Hellmich[1]

[1]Institute for Mechanics of Materials and Structures [2]Institute of Chemical Technologies and Analytics

Motivation

It is well accepted that the mechanical properties of bone depend crucially on the materials composition in terms of mineral and collagen content, as well as the hierarchical organization of those components [3]. What is less known, is the role of the third major structural component in bone, which is water. It is partitioned in three levels of pore spaces, ranging from the nanometer to the millimeter level. The porosity of cortical bone (**A**) includes the Vascular Porosity (**B**), the Lacunae Porosity(**C**), and the Ultra-structure Porosity. Besides the hierarchical organization, the quantitative aspects of this partitions remains largely unknown. The present work elucidates this issue, by refining the landmark protocol of Lees and coworkers [2], and performing simultaneous investigations with the light microscope LM.

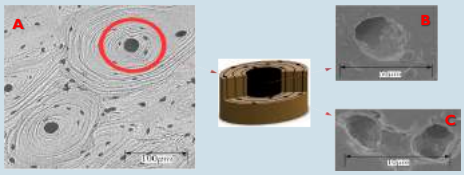

Material & Experimental Methods

Sample Preparation

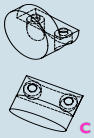

The 24 bone samples were harvested from a healthy bovine femur (**A**). The bone samples were first cut into smaller pieces using a diamond blade band saw. The smaller pieces were cleaned from the remaining soft tissue. The samples were later cut into the individual sample sizes with a low speed saw (**B**). The samples were subsequently attached to a custom-made steel holder (**C**), and polished in a two-step polishing process using a rotating polishing system (**D**).

Porosity Determination

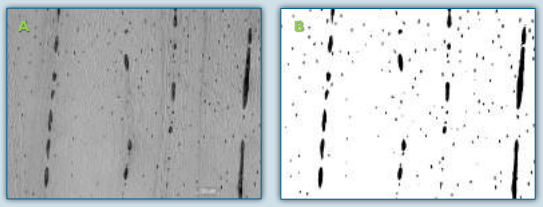

Each image obtained under the LM (**A**) was converted into an 8-bit image and filtered manually (**B**). The image segmentation was performed by a two-level threshold method. The pores were divided into Vascular pores and Lacunae pores by setting an user-defined second threshold condition.

Dehydrated State

The samples was dehydrated under vacuum alongside with an orange silica gel desiccant. The mass from each of the samples was monitored in a precision balance until no change was noticed. At this point, the samples are considered to be dehydrate, *i.e.* the bone samples are dry in equilibrium with a water-free environment and at room temperature.

Hydrated State

From the twenty-four dehydrated samples, eighteen samples were immersed into a Hank's Balanced Salt Solution (**HBSS**) with pH 7.4, and six samples were immersed in **Xylene**. The weight from each immersed sample was registered every two hours for a twenty-four hour period. After the twenty-four-hour period, the weight from each immersed sample was measured every day for a six-day period. At this point the samples are considered to be hydrated. Subsequently, the volumes were calculated using the Archimedes´ Principle.

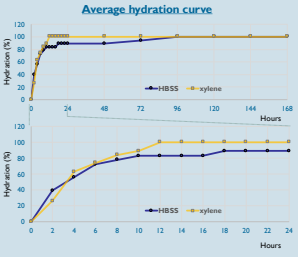

Demineralized State

The twenty-four samples were demineralized using a 0.5 M EDTA solution with a pH 7.5. The solutions of the three immersions from each sample were examined in an Optical Emission Spectrometer (ICP-OES) in order to detect the presence of Calcium, Magnesium, or Phosphorous. After not detecting any of the before-mentioned minerals in the last 0.5 M EDTA solutions, the samples are considered to be demineralized at this point.

Results & Discussion

Weight Fractions and Density

Density:

$$\rho = \frac{Mass_{total}}{Volume_{total}}$$

The mass of the bone contents are normally given in terms of the content weight fraction.

Weight Fraction:

$$WF_i^j = \frac{Mass_i^j}{Mass_{total}}$$

with:
$i = water$ for water content
$i = HA$ for mineral content
$i = org$ for organic content

Sample	ρ (g/cc)	WF_{org}	WF_{HA}
HBSS	1,99	0,2063	0,6808
Xylene	1,90	0,1949	0,6680

Sample	WF_{water}	$WF_{water}^{vascular}$	$WF_{water}^{lacunae}$	WF_{water}^{ultra}
HBSS	0,1129	0,0161	0,0098	0,0870
Xylene	0,1383	0,0145	0,0079	0,0942

Volume Fractions

Volume Fraction:

$$f_i^j = \frac{Volume_i^j}{Volume_{total}}$$

with:
$i = water$ for water content
$i = HA$ for mineral content
$i = org$ for organic content

Sample	f_{water}	f_{org}	f_{HA}
HBSS	0,2227	0,3263	0,4510
Xylene	0,2893	0,2883	0,4224

Sample	$f_{water}^{vascular}$	$f_{water}^{lacunae}$	f_{water}^{ultra}
HBSS	0,0320	0,0195	0,1711
Xylene	0,0312	0,0169	0,1906

Discussion

The results provide a significant addition and validation to previous experiments performed by [1] and [2]. Finally, with the results of the weight fractions and volume fractions we revealed the partition of bone fluid at the micro-structural and ultra-structural scale. Being bone a composite material, the allocation and quantification of fluid, along with the mineral and organic contents, are essential to a better understanding of the reaction of bones toward forces,

References:
[1] Robinson and Elliot (1957), *The Journal of Bone and Joint Surgery* 39(1):167–188.
[2] Lees et al., (1979) *Calcified Tissue International* 29(1):107–117.
[3] Fritsch and Hellmich (2007), *Journal of Theoretical Biology* 244(4):597–620.

Bibliography

[Alexander et al., 2012] Alexander, B., Daulton, T. L., Genin, G. M., Lipner, J., Pasteris, J. D., Wopenka, B., and Thomopoulos, S. (2012). The nanometre-scale physiology of bone: steric modelling and scanning transmission electron microscopy of collagen–mineral structure. *Journal of the Royal Society Interface*, 9:1774–1786.

[Anderson et al., 2005] Anderson, H. C., Garimella, R., and Tague, S. E. (2005). The role of matrix vesicles in the growth plate development and biomineralization. *Frontiers in Bioscience*, 10:822–837.

[Andriotis et al., 2015] Andriotis, O., Chang, S., Vanleene, M., Howarth, P., Davies, D., Shefelbine, S., M.J., B., and Thurner, P. J. (2015). Structure–mechanics relationships of collagen fibrils in the osteogenesis imperfecta mouse model. *Journal of The Royal Society Interface*, 12(111):188–200.

[Atkinson and Hallsworth, 1983] Atkinson, P. and Hallsworth, A. (1983). The changing pore structure of aging human mandibular bone. *Gerodontology*, 2:57–66.

[Bailey, 2001] Bailey, A. (2001). Molecular mechanisms of ageing in connective tissues. *Mechanisms of Ageing and Development*, 122:735–755.

[Benezra Rosen et al., 2002] Benezra Rosen, V., Hobbs, L., and Spector, M. (2002). The ultrastructure of anorganic bovine bone and selected synthetic hyroxyapatites used as bone graft substitute materials. *Biomaterials*, 23:921–928.

[Biltz and Pellegrino, 1969] Biltz, R. M. and Pellegrino, E. D. (1969). The chemical anatomy of bone. *The Journal of bone and joint surgery*, 51:456–466.

[Bonucci, 2000] Bonucci, E. (2000). *Mechanical testing of bone and the bone-implant interface* . CRC Press LLC, New York City, USA.

[Bozeca et al., 2005] Bozeca, L., de Grootb, J., Odlyhac, M., Nichollsa, B., Nesbitta, S., Flanagand, A., and Horton, M. (2005). Atomic force microscopy of collagen structure in bone and dentine revealed by osteoclastic resorption. *Ultramicroscopy*, 105:79–89.

[Bradbury and Bracegirdle, 1998] Bradbury, S. and Bracegirdle, B. (1998). *Introduction to Light Microscopy.* Springer-Verlag., New York City, USA.

[Bryan, 1951] Bryan, J. G. (1951). The generalized discriminant function: Mathematical foundations and computational routine. *Harvard Educational Review*, 21:90–95.

[Buckwalter et al., 1996] Buckwalter, J., Glimcher, M., Cooper, R., and Recker, R. (1996). Bone biology. i: Structure, blood supply, cells, matrix, and mineralization. *The journal of bone and joint surgery*, 77(8):1256–1275.

[Burns, 1929] Burns, C. M. (1929). The effect of the continued ingestion of mineral acid on growth of body and bone and on the composition of bone and of the soft tissues. *Biochemical Journal*, 23:860–867.

[Butler, 1984] Butler, W. (1984). Matrix macromolecules of bone and dentin. *Collagen and related research*, 297(6):297–307.

[Carriero et al., 2014] Carriero, A., Doube, M., Vogt, M., Busse, B., Zustind, J., Levchuk, A., Schneider, P., Müller, R., and Shefelbine, S. (2014). Altered lacunar and vascular porosity in osteogenesis imperfecta mouse bone as revealed by synchrotron tomography contributes to bone fragility. *Bone*, 61:116–124.

[Cowin, 1999] Cowin, S. C. (1999). Bone poroelasticity. *Journal of biomechanics*, 32(1999):217–238.

[Currey, 1964] Currey, J. (1964). The relationship between the stiffness and the mineral content of bone. *Biorheology*, 2:1–10.

[Currey, 1969] Currey, J. (1969). Three analogies to explain the mechanical properties of bone. *Journal of biomechanics*, 2:477–480.

[Dong et al., 2013] Dong, P., Haupert, S., Hesse, B., Langer, M., Gouttenoire, P.-J., Bousson, V., and Peyrin, F. (2013). 3d osteocyte lacunar morphometric properties and distributions in human femoral cortical bone using synchrotron radiation micro-ct images. *Bone*, 60:172–185.

[Eberhardsteiner et al., 2014] Eberhardsteiner, L., Hellmich, C., and Scheiner, S. (2014). Layered water in crystal interfaces as source for bone viscoelasticity: Arguments from a multiscale approach. *Computer Methods in Biomechanics and Biomedical Engineering*, 17:48 – 63.

[Fritsch and Hellmich, 2007] Fritsch, A. and Hellmich, C. (2007). Universal microstructural patterns in cortical and trabecular, extracellular and extravascular bone materials: micromechanics-based prediction of anisotropic elasticity. *Journal of Theoretical Biology*, 244(4):597–620.

[Fritsch et al., 2009] Fritsch, A., Hellmich, C., and Dormieux, L. (2009). Ductile sliding between mineral crystals followed by rupture of collagen crosslinks: Experimentally supported micromechanical explanation of bone strength. *Journal of Theoretical Biology*, 260:230–252.

[Frost, 1960] Frost, H. (1960). Measurement of osteocytes per unit volume and volume components of osteocytes and canaliculae in man. *Henry Ford Hospital medical bulletin*, 8:208–211.

[Gao et al., 2003] Gao, H., Ji, B., Jager, I., Arzt, E., and Fratzl, P. (2003). Materials become insensitive to flaws at nanoscale: lessons from nature. *Proceedings of the National Academy of Sciences of the United States of America*, 100:5597–5600.

[Georgiadis et al., 2016] Georgiadis, M., Müller, R., and Schneider, P. (2016). Techniques to assess bone ultrastructure organization: orientation and arrangement of mineralized collagen fibrils. *Journal of The Royal Society Interface*, 13:1–26.

[Gong et al., 1964] Gong, J., Arnold, J., and Cohn, S. (1964). The density of organic and volatile and non- volatile inorganic components of the bone. *The Anatomical Record*, 149:319–324.

[Hammett, 1925] Hammett, F. S. (1925). A biochemical study of bone growth. *The Journal of Biological Chemistry*, 64:409–428.

[Hannah et al., 2010] Hannah, K., Thomas, C., Clement, J., De Carlo, F., and Peele, A. (2010). Bimodal distribution of osteocyte lacunar size in the human femoral cortex as revealed by micro-ct. *Bone*, 47:866–871.

[Hassenkam et al., 2004] Hassenkam, T., Fantnera, G. E., Cutronia, J. A., Weaverb, J. C., Morseb, D. E., and Hansmaa, P. K. (2004). High-resolution afm imaging of intact and fractured trabecular bone. *Bone*, 35:4–10.

[Hassenkam et al., 2005] Hassenkam, T., Jørgensen, H. L., Pedersen, M. B., Kourakis, A. H., Simonsen, L., and Lauritzen, J. B. (2005). Atomic force microscope on human trabecular bone from an old woman with osteoporotic fractures. *Micron*, 36:681–687.

[Hellmich and Ulm, 2003] Hellmich, C. and Ulm, F. (2003). Average hydroxyapatite concentration is uniform in the extracollagenous ultrastructure of mineralized tissues: evidence at the 1–10-micrometer scale. *Biomechanics and Modeling in Mechanobiology*, 2:21–36.

[Hellmich and Ulm, 2002] Hellmich, C. and Ulm, F. J. (2002). Micromechanical model for ultrastructural stiffness of mineralized tissues. *Journal of Engineering Mechanics*, 8(128):898–908.

[Hellmich et al., 2004] Hellmich, C., Ulm, F.-J., and Dormieux, L. (2004). Can the diverse elastic properties of trabecular and cortical bone be attributed to only a few tissue-independent phase properties and their interactions? arguments from a multiscale approach. *Biomechanics and Modeling in Mechanobiology*, 2:219–238.

[Hesse et al., 2013] Hesse, B., Männicke, N., Pacureanu, A., Varga, P., Lagner, M., Peyrin, F., and Raum, K. (2013). Accessing osteocyte lacunar geometrical properties in human jaw bone on the submicron length scale using synchrotron radiation μct. *Journal of Microscopy*, 255:158–168.

[Hesse et al., 2014] Hesse, B., Varga, P., Lagner, M., Pacureanu, A., Schrof, S., Männicke, N., Suhonen, H., Maurer, P., Cloetens, P., Peyrin, F., and Raum, K. (2014). Canalicular network morphology is the major determinant of the spatial distribution of mass density in human bone tissue: Evidence by means of synchotron radiation phase-contrast nano-ct. *Journal of Bone and Mineral Research*, 30:346–356.

[Katsamenis et al., 2015] Katsamenis, O. L., Jenkins, T., and Thurner, P. J. (2015). Toughness and damage susceptibility in human cortical bone is proportional to mechanical inhomogeneity at the osteonal-level. *Bone*, 76:158–168.

[Katz et al., 1984] Katz, J. L., Yoon, H. S., Lipson, S., Maharidge, R., Meunier, A., and Christel, P. (1984). The effects of remodeling on the elastic properties of bone. *Calcified Tissue International*, 36:S31–S36.

[Lakes, 1993] Lakes, R. (1993). Materials with structural hierarchy. *Nature*, 361:511–515.

[Lees, 1979] Lees, S. (1979). A model for the distribution of hap crystallites in bone—an hypothesis. *Calcified Tissue International*, 27:53–56.

[Lees, 1986] Lees, S. (1986). Water content in type i collagen tissues calculated from the generalized packaging model. *International Journal of biological macromolecules*, 16:281–303.

[Lees, 1987] Lees, S. (1987). Considerations regarding the structure of the mammalian mineralized osteoid from viewpoint of the generalized packing model. *Connective Tissue Research*, 16:281–303.

[Lees, 2003] Lees, S. (2003). Mineralization of type i collagen. *Biophysical Journal*, 85:204–207.

[Lees et al., 1983] Lees, S., Ahern, J., and Leonard, M. (1983). Parameters influencing the sonic velocity in compact calcified tissues of various species. *Journal of the Acoustical Society of America*, 74:28–33.

[Lees et al., 1984a] Lees, S., Bonar, L., and Mook, H. (1984a). A study of dense mineralized tissue by neutron diffraction. *International Journal of Biological Macromolecules*, 6:321–326.

[Lees et al., 1979a] Lees, S., Cleary, P., Heeley, J., and Gariepy, E. (1979a). Distribution of sonic plesio-velocity in a compact bone sample. *Journal of Acoustic Society of America*, 66:641–646.

[Lees and Escoubes, 1987] Lees, S. and Escoubes, M. (1987). Vapor pressure isotherms, composition and density of hyperdense bones of horse, whale and porpoise. *Connective Tissue Research*, 16(4):305–322.

[Lees et al., 1995] Lees, S., Hanson, D., and Page, E. (1995). Some acoustical properties of the otic bones of a fin whale. *Journal of the Acoustical Society of America.*, 99:2421–2427.

[Lees et al., 1994a] Lees, S., Hanson, D., Page, E., and Mook, H. (1994a). Comparison of dosage-dependent effects of beta-aminopropionitrile, sodium fluoride, and hydrocortisone on selected physical properties of cortical bone. *Journal of Bone and Mineral Research.*, 9:1377–1389.

[Lees and Heeley, 1981] Lees, S. and Heeley, J. D. (1981). Density of a sample bovine cortical bone matrix and its solid constituent in various media. *Calcified Tissue International*, 33(1):499–504.

[Lees et al., 1979b] Lees, S., Heeley, J. D., and Cleary, P. F. (1979b). A study of some properties of a sample of bovine cortical bone using ultrasound. *Calcified Tissue International*, 29(1):107–117.

[Lees and Page, 1992] Lees, S. and Page, E. A. (1992). A study of some properties of mineralized turkey leg tendon. *Connective Tissue Research*, 28(4):263–287.

[Lees et al., 1984b] Lees, S., Pineri, M., and Escoubes, M. (1984b). A generalized packing model for type i collagen. international. *Journal of Biological Macromolecules*, 6:133–136.

[Lees and Prostak, 1986] Lees, S. and Prostak, K. (1986). The locus of mineral crystallites in bone. *Connective Tissue Research*, 18:41–54.

[Lees et al., 1994b] Lees, S., Prostak, K., Ingle, V., and Kjoller, K. (1994b). The loci of mineral in turkey leg tendon as seen by atomic force microscope and electron microscopy. *Calcified Tissue*, 55:180–189.

[Mader et al., 2013] Mader, K. S., Schneider, P., Müller, R., and Stampanoni, M. (2013). A quantitative framework for the 3d characterization of the osteocyte lacunar system. *Bone*, 57:142–154.

[Mahalanobis, 1936] Mahalanobis, P. (1936). On the generalized distance in statistics. *Proceedings of the National Institute of Science of India*, 12:49–55.

[Marotti, 1993] Marotti, G. (1993). A new theory of bone lamellation. *Calcified tissue international*, 53:S47–S56.

[Marotti et al., 1994] Marotti, G., Muglia, M., Palumbo, C., and Zaffe, D. (1994). The microscopic determinants of bone mechanical properties. *Italian journal of mineral and electrolyte metabolism*, 4:167–175.

[McNally et al., 2013] McNally, E. A., Nan, F., Botton, G. A., and Schwarcz, H. P. (2013). Scanning transmission electron microscopic tomography of cortical bone using z-contrast imaging. *Micron*, 49:46–53.

[McNally et al., 2012] McNally, E. A., Schwarcz, H. P., Botton, G. A., and Arsenault, A. L. (2012). Ta model for the ultrastructure of bone based on electron microscopy of ion-milled sections. *PLoS ONE*, 7:e29258.

[Morris et al., 1982] Morris, M., Lopez-Curato, J., Hughes, S., An, K., Bassingthwaighte, J., and Kelly, P. (1982). Fluid spaces in canine bone and marrow. *Microvascular Research*, 23:188–200.

[Newman and Newman, 1958] Newman, W. F. and Newman, M. W. (1958). *The Chemical Dynamics of Bone Mineral.*, volume XI of *209*. The University of Chicago Press, Chicago, USA.

[Orgel et al., 2006] Orgel, J. P., Irving, T., Miller, A., and Wess, T. J. (2006). Microfibrillar structure of type i collagen in situ. *Proceedings of the National Academy of Sciences of the United States of America*, 103(24):9001–9005.

[Orgel et al., 2001] Orgel, J. P., Miller, A., Irving, T. C., Fischetti, R. F., Hammersley, A. P., and Wess, T. J. (2001). The in situ supermolecular structure of type i collagen. *Structure*, 9:1061–106.

[Orgel et al., 2000] Orgel, J. P., Wess, T. J., and Miller, A. (2000). The in situ conformation and axial location of the intermolecular cross-linked non-helical telopeptides of type i collagen. *Structure*, 8:137–142.

[Palacio-Mancheno et al., 2014] Palacio-Mancheno, P. E., Larriera, A. I., Doty, S. B., Cardoso, L., and Fritton, S. P. (2014). 3d assessment of cortical bone porosity and tissue mineral density using high-resolution micro-ct: Effects of resolution and threshold method. *Journal of bone and mineral research*, 29:142–150.

[Parfitt, 1983] Parfitt, A. (1983). *The physiological and clinical significance of bone histomorphometric data*. CRC Press Inc., Boca Raton, USA.

[Pestruska and Hodge, 1964] Pestruska, J. A. and Hodge, A. J. (1964). A subunit model for the tropocollagen macromolecule. *Proceedings of the National Academy of Sciences of the United States of America*, 51:871–876.

[Pivonka et al., 2013] Pivonka, P., Buenzli, P. R., Scheiner, S., Hellmich, C., and Dustan, C. R. (2013). The influence of bone surface availability in bone remodelling — a mathematical model including coupled geometrical and biomechanical regulations of bone cells. *Engineering Structures*, 47:Pages 134–147.

[Prostak and Lees, 1996] Prostak, K. and Lees, S. (1996). Visualization of crystal-matrix structure. i situ demineralization of mineralized turkey leg tendon and bone. *Calcified tissue international*, 59:474–479.

[Raspanti et al., 1995] Raspanti, M., Guizzardi, S., Strocchi, R., and Ruggeri, A. (1995). Different fibrillar architectures coexisting in haversian bone. *Italian Journal of Anatomy and Embryology*, 100:103–112.

[Robinson and Elliot, 1957] Robinson, R. A. and Elliot, S. R. (1957). The water content of bone. *The journal of bone and joint surgery*, 39(1):167–188.

[Rubin and Jasiuk, 2005] Rubin, M. A. and Jasiuk, I. (2005). The tem characterization of the lamellar structure of osteoporotic human trabecular bone. *Micron*, 36:653–664.

[Rubin et al., 2003] Rubin, M. A., Jasiuk, I., Taylor, J., Rubin, J., Ganey, T., and Apkarian, R. P. (2003). Tem analysis of the nanostructure of normal and osteoporotic human trabecular bone. *Bone*, 33:270–282.

[Sasaki et al., 2002] Sasaki, N., Tagami, A., Goto, T., Taniguchi, M., Nakata, M., and Hikichi, K. (2002). Atomic force microscopic studies on the structure of bovine femoral cortical bone at the collagen fibril-mineral level. *Journal of Materials Science: Materials in Medicine*, 13:333–337.

[Schaffler and Burr, 1988] Schaffler, M. B. and Burr, D. B. (1988). Stiffness of compact bone: Effects of porosity and density. *Journal of Biomechanics*, 21:13–16.

[Scheiner et al., 2016] Scheiner, S., Komlev, V., Gurin, A., and Hellmich, C. (2016). Multiscale mathematical modeling in dental tissue engineering: Towards computer-aided design of a regenerative system based on hydroxyapatite granules, focusing on early and mid-term stiffness recovery. *Frontiers in Physiology*, 7:S. 1 – 18.

[Schwarcza et al., 2014] Schwarcza, H. P., McNally, E. A., and Botton, G. A. (2014). Dark-field transmission electron microscopy of cortical bone reveals details of extrafibrillar crystals. *Journal of Structural Biology*, 188:240–248.

[Sietsema, 1995] Sietsema, W. (1995). Animal models of cortical porosity. *Bone*, 4:297S–305S.

[Skinner et al., 1997] Skinner, R., Hickmon, S., Lumpkin, C., Aronson, J., and Nicholas, R. (1997). Decalcified bone: Twenty years of successful specimen management. *The Journal of Histotechnology*, 20:267–277.

[Suvarna et al., 1996] Suvarna, K. S., Layton, C., and Bancroft, J. D. (1996). *Bancroft's Theory and Practice of Histological Techniques*. Churchill Livingstone, New York City, USA, 7th edition.

[Urist et al., 1983] Urist, M. J., DeLange, R. J., and Finerman, G. (1983). Bone cell differentiation and growth factors. *Science*, 220:680–686.

[Wallace, 2012] Wallace, J. M. (2012). Applications of atomic force microscopy for the assessment of nanoscale morphological and mechanical properties of bone. *Bone*, 50:420–427.

[Weiner and Wagner, 1998] Weiner, S. and Wagner, H. (1998). The material bone: Structure-mechanical function relations. *Annual Review of Materials Science*, 28:271–298.

[Zhang et al., 1998] Zhang, D., Weinbaum, S., and Cowin, S. (1998). Estimates of the peak pressures in bone pore water. *Journal of Biomechanical Engineering*, 120:697–703.

APPENDIX D

Résumé of the author

Personal Information

Name:	**Luis Zelaya Lainez**
Date of birth:	July 31st, 1987
Nationality:	Honduras
Current address:	Brünner Straße 55/3/309, 1210 Vienna, Austria

Education

Master in Science (MSc.) **2010-2012**
Master's Degree in Occupational safety and health[a]
Polytechnic University of Valencia
Valencia, Spain.

Bachelor in Science (BSc.) **2005-2009**
Licentiate degree in Industrial Engineering[b]
Central American Technological University
Tegucigalpa, Honduras.

High School Diploma **1992-2005**
La Estancia School
Tegucigalpa, Honduras.

Awards

Young Researcher Award **2016**
33*rd* Danubia Adria Symposium on Advances in Experimental Mechanics
Portorož, Eslovenia

Committee Award **2003**
Proceedings of the Organization of American States
HACIA Democracy[c] Summit of the Americas
Guatemala City, Guatemala

[a] Thesis: "Dosimetric analysis and investigation of shielding of a radioisotope laboratory using the Monte Carlo based code MCNP5. Application to occupational risk assessment." Submitted at the department of chemical and nuclear engineering.
[b] 5 years engineering degree with a mechanical orientation.
[c] Organization based at Harvard University, Cambridge, USA.